

Coupled-cluster theory for open-shell nuclei

Gustav R. Jansen

Acknowledgements

To my beloved wife, without whom this work would never be finished. To my wonderful children, a continued source of joy and inspiration.

Contents

1	Introduction	1
2	Modelling the nucleus	5
2.1	Relevant degrees of freedom	5
2.2	The nuclear interaction	8
2.3	Many-body approximations	9
2.4	Proof of concept	14
2.5	Chasing convergence	16
2.5.1	Symmetries	16
2.5.2	Center-of-mass contamination	18
2.5.3	Convergence properties	19
3	Applications	23
3.1	Three-nucleon forces	23
3.1.1	Renormalized three-nucleon forces	24
3.1.2	Density-dependent three-nucleon forces	25
3.2	Nuclei as open quantum systems	26
3.3	Oxygen	26
3.3.1	The oxygen drip line	27
3.3.2	Magic numbers	27
3.3.3	Predictions	28
3.4	Calcium	28
3.4.1	Shell closure	29
3.4.2	Drip line	29
3.5	The complete picture	30
4	Concluding remarks	31

A	Attachments	39
A.1	Paper 1: Towards open-shell nuclei with coupled-cluster theory	39
A.2	Paper 2: Spherical coupled-cluster theory for open-shell nuclei	39
A.3	Paper 3: Continuum effects and three-nucleon forces in neutron-rich oxygen isotopes	39
A.4	Paper 4: Evolution of shell structure in neutron-rich calcium isotopes	39

Chapter 1

Introduction

We wish to understand the structure of matter. This is an enterprise that has occupied natural philosophers for millennia. In pre-Socratic Greece, Thales of Miletus envisioned water as the foundation of all matter, while contemporaries both in Greece and India formed the idea of an atom as the smallest undividable unit. And although the view of what constitutes the smallest units of matter has changed since, the idea that all matter can be reduced to its fundamental constituents is one of the pillars of modern particle physics.

While the attempt to describe matter using the fundamental degrees of freedom may sound appealing, in practical calculations such an approach is not possible. A successful description of matter can only be accomplished by using the tools and degrees of freedom that are relevant for the properties under investigation.

One of the primary goals in the study of matter, is to understand why matter is stable and the limits to its stability. These are important building blocks in our understanding of the origin and evolution of elements in the universe. Thus, we study the atomic nucleus – the smallest unit of matter that can exist, before the elements break down into their individual components and lose their identity. Of fundamental importance are the structural properties like for example masses, and thereby binding energies, as well as charge and density distributions in nuclei. These are quantities which reveal important information about the shell structure.

Along the valley of stability, represented by the black squares in Fig. 1.1,

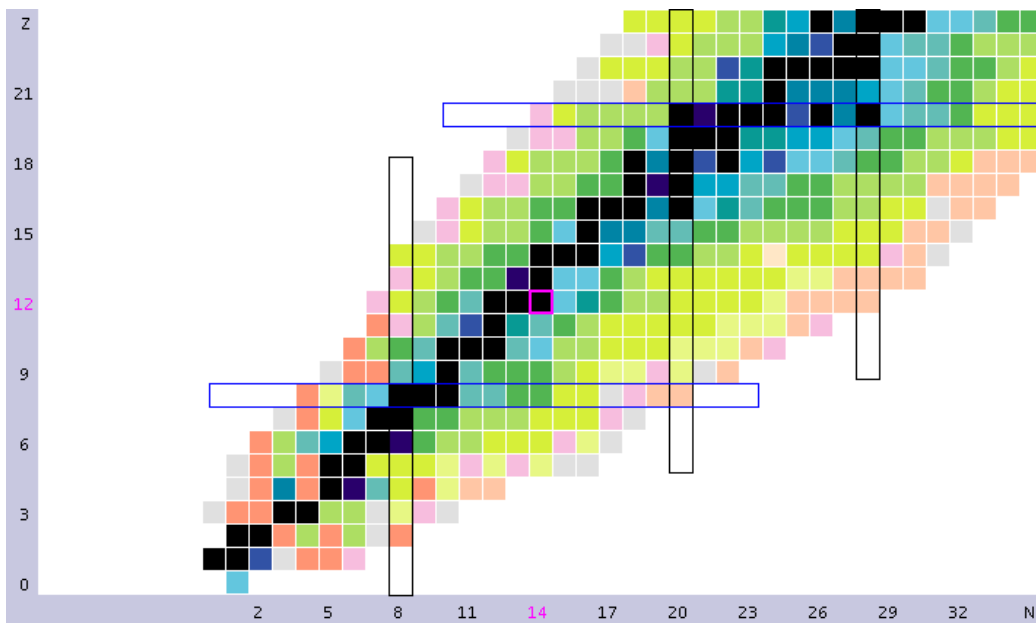


Figure 1.1: A subset of the nuclear chart, color coded by the half-life of the isotope. The darker colors represent long lifetimes. The vertical axis is the proton number, while the horizontal axis is the neutron number.

the shell structure is well known with magic numbers discovered over half a century ago. Only a simple model, based on the harmonic oscillator with a spin-orbit correction, is needed to explain this structure [1]. As we move away from the valley of stability and approach the drip lines, the structure changes in manners that cannot be explained by simple models. It is very difficult to conduct experiments in this region, as the isotopes have very small production cross-sections and their lifetimes are extremely short. However, a new generation of experimental facilities will offer unprecedented data on weakly bound systems near the limits of nuclear existence. To interpret such a wealth of experimental data and point to new experiments that can shed light on various properties of matter, requires a reliable and predictive theory. In view of the high investment costs and limited availability of the most exotic beams, it is also extremely important to use high-quality theoretical models to set correct priorities and differentiate between experiments that advance science most and those that can be safely postponed.

The approach taken to model the nucleus in this work, is the *ab initio* description of the nucleus based on nucleons as the relevant degrees of freedom. All properties of nuclei are sought to be explained solely by the interaction of non-relativistic particles. As this problem cannot be solved exactly for other than the lightest nuclei, the method we use introduces a set of controlled approximations to the original problem. Our task is to make sure that our calculated observables are good representations of the originals, before our method can be used predictively.

This thesis is divided into two parts. In section 2, the focus is on the development of a new method to solve the nuclear many-body problem. It is applicable to nuclei that can be described as two particles attached to or removed from a closed (sub-)shell nucleus. Two papers are presented where the method is evaluated. The first is a proof-of-principle, where the formal theory is detailed and a calculation is performed in a very small model space, where a comparison can be made to a numerically exact calculation. The second paper presents a set of analytical optimizations that exploit the rotational symmetry of the Hamiltonian. This allows calculations to be performed in very large model spaces, where converged results are obtained. Thus, the only error introduced is due to the approximations done in the method itself.

In section 3, the focus is on the applications of the method. As it is a part of a larger class of methods, where each solve the problem for a specific subset of nuclei, multiple methods were used to examine the properties of the isotopic chains of oxygen and calcium. These studies are presented in two separate papers.

Finally, section 4 contains some final remarks and a brief discussion of the road ahead. All four papers that are a part of this thesis, are included in the appendix.

Chapter 2

Modelling the nucleus

2.1 Relevant degrees of freedom

The reductionist approach to low-energy nuclear structure, would be to model the nucleus using whatever is currently considered the fundamental degrees of freedom. Today, that would be quarks and gluons, interacting through the strong, weak and electromagnetic force, as well as gravity. The focus of this thesis is on practical calculations and such an approach is not practically possible. There are several reasons for this. First, limits imposed on numerical precision would deny the simultaneous treatment of all forces. The effects of gravity and the weak interaction would be completely invisible compared to the effects of the remaining two forces. Second, the calculations that would have to be performed, are so complex that limitations in our current level of technology will not allow them. If this was not an issue, limits on the number of floating point operations that can be performed per second (FLOPS), would result in calculations that would basically never finish. Moreover, the precision required of experimental data to evaluate such a calculation, would have to be orders of magnitude better than what is possible today. Instead, we try to find the relevant degrees of freedom for any given property or process. If a solvable model can be worked out, it may provide not only valuable insight, but also clues to create a more accurate model for the next generation of tools.

The relevant degrees of freedom in low-energy nuclear physics are protons

and neutrons, collectively called nucleons. They are part of a larger family of particles called baryons, but only the nucleons are stable enough to survive and form the bound structures we call nuclei. In this model, the interaction between nucleons is mediated by a class of particles called mesons. The range of the interaction is determined by the mass of the meson involved, where the lightest mesons, called the pions, are considered dominant at long range or low energies. Both the baryons and the mesons are part of an even bigger family of particles called hadrons. All hadrons are composite particles, where the constituents are quarks and gluons. It is the interaction between the quarks and gluons, that is ultimately responsible for nuclear binding and the stability of matter.

In the standard model of particle physics, quantum chromodynamics (QCD) is the field theory that describes the strong interaction between quarks and gluons. The quarks come in six different flavours, but only the two lightest quarks, named up and down, make up the nucleons. In the larger picture, the up and down quarks are part of the first generation of particles together with the electron and the electron-neutrino, that are the constituents of all ordinary matter. The gluons are considered the force carriers mediating the strong nuclear force.

The quarks and gluons carry a strong charge, called color. This charge comes in three different values along with their anti-particle complements. Each quark carries only a single color. The color content of gluons is more complicated. Here, the color charge is a linear combination of different colors and anti-colors. There are only eight orthogonal combinations, making up the color octet of gluons.

There are two properties of QCD that are important when a model of the nucleus is attempted. One requires, while the other justifies the use of hadrons as the relevant degrees of freedom at low energies. The property of asymptotic freedom is a feature of QCD and it means that the coupling strength between quarks and gluons becomes weaker at higher energies. This enables a solution using perturbation theory, analogous to quantum electro dynamics (QED). At low energies, the interaction is very strong, with the consequence that low-energy QCD is non-perturbative. This means that a perturbative expansion in terms of the interaction, does not converge. The strong force is the only force that does not decrease in strength at long range and an exact solution of the field equations is necessary. Such a solution is certainly

possible. In lattice QCD (LQCD), euclidean space-time is modelled as a four-dimensional hypercube, where the field equations are solved using the path integral formalism. Using Monte Carlo integration, the integral kernel is only evaluated at certain points on the hypercube, called the grid points. A fixed distance between the grid points, called the lattice spacing, imposes a minimum spacing between particles. This is effectively a momentum cutoff, since the lattice spacing has to be small enough to resolve the structure of the wave function. In addition, the total number of points on the hypercube is limited by available hardware, which sets an upper limit to the size of the hypercube. An additional restriction is set by the mass of the particles to be included, as the hypercube must be able to contain them. The Compton wavelength of a point particle is inversely proportional to its mass, so the size of the hypercube sets a lower limit on the mass of the particles. Efforts have been made to calculate properties of the nuclear interaction directly using LQCD [2–4], but it is still necessary to use large quark masses, resulting in a pion mass of about 350 MeV. This is too large for a reliable extrapolation to experimental masses. Thus, the explicit treatment of quark degrees of freedom in a nucleus is not possible at present and requires a model where the nucleons are considered the relevant degrees of freedom.

Due to the strong interaction strength at long range, QCD displays a property called confinement. Free quarks are never observed, but are confined to form hadrons. It is important to realize that the hadrons carry no color charge. Quarks and anti-quarks combine in such a way, as to make color neutral composite particles. A quark and an anti-quark of the same color combine to form mesons, while three quarks with different colors combine to form baryons. Thus, the complex interaction observed between nucleons and mesons is only a residual interaction between quarks and gluons. This is completely analogous to the residual electromagnetic interaction observed between neutral atoms and molecules. Only at very high energies is the structure of hadrons visible to an observer, which justifies the use of hadrons as the relevant degrees of freedom in low-energy nuclear physics.

2.2 The nuclear interaction

The nuclear interaction is not known to us. There is no analogue to the Coulomb potential between electromagnetically charged particles, that acts between nucleons. This is because the nucleons are effective degrees of freedom, with complex interactions that must be fitted to experimental data to produce reliable results. We have many models with varying numbers of parameters, that reproduce nucleon-nucleon observables to a very high precision. Models based on meson exchange (see Machleidt [5] for an excellent introduction) are giving way to modern potentials based on the approximate chiral symmetries of QCD [6, 7]. While all models reproduce two-nucleon observables, for systems with more than two nucleons, the relevant observables are not reproduced. The nucleon-nucleon (NN) force is considered insufficient to reproduce the relevant observables.

Many take this as a clue that nucleons are not the only relevant degrees of freedom in the nucleus. Maybe pions and nucleon resonances have to be treated explicitly in any calculation involving more than two nucleons. The current approach is to model the missing physics by introducing three-nucleon forces (3NF). If this proves insufficient, maybe four-nucleon forces needs to be included as well. However, modern *ab initio* methods (see Leidemann and Orlandini [8] for a recent review) are barely capable of exploring the effects of three-nucleon forces in the lightest nuclei. It will take some time before a level of precision is reached where eventual four-nucleon forces are deemed necessary. The experimentally observed hierarchy of many-body forces ensures that we handle three-nucleon forces correctly, before contemplating forces with higher particle rank.

In the past fifteen years, a direct connection between the nuclear interaction and QCD has been established. Using the framework of effective field theory (EFT), chiral perturbation theory has unveiled a consistent picture of nuclear forces. Here, many-body forces emerge naturally and are all treated equally. The perturbative expansion is considered order by order and each order contributes less than the previous. This explains the experimentally observed hierarchy of many-body forces, as forces of higher particle rank appear later in the expansion. At the next-to-next-to-next-to-leading ($n^3\text{lo}$) order, which is the two-body interaction used in all our calculations, already three- and four-body forces are part of the theory. However, the four-body forces are

very small at this level.

The chiral interaction is suited to describe low energy processes. The hard scale, where the chiral expansion breaks down, is typically set around 1 GeV, while the interactions elements themselves are only set up to a cutoff below the hard scale. In the interaction used in this work [9], the cutoff is set at 500 MeV. Thus, the interaction is suitable for ground state energies, low energy excitation spectra and conventional nuclear reactions [6]. At higher energies, QCD becomes perturbative and conventional field theoretic approaches may be used.

2.3 Many-body approximations

In any *ab initio* many-body calculation, there are many different levels of truncations and approximations. Once the nuclear interaction is available, convergence has to be reached at every level, before we can say that we have the final result from a specific interaction. But already in the derivation of the interaction, many approximations have been made. The chiral interaction is expressed as a power series momentum scale. It is cut off at the level of $n^3\text{lo}$, where both three- and four-nucleon forces are part of the series. Diagrams have to be renormalized to account for divergent integrals and the integrals themselves have to be solved numerically, introducing a slight numerical error. Once these parameters are set, the free coupling constants in the theory are fitted to reproduce nucleon-nucleon scattering phase shifts. The experimental data used also has a varying degree of accuracy, that has to be accounted for in the fitting process. In addition, there are several numerical parameters used in the solution of the Lippmann-Schwinger equation that also have to be taken into account. Finally the matrix elements of the interaction can be produced. For each partial wave, a new set of matrix elements are produced in relative and center-of-mass coordinates. The number of partial waves is unfortunately infinite, so a numerical cutoff has to be introduced also at this level.

In this work, the many-body problem is solved in laboratory coordinates in a discrete harmonic oscillator basis. Single nucleon wave functions define the space of available many-body configurations. This space is called the Hilbert space and represents the space of available wave functions. The size

of this space is determined by the number of allowed harmonic oscillator shells. Various intermediate transformations are also performed, each with its own set of approximations, but these present no problems as they are taken to numerical precision.

Once the many-body basis has been defined, the Schrödinger equation can be solved exactly by means of a matrix diagonalization of the many-body Hamiltonian matrix. Unfortunately, this can only be done for light nuclei in relatively small model spaces (see Navrátil *et al.* [10] for a recent review). Additional approximations are necessary to reach heavier nuclei.

Let us make the previous discussion a bit more concrete, as it is needed to discuss the approximations made in coupled-cluster theory. Given a set of single-particle wave functions, we can construct a basis for an A -body Hilbert space \mathcal{H} , that consists of all possible Slater determinants that can be constructed from a given number of single-particle wave functions. The wave function can be expanded in a linear combination of these Slater determinants

$$|\Psi\rangle \approx |\Phi_0\rangle + \sum_{\substack{i_1 \\ a_1}} c_{i_1}^{a_1} |\Phi_{i_1}^{a_1}\rangle + \frac{1}{4} \sum_{\substack{i_1, i_2 \\ a_1, a_2}} c_{i_1 i_2}^{a_1 a_2} |\Phi_{i_1 i_2}^{a_1 a_2}\rangle + \dots \\ + \frac{1}{(A!)^2} \sum_{\substack{i_1, \dots, i_n \\ a_1, \dots, a_n}} c_{i_1 \dots i_n}^{a_1 \dots a_n} |\Phi_{i_1 \dots i_n}^{a_1 \dots a_n}\rangle, \quad (2.1)$$

where $|\Phi_0\rangle$ is the reference determinant, while the determinant $|\Phi_{i_1 \dots i_n}^{a_1 \dots a_n}\rangle$ has holes in orbitals labelled $i_1 \dots i_n$ and particles in orbitals labelled $a_1 \dots a_n$. As is customary in the coupled-cluster literature, orbitals with indices i, j, k, \dots represent hole states, i.e. single-particle states below the Fermi level, while orbitals with indices a, b, c, \dots represent particle states, i.e. single-particle states above the Fermi level. The amplitudes $c_{i_1 \dots i_n}^{a_1 \dots a_n}$ are the probability amplitudes for finding the A -body state in a given configuration. It is important to remember that if the single-particle basis is complete, this would be the exact wave function.

We can write this in operator form as

$$|\Psi\rangle \approx \hat{C}|\Phi_0\rangle = \left(\hat{1} + \sum_{n=1}^A \hat{C}_n \right) |\Phi_0\rangle, \quad (2.2)$$

where

$$\hat{C}_n = \frac{1}{(n!)^2} \sum_{\substack{i_1, \dots, i_n \\ a_1, \dots, a_n}} c_{i_1 \dots i_n}^{a_1 \dots a_n} \{a_{a_1}^\dagger \dots a_{a_n}^\dagger a_{i_n} \dots a_{i_1}\}. \quad (2.3)$$

Here $a_p^\dagger(a_p)$ are creation(annihilation) operators that create(annihilate) a particle in the orbital labelled p . The operator \hat{C}_n is called an n -particle- n -hole (nP - nH) excitation operator, and the curly brackets indicate that the operator product is normal ordered as used in Wicks theorem.

Solving the many-body Schrödinger equation in this basis for the unknown c -amplitudes, is called the full configuration interaction method (FCI) in the quantum chemistry literature and is equivalent to the exact diagonalization discussed above.

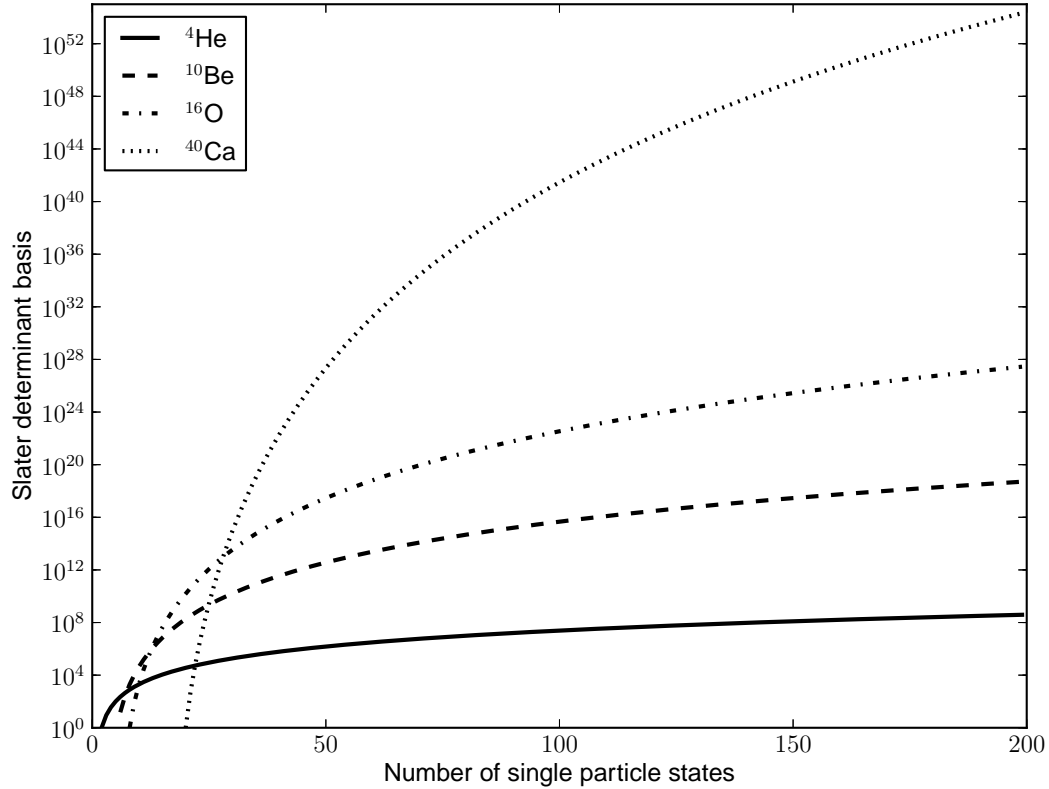


Figure 2.1: The number of possible Slater determinants as a function of the number of available single-particle states for ^4He , ^{10}Be , ^{16}O and ^{40}Ca . The vertical axis has a logarithmic scale.

The major problem of this approach, is the number of possible Slater determinant that can be constructed for a given single-particle space. In Fig. 2.1 we show the number of possible Slater determinants as a function of the number of single-particle wave functions for selected nuclei. For ^{16}O , there are already about 10^{28} possible Slater determinants that can be constructed using only 200 single-particle states. For comparison, a fully converged calculation of ^{16}O will require close to 4000 single-particle states in the uncoupled representation.

To perform these calculations, the space of Slater determinants has to be reduced. One approach is to introduce approximations by truncating the particle-hole expansion in Eq. (2.1). Such a truncation will in general lead to the inclusion of unwanted unlinked diagrams.

In coupled-cluster theory, we choose a different parametrization of the c -amplitudes, determined by the exponential expansion

$$|\Psi\rangle \approx |\Psi_{CC}\rangle = e^{\hat{T}}|\Phi_0\rangle, \quad \hat{T} = \hat{T}_1 + \hat{T}_2 + \dots + \hat{T}_A \quad (2.4)$$

where

$$\hat{T}_n = \left(\frac{1}{n!}\right)^2 \sum_{\substack{i_1, i_2, \dots, i_n \\ a_1, a_2, \dots, a_n}} t_{i_1 i_2 \dots i_n}^{a_1 a_2 \dots a_n} a_{a_1}^\dagger a_{a_2}^\dagger \dots a_{a_n}^\dagger a_{i_n} \dots a_{i_2} a_{i_1}$$

is the $n\text{P-}n\text{H}$ excitation operator discussed above. Writing out the Taylor expansion of this operator, reveals the equivalence between the two methods. There is a direct correspondence between the operators \hat{C} and $e^{\hat{T}}$ in the expansion of the wave function, which is translated into a relation between the individual amplitudes,

$$c_i^a = t_i^a \quad (2.5)$$

$$c_{ij}^{ab} = \frac{1}{2} t_i^a t_j^b + t_{ij}^{ab} \quad (2.6)$$

$$c_{ijk}^{abc} = \frac{1}{6} t_i^a t_j^b t_k^c + t_{ij}^{ab} t_k^c + t_{ijk}^{abc} \quad (2.7)$$

$$\vdots \quad (2.8)$$

Without truncations, the two methods are equivalent, but when truncations are introduced, important differences emerge. When \hat{C} is truncated at some

level n , no determinants with higher particle rank than \hat{C}_n can be produced. This is not the case when \hat{T} is truncated, as determinants of all ranks can be produced, due to the exponential expansion.. The number of degrees of freedom are still identical, but a different manifold is mapped out in the original Hilbert space. As a consequence, no unlinked diagrams appear in coupled-cluster theory.

Different truncations of \hat{T} define a hierarchy of coupled-cluster approximations. In nuclear physics, two truncations are used. When \hat{T} is truncated after 2P-2H amplitudes, the method is called the coupled-cluster singles and doubles (CCSD) approximation. Including triple excitations, by truncation \hat{T} at the 3P-3H level defines the coupled-cluster singles, doubles and triples (CCSDT) approximation. A peculiar situation arises, because in general CCSD is not accurate enough in nuclear physics applications, while CCSDT is too computationally expensive to be used routinely. Therefore, an additional level of approximation is introduced in Λ -CCSD(T) [11], where the effects of triple excitations are approximated based on singles and doubles amplitudes only. This is an approximation to the approximation, but it has proven very accurate and is currently considered state-of-the-art in coupled-cluster theory for nuclear physics.

Now, the defining equations for the cluster amplitudes can be found in any recent textbook on many-body methods. In Shavitt and Bartlett [12] all relevant equations up to CCSDTQ are listed in full. Once the amplitudes have been defined, the similarity transformed Hamiltonian is defined by

$$\bar{H} = e^{-\hat{T}} \hat{H}_N e^{\hat{T}}, \quad (2.9)$$

where \hat{H}_N is the Hamiltonian normal-ordered with respect to the A -body reference state. By diagonalizing this matrix in the proper Hilbert space, approximations to the energy eigenstates of the original Hamiltonian can be found. The Hilbert space is now defined by the standard particle-hole expansion represented by \hat{C} , and an additional level of approximation is introduced by truncating this space. This is called the equation-of-motion coupled-cluster theory (EOM-CC).

Whenever approximations are involved, we want to make sure that despite the approximations introduced, the results are still comparable to the exact solution. But in nuclear physics, this is only half the story. While we

must consider the quality of the coupled-cluster approximations by comparing our result to an exact diagonalization in an identical model space, we must simultaneously make sure that the interaction matrix elements we use are a good representation of the original interaction. Now, the quality of the coupled-cluster approximation is basically set. The Λ -CCSD(T) approximation is the best we can do for closed (sub-)shell nuclei. In the diagonalization procedure, we are currently not able to increase the size of the Hilbert space, due to the large number of single-particle wave functions. To refine these approximations, the computational cost needs to be reduced by optimizing the current implementation and an increase in the available computational resources are probably needed. The main challenge is then to make sure that our results are converged with respect to the size of the harmonic oscillator space.

We now introduce two papers, attached to this thesis as paper 1 in appendix A.1 and paper 2 in appendix A.2. These papers introduce an EOM-CC method that is tailored to the calculation of energy states in nuclei that can be described as two nucleons attached to or removed from a closed (sub-)shell nucleus. The first paper compares the results obtained to an exact diagonalization in a small single-particle space. The conclusions are discussed in section 2.4. The second paper explores the convergence properties of the method with respect to the size of the single-particle space. A discussion of this article can be found in section 2.5. These two articles represent the bulk of the work done in preparation for this thesis.

2.4 Proof of concept

In paper 1 [13], we defined two new methods within coupled-cluster theory, that expanded its reach to nuclei that can be described as two nucleons attached to or removed from a closed (sub-)shell nucleus. Both methods are based on the coupled-cluster singles and doubles (CCSD) approximation to a closed (sub-)shell reference, where a similarity transformation is constructed in a reduced Hilbert space. This results in a non-Hermitian operator labelled \bar{H} , which is often called the similarity transformed Hamiltonian in the literature. To obtain energy levels and eigenstates, \bar{H} is diagonalized in the space of the Slater determinants that are appropriate for the problem at hand.

When two nucleons are added, the method is called two particles attached EOM-CCSD (2PA-EOM-CCSD) and the many-body space is constructed of determinants that have two extra particles compared to the reference determinant. In paper 1, at most 3P-1H determinants were included in the diagonalization procedure. When two nucleons are removed from a reference nucleus, the method is called two particles removed EOM-CCSD (2PR-EOM-CCSD) and only determinants that have two particles less than the reference are included. At most 1P-3H determinants were included in the current implementation.

There are two reasons why these methods were introduced to nuclear physics. First, as already stated, coupled-cluster theory can be used to study a larger set of nuclei with these methods. Second, and related to the long term goals of the group, is the possibility of constructing effective operators for the use in shell-model calculations. The idea is to use the particle attached EOM-CCSD (PA-EOM-CCSD) and particle removed EOM-CCSD (PR-EOM-CCSD) approximations [14–16], which are suited for nuclei where one nucleon is added to or removed from a closed (sub-)shell nucleus, to obtain single-particle energies. The methods presented here are then used to obtain an effective interaction in a reduced space. Thus, coupled-cluster theory can be used to study an even larger set of nuclei, also in the heavy mass regime. For this procedure to work, it is crucial that these methods provide accurate approximations to both energy levels and the wave functions. Currently, only energy levels can be obtained as the calculations of other expectation values are more involved. To further evaluate the wave functions, radii, charge distributions, transition probabilities etc. should also be calculated. These properties are more sensitive to changes in the wave function than the energy.

To evaluate the accuracy of the methods, we studied the helium isotopes $^3\text{--}^6\text{He}$ and compared the approximate results to an exact diagonalization in a very small model space. The quality of the results was mixed. First the PR-EOM-CCSD approximation was unable to accurately describe the ground state of ^3He . This was to be expected as the removal of a nucleon from ^4He is not considered a good approximation to ^3He . This method performs better for heavier nuclei [17, 18].

The main result of the paper, was the quality of the PA-EOM-CCSD and 2PA-EOM-CCSD approximations. Both methods were able to provide ground state energies within half a percent of the exact energies for ^5He and ^6He re-

spectively. In ${}^6\text{He}$, the 2PA-EOM-CCSD approximation of the first excited $J^\pi = 2^+$ state was within the same level of accuracy.

These nuclei are especially good candidates for the EOM-CC framework. Both nuclei can be described and are viewed as an inert ${}^4\text{He}$ core, interacting with one or two nucleons. ${}^4\text{He}$ is deeply bound, about 20 MeV below the nucleon emission threshold and it has no bound excited states. The alpha cluster is therefore expected to retain its structure when additional neutrons are added.

The 2PR-EOM-CCSD approximation was not evaluated in this work, but similar results to those obtained by the PR-EOM-CCSD approximation are to be expected. This discouraged the further optimization of this method in the coupled representation, but when the next level of refinements are implemented, this method will be evaluated.

2.5 Chasing convergence

One of the main goals of the work leading up to this thesis, has been to do converged calculations of medium mass nuclei like ${}^{42,50,56,62}\text{Ca}$, approaching the neutron drip line for this element. In the coupled-cluster framework, these nuclei are only accessible by the 2PA-EOM-CCSD approximation. From earlier studies [19], it was known that the basis size would have to include at least 17-19 major oscillator shells for convergence in this region. In the previous section, we presented the 2PA-EOM-CCSD approximation in a basis of Slater determinants, which we will call the uncoupled representation. In the uncoupled representation the largest calculations we performed used a basis size of only five harmonic oscillator shells. This approach was not viable for the large model spaces needed for convergence.

2.5.1 Symmetries

The many-body Hamiltonian has several intrinsic symmetries. Each of these give rise to a conserved quantum number. While a complete description is beyond the scope of this thesis, a brief discussion of the relevant quantum

numbers and the symmetries associated with them, is in order (for details see e.g. Bohr and Mottelson [20]).

The nuclear Hamiltonian is invariant to the familiar space-time transformation. Invariance under translation leads to the conservation of total momentum, invariance under rotation leads to the conservation of the total angular momentum. In addition, the Hamiltonian is invariant with the respect to space inversion, which leads to the conservation of parity. In the Slater determinant basis used in the uncoupled representation, the total parity is a good quantum number. That means that each Slater determinant has a specific parity determined by the orbital momenta of all individual single-particle wave functions. The same is also true for the projection of the total angular momentum, which is the sum of all individual projections. The conservation of these quantum numbers was exploited already in the uncoupled representation as the quantum numbers were additive and easy to implement.

The Slater determinant basis does not, in general, have a good total angular momentum. Only the singlet states with zero total angular momentum can be associated with a Slater determinant. A new basis had to be constructed, where each basis state had a specific total angular momentum. This is what we refer to as the coupled representation or the jj -scheme. To accomplish this, a fair bit of angular momentum algebra had to be performed and the resulting algebraic expressions are cluttered with recoupling coefficients, complicated phases and sums over intermediate angular momentum variables. The implementation of these equations is a bug prone operation, and care has to be taken to verify the implementation. The payoff, however, is immense and is one of the major reasons that converged calculations in the medium mass sector were accomplished.

In paper 2, we presented the 2PA-EOM-CCSD method in the coupled representation. The theory presented there as well as the resulting implementation, is the main work of this thesis. For future reference, all algebraic expressions in the coupled representation were listed along with a thorough description of the procedure used to derive them.

2.5.2 Center-of-mass contamination

The nuclear Hamiltonian is invariant under Galilean transformations. This means that the Hamiltonian can be expressed as the sum of an intrinsic part and a center-of-mass part, where the intrinsic Hamiltonian only depends on relative coordinates. When many-body calculations are performed in relative and center-of-mass coordinates, this separation can be treated exactly. For more than a few particles however, this basis is not feasible. Because the explicit anti-symmetrization of the many-body wave functions is more complicated for many particles, the use of this basis for more than four particle is seldom done. In laboratory coordinates, the construction of anti-symmetric wave functions is trivial in the uncoupled representation. While it is more complicated in the coupled representation, the many-body basis consist of only four quasi particles and the coupling procedure is manageable for such systems. The problem, however, is that the final wave function is not guaranteed to factorize into a relative and a center-of-mass part – especially when a truncated space is used.

This problem was solved by Hagen *et al.* [21], where they demonstrated the approximate factorization of the ground state wave function in the Λ -CCSD(T) approximation. Later, it was also demonstrated for excited states when the procedure was applied to the PA-EOM-CCSD approximation. The factorization was not as good in this case, especially for higher lying excited states.

In paper 2, we demonstrate the factorization of the final wave function also for states calculated within the 2PA-EOM-CCSD approach. Some states, however, like the second $J^\pi = 0^+$ in ^{18}O , show a large center-of-mass contamination. The other two $J^\pi = 0^+$ states factorize approximately with reasonably high accuracy. The factorization was not explored in full, as calculations in larger model spaces have to be performed, but already at the current level there was a major difference between the states that factorize approximately and the ones that do not. We interpret the center-of-mass contamination as an indication that the many-body basis has been truncated prematurely. This can either be in the size of the harmonic oscillator single-particle space, the coupled-cluster truncation or the 3P-1H truncation implemented in this work.

2.5.3 Convergence properties

One of the main conclusions reached in paper 2, was that the current implementation was able to calculate converged energies using the “bare” chiral interaction. Both ground state energies and excitation energies were investigated for ${}^6\text{He}$, ${}^6\text{Li}$, ${}^{18}\text{O}$ and ${}^{18}\text{F}$, where selected states in both ${}^6\text{Li}$ and ${}^6\text{He}$ were compared to a no-core shell-model (NCSM) calculation [22]. While the ground state energies seemed to converge towards the NCSM result, the excitation energies were consistently overestimated. For some of the excited states, most of the difference can be attributed to the differences between the two calculations. The NCSM results were extrapolated to infinite model spaces and some uncertainties as to the exact parameters used in the interaction exist.

The $J^\pi = 3^+$ excited state in ${}^6\text{Li}$ however, was especially high in energy, about 700 keV compared to the NCSM result. While this is attributed to missing 4P-2H configurations in the EOM-CC diagonalization, we tried to identify possible properties that could be used to evaluate the accuracy of the calculation. This would be very useful in heavier nuclei, where exact diagonalization is not possible. We found the center-of-mass contamination of this state especially intriguing, but was unable to reach converged results for this expectation value. The contamination was only a few hundred keV and compared to the spurious center-of-mass states found in the spectrum, this was insignificant. Additional calculations using softer interactions were also performed to speed up convergence, but this contamination persisted. A quantitative analysis of this contamination is something we will have to look at in the future, especially its correlation to the error introduced in the coupled-cluster calculation. There are some obstacles that needs to be overcome before we can go any further. First, the comparison has to be done in a large model space, so that it can be considered numerically complete. This will require substantial computational resources, even if low-momentum interactions are used. Second, the calculation of expectation values in coupled-cluster is not exact. A discretized version of the Hellmann-Feynman theorem is used. A more exact approach would be to calculate the expectation value directly using the final wave functions.

Even though the center-of-mass contamination could not be analyzed quantitatively, it still proved a valuable tool. In ${}^{18}\text{O}$ it was a crucial element in

identifying the second $J^\pi = 0^+$ excited state. This state is known to have sizeable contributions from 4P-2H configurations [23] and should therefore not be reproduced in a 2PA-EOM-CCSD calculation, where the basis has been truncated at 3P-1H configurations. Our third $J^\pi = 0^+$ state, although the energy was completely converged, had a massive amount of center-of-mass contamination. Under the assumption that center-of-mass contamination suggests an unconverged calculation, we concluded that this state was not converged with respect to the EOM-CC truncation and was an ideal candidate for the experimentally observed second $J^\pi = 0^+$. This was further strengthened in paper 3, where the effects of three-nucleon forces were included. Here our second $J^\pi = 0^+$ was pushed up in excitation energy to the level of the experimentally observed third $J^\pi = 0^+$.

Three negative parity states also showed a large center-of-mass contamination and were excluded from the final spectrum. In these states, the level of 3P-1H configurations in the final wave function was larger than for the other states. This is natural, as 3P-1H excitations, where a nucleon is excited from the p -shell to the sd -shell, is one of the best ways to create negative parity states. A 2P configuration would have to include an orbital from the pf -shell to create a negative parity state. But larger 3P-1H amplitudes also indicates the need for additional 4P-2H configurations.

In general, both the ground and excited states in ^{18}O and ^{18}F , showed a reasonable level of convergence using 17 major oscillator shells. This required about 300 single-particle wave functions in the coupled representation and resulted in up to 300 million configurations ($J^\pi = 5^+$ in ^{18}F) at the 3P-1H level determining the dimensionality of the matrix to be diagonalized.

In papers 3 and 4, the 2PA-EOM-CCSD approximation was used to calculate the binding energy and excitation energies of neutron rich nuclei. While the rate of convergence with respect to the size of the model space was reduced, we were still able to perform converged calculations of both ^{26}O and ^{56}Ca . The latter required 21 harmonic oscillator shells before the ground state energy was converged and is the largest model space attempted with the current implementation. As more neutrons are added, the neutron drip line is getting closer and the isotopes are more weakly bound. A closer proximity to the nucleon emission threshold requires a larger model space when the harmonic oscillator basis is used. As only bound states are allowed by this basis, a large number of single-particle wave functions are needed to account

for the effect of the continuum. As we shall see in the next section, a different basis is more appropriate for such systems.

An additional point can be made about neutron rich systems in relation to the 2PA-EOM-CCSD approximation. In paper 4 we also calculated the excitation spectra of ^{50}Ti , ^{54}Ti and ^{56}Ti . These were obtained by adding two protons in the $f_{7/2}$ orbital. This orbital and those immediately above, were already fully occupied by neutrons in these systems. Compared to the respective calcium isobars, the results were not as good for these nuclei. This can be related to the proton-neutron interaction between protons in the $f_{7/2}$ orbital and neutrons in the orbitals $f_{7/2}$, $p_{3/2}$ etc. These are above the level of occupation in proton orbitals, but below that of neutron orbitals. The interaction between nucleons in these orbitals are now particle-hole interactions and not particle-particle interactions as they would be in $Z = N$ nuclei. The effect is that additional levels of particle-hole correlations are needed when protons are added to neutron rich reference states. It is probable that this is also the case when adding a proton neutron pair. The final wave functions of the titanium isotopes showed a significantly larger 3P-1H content, than their corresponding calcium isobars. It is evident that 4P-2H configurations are needed for nuclei with a high degree of asymmetry, but it is possible that also 5P-3H configurations need to be evaluated, which would prove quite difficult to accomplish in a coupled representation.

Chapter 3

Applications

Until now, the main focus of this thesis has been the development of the 2PA-EOM-CCSD approximation as well as its accuracy and convergence properties. We have shown that this method is suitable for calculating binding energies and the excitation energies of low-lying states with simple structure. However, it has been assumed that all states are bound, which are the only type of states allowed by the harmonic oscillator single-particle basis. In addition, it has been assumed that the nuclear Hamiltonian contains only two-body interactions. None of these assumptions survive comparison with experimental data.

3.1 Three-nucleon forces

It has been known for some time that the inclusion of three-nucleon forces (3NF) is necessary for a quantitative description of nuclei. In 2001, Pieper and Wiringa [24] showed explicitly that for light p -shell nuclei, nuclear properties can be accurately described starting from NN and 3NFs only.

For many-body methods based on a finite basis expansion, the inclusion of 3NFs is a formidable task. While the number of two-body matrix elements scale as $O(n^4)$, the number of three-body matrix elements scale as $O(n^6)$, where n is the number of single-particle basis states. As we saw in section 2.5, approximately 300 single-particle states were used for a converged cal-

calculation of the binding energy of ^{18}O , using the bare $n^3\text{lo}$ interaction. Thus, the number of three-body matrix elements for this calculation would be five orders of magnitude larger than the number of two-body matrix elements. The storage of matrix elements are already a limiting factor in many-body calculations, so a full treatment of 3NFs is not possible. In the uncoupled representation, the problem is much worse as this corresponds to roughly 4000 single-particle states resulting in over one Peta byte of two-body matrix elements alone.

We highlight two strategies to deal with this problem.

3.1.1 Renormalized three-nucleon forces

The major reason why a large model space is needed for a converged calculation, is because the interaction is hard. This means that it contains high-momentum components that will slow the rate of convergence. A softer interaction where the short range components have been removed, will reduce the number of matrix elements needed. This is the approach taken in recent no-core shell-model calculations, where the similarity renormalization group (SRG) [25] has been used to create effective low-momentum interactions.

There is a potential problem with this approach, that has yet to be resolved. The renormalization procedure itself induces many-body operators of higher rank than the original. This means that if the original operator was a two-body operator, the effective operator will contain three-body parts and higher. If the induced many-body operators are small, they can be safely neglected. If not, the final result will have a significant model dependence. This is illustrated in Roth *et al.* [26], where they conclude that when starting from a Hamiltonian that includes 3NFs, the SRG approach will induce sizeable four-nucleon forces.

These conclusions were drawn by extrapolating the result using effective interactions with different values of the SRG model parameter. The extrapolated values differed substantially. Now, this calculation can be criticized for using a fixed $\hbar\omega$ parameter throughout. If the $\hbar\omega$ dependence is different for the different values of the SRG model parameter, the extrapolations done in Roth *et al.* [26] will not describe the complete picture. This matter has yet to be resolved and a more detailed analysis will hopefully enlighten the

situation.

3.1.2 Density-dependent three-nucleon forces

The inclusion of 3NFs in coupled-cluster theory is faced with a different problem. A full inclusion using the CCSDT approximation, will require close to a thousand new diagrams to be added. This is a formidable task and will probably not be attempted any time soon.

In Hagen *et al.* [27], coupled-cluster theory for three-body Hamiltonians was presented at the CCSD level in the uncoupled scheme. A detailed analysis of the contribution from the 3NFs was performed for ${}^4\text{He}$. They showed that by including only the density-dependent zero-, one- and two-body parts of the normal ordered Hamiltonian used in coupled-cluster theory, most of the effects of the original 3NFs were accounted for. The residual three-body Hamiltonian accounted for less than a thousandth of the total binding energy. It must be said, that these calculations were done in very small model spaces with soft low-momentum interactions. The authors warn that this result might be due to the softness of the effective interaction used in the calculations. A more recent result, not yet published is presented in Roth *et al.* [28], where the same approach is used for heavier nuclei, show the same result. The residual interaction contributes very little to the total energies, but also here, soft effective interactions were used in the analysis.

But even using this approach, the full set of three-body matrix elements have to be stored and used to calculate the density dependent parts. A different approach was proposed by Holt *et al.* [29]. They proposed an effective three-body interaction based on chiral perturbation theory at next-to-next-to leading order. By integrating one nucleon line on all three-body diagrams at this level up to the Fermi momentum, this line was closed creating an effective two-body diagram. This procedure is designed for symmetric nuclear matter, but we wanted to investigate how this relatively simple effective interaction performed when used in finite nuclei. The result has been two papers [30, 31], attached to this thesis as paper 3 in appendix A.3 and paper 4 in appendix A.4, where this interaction is used on the oxygen and the calcium chain of isotopes.

3.2 Nuclei as open quantum systems

When moving away from the valley of stability, it becomes evident that the nuclei are not completely isolated systems. Weakly bound nuclei have ground states very close to their nucleon emission thresholds, while unbound nuclei might have resonant states that are detectable in modern experiments. A complete description of nuclei, would have to take this openness into consideration.

In the Gamow shell model [32], bound, resonant and continuum states are all accounted for on equal grounds by using the Berggren completeness relations [33]. The resulting basis can be used in standard many-body calculations by transforming the basis and matrix elements to a discrete basis in laboratory coordinates, as has been done in Hagen *et al.* [34, 35]. The entire coupled-cluster machinery can then be used, with a more correct treatment of continuum degrees of freedom, resulting in better results for nuclei and states close to the nucleon emission threshold. When resonances are to be included, a complex valued basis has to be used. The inclusion of resonances in particle attached or removed methods presents some issues, as the resonance is calculated with respect to the wrong threshold. This is a direct consequence of the treatment of the center-of-mass energy in the original Hamiltonian.

In both papers 3 and 4, the effects of continuum degrees of freedom were shown to be crucial for the description of neutron rich nuclei.

3.3 Oxygen

The oxygen isotopes are particularly interesting nuclei. Especially the neutron rich isotopes where new magic numbers have been established. It is also the heaviest element with an experimentally established drip line. Earlier studies have shown the need for both a correct inclusion of continuum degrees of freedom [36, 37] and that 3NFs were crucial to explain experimental data [38]. None has performed a complete calculation for the oxygen isotopes treating both continuum degrees of freedom and 3NFs simultaneously. This is what we set out to do in Hagen *et al.* [30] attached to this thesis as paper 3 in appendix A.3.

3.3.1 The oxygen drip line

Oxygen is the heaviest nuclei for which the neutron drip line is experimentally established. But the theoretical prediction of this drip line has not been easy. In Otsuka *et al.* [38] it was shown that the inclusion of the effects of 3NFs are necessary for establishing the correct drip line nucleus. Earlier studies, including coupled-cluster [37], where only NN interactions were used, were not able to do this. Using the density-dependent effective interaction described earlier to approximate the 3NFs from chiral perturbation theory, we were able to reproduce the drip line in the oxygen isotopes. This was considered clear evidence that this interaction includes important aspects of the 3NFs. Figure 1 in Hagen *et al.* [30] clearly shows that 3NFs are necessary for establishing drip line properties.

3.3.2 Magic numbers

The nuclear shell-model [1] is the current paradigm for our understanding of nuclear structure. In this model, the magic numbers are particularly important, because they denote especially stable numbers of protons and neutrons. The so-called doubly magic nuclei have a magic number of both protons and neutrons. The magic numbers were observed along the valley of stability and were explained theoretically by a mean field in addition to a strong spin-orbit interaction. But as the neutron to proton ratio changes, the magic numbers also change. In the oxygen isotopic chain, new doubly magic nuclei have been established at ^{22}O and ^{24}O [39–41], making the neutron numbers $N = 14$ and $N = 16$ magic.

The strongest experimental evidence for doubly magic structure, is a large separation energy, a reduced transition probability and a high excitation energy of the first excited state compared to that of neighbouring nuclei.

We find a high-lying first excited state both in ^{22}O and ^{24}O , but the inclusion of 3NFs is crucial for both results. In ^{24}O the first excited $J^\pi = 2^+$ is in the continuum, so continuum degrees of freedom are also important for this state. However, we did not investigate the specific effect of the continuum degrees of freedom for this result.

3.3.3 Predictions

The ultimate goal of nuclear many-body theory is to be fully predictive. In paper 3 attached to this thesis in appendix A.3, we make several predictions of observables not yet measured experimentally. The ground state of ^{28}O , a resonance, is predicted to be unbound with respect to ^{24}O by about 4 MeV with a resonant width of about 1 MeV. Without 3NFs this state would be bound compared to ^{24}O and would constitute the oxygen drip line [37]. Without continuum couplings, the energy would be much closer to that of ^{24}O .

We also predict three narrow resonances near the unknown experimental state at about 7.5 MeV in ^{24}O [42]. This supports Hoffman *et al.* [42], where they speculate that this resonance is a superposition of narrow resonances with $J^\pi = 1^+$ to 4^+ . However, we find the $J^\pi = 1^+$ state at significantly higher energy and shorter lifetime. Both 3NFs and continuum degrees of freedom were again crucial for finding these states at the reported values.

3.4 Calcium

In the oxygen isotopes, the inclusion of 3NFs was crucial for making ^{24}O doubly magic and a drip line nucleus. In the calcium isotopes the drip line is an unsettled topic. The heaviest isotope where mass measurement has been done is ^{52}Ca [43, 44], while the heaviest isotope observed is ^{58}Ca [45]. By a simple extrapolation to heavier calcium isotopes, it looks like ^{60}Ca will be close to threshold [46]. This is in contrast to energy-functional [47] calculations and mass-models [48, 49], that predict the drip line to be around ^{70}Ca . In addition, mean-field calculations [48, 49] predict that the single-particle states above ^{60}Ca are very closely spaced. As a result, the nuclei in this region might be very deformed, making a coupled-cluster approach difficult due to missing correlations. The evolution of shell structure in this region is particularly interesting and might hold similar surprises as the new magic neutron numbers found in the oxygen isotopic chain.

In paper 4, attached to this thesis in appendix A.4, we focused on the description of shell structure in neutron rich calcium isotopes in the $A = 50$ – 60 region, including both 3NFs and continuum degrees of freedom.

3.4.1 Shell closure

Experimentally, both ^{40}Ca and ^{48}Ca are well established doubly magic nuclei. But two-body forces alone does not yield a magic neutron number at $N = 28$. Again, the inclusion of 3NFs is necessary, as shown by Holt *et al.* [50]. At neutron number $N = 32$ a so-called sub-shell closure is well established in chromium, titanium and calcium [51–54]. At neutron number $N = 34$ however, no sub-shell closure is seen in either chromium or titanium [55–57], but the matter is still unsettled in calcium [58]. Theoretical studies [50, 59–61] predict everything from no shell gap to a large shell gap indicative of a major shell closure.

In the coupled-cluster calculations presented in paper 4, our results confirmed those of Holt *et al.* [50] – that the inclusion of 3NFs is needed for ^{48}Ca to be doubly magic and that the neutron number $N = 32$ generates a sub-shell closure in ^{52}Ca . One of our main results was the sub-shell closure of ^{54}Ca as well. The first excited $J^\pi = 2^+$ state in ^{54}Ca , was very similar in energy to the first excited state in ^{52}Ca . In addition, the $J^\pi = 4^+$ to 2^+ ratios were similar, leading us to conclude that coupled-cluster theory predicts a sub-shell closure in ^{54}Ca at this level of approximation.

3.4.2 Drip line

As can be seen from Fig. 1 in paper 4, coupled-cluster calculations using the density-dependent effective 3NF derived by Holt *et al.* [29], places the neutron drip line in the calcium isotopes to be between ^{56}Ca and ^{60}Ca . We place ^{60}Ca slightly unbound compared to ^{56}Ca , but missing many-body correlations might be more important for the description of ^{60}Ca , than for ^{56}Ca . This can result in additional binding in ^{60}Ca , so a definite conclusion cannot be drawn on this subject, due to the uncertainties in the extrapolated results. Including the effects of the continuum is very computationally demanding, as the number of single-particle state increase drastically. Thus, these calculation have not reached the same level of convergence as the calculations in lighter isotopes, resulting in increased extrapolation uncertainties.

But something interesting happens to the single-particle states in this region. The first orbitals above ^{60}Ca , where the neutron pf -shell is filled, changes order in our calculation compared to the naive shell-model picture. In this

picture the first three single-particle states above the pf -shell is the $g_{9/2}$, the $d_{5/2}$ and the $s_{1/2}$ orbitals. In our calculations, the $J^\pi = 5/2^+$ state drops below the $J^\pi = 9/2^+$ state in ^{53}Ca , ^{55}Ca and ^{61}Ca . Also in ^{61}Ca , the $J^\pi = 1/2^+$ state drops even lower than $J^\pi = 5/2^+$. In addition, the ground state of ^{62}Ca , is completely dominated by $(s_{1/2})^2$ configurations. This effect is all due to the correct treatment of the scattering continuum. Without these additional degrees of freedom, our calculations reproduce the shell-model ordering. This shows that the naive shell-model filling of $g_{9/2}$ on top of the pf -shell that has been established in zinc and nickel isotopes, is not correct in the calcium isotopes.

3.5 The complete picture

There are two major conclusion that I want to highlight from this chapter. First, a complete description of nuclei is not possible without the inclusion of three-nucleon forces and the correct treatment of the scattering continuum. Without these two elements, important structural information like shell closure, the location of the drip line and even the ordering of single-particle states will not be reproduced. A correct treatment of the scattering continuum will also facilitate a more unified approach to both structure and reactions.

Second, and absolutely paramount to coupled-cluster theory, is that the effects of three-nucleon forces can be approximated by density-dependent effective interactions at the two-body level. It must be noted that the interaction we have used is based on a very crude approach and that additional refinements of this interaction will hopefully make this approximation even more useful in practical calculations.

Chapter 4

Concluding remarks

The introduction of the 2PA-EOM-CCSD approximation to nuclear physics has been very successful. Even though a truncation has been introduced where at most 3P-1H configurations are allowed on top of a coupled-cluster reference state, we get good results. Of course, additional refinements must be introduced to allow even higher accuracy, but many of the results provided can be used quantitatively even now.

One of the major challenges in coupled-cluster theory, and in nuclear many-body physics in general, is the production of reliable *a priori* uncertainties. Due to the long history of coupled-cluster theory in computational quantum chemistry, certain rules of thumb have been established *a posteriori*. According to these, the CCSD approximation is able to account for approximately 90 percent of the correlation energy, the CCSDT approximation brings this up to 99 percent and each new level increase the accuracy by an order of magnitude. In nuclear physics, this rule of thumb has been seen to hold for doubly magic systems, where the coupled-cluster reference state is a good zeroth order approximation to the physical state. If it is not, like in for example ^{12}C , the coupled-cluster method is inadequate at the current level of approximation. In this work, we have demonstrated that coupled-cluster theory can uphold this level of uncertainty, even when used on open-shell nuclei like ^{18}O . However, the quality of the results depends strongly on the structure of the target state. If the error introduced by the approximations in the method can be quantified and a correlation can be established with the center-of-mass contamination of the final wave function, this might prove

to be a way towards reliable error estimates.

Another major challenge to coupled-cluster theory, is that the set of nuclei available to the method is very limited. Only closed (sub-)shell nuclei and their nearest neighbours are currently reachable. One possibility to expand this reach, is the construction of effective operators for shell-model calculations. Within the coupled-cluster framework, a completely microscopic shell-model input can be calculated. The PA-EOM-CCSD approximation can provide effective one-body operators and single-particle energies, while the 2PA-EOM-CCSD approximation can be used to construct the effective two-body operators. However, this requires the ability to reproduce all relevant states in an effective model space, to a high degree of accuracy. For heavier nuclei, significant improvements have to be made to allow the converged calculations of states with a large total angular momentum. While the *sd*-shell allows a maximum total angular momentum of five, including the *pf*-shell bring this up to seven. As an effect, the number of possible configurations at the 3P-1H level, quadruples within identical single-particle spaces. One solution might be to reduce the many-body space even further by introducing a different cutoff in the single-particle space for 3P-1H configurations than for 2P configurations. Physically this can be justified as the excitations around the Fermi level is thought to be the most important. This might also be a possible way to introduce 4P-2H configurations, which are important contributions to excitations in nuclei, because they can be viewed as excited alpha clusters. Excitations to highly excited states are less probable for such quasi-particles.

During the final stages of preparing this thesis, it was discovered that the effective three-nucleon interaction used in papers 3 and 4 was not correct. While paper 3 has been updated using a corrected version of the interaction, this has not yet been done in paper 4. This is due to the large amount of computer time needed to recalculate all results. However, an updated version will be available before this thesis is published.

Finally, it must be said that the current implementation has large rooms for improvement, especially now that new hybrid high performance clusters are becoming available. The efficient use of accelerators in high performance computing is an exciting area of study and promise orders of magnitude better performance than we can claim today.

Bibliography

- [1] M. G. Mayer and J. H. D. Jensen. *Elementary theory of nuclear shell structure*. Wiley, New York, 1955.
- [2] T. Inoue, N. Ishii, S. Aoki, T. Doi, T. Hatsuda, Y. Ikeda, K. Murano, H. Nemura, and K. S. Q. Collaboration. Prog. Theor. Phys. 124, 591, 2010.
- [3] K. Murano, N. Ishii, S. Aoki, and T. Hatsuda. Prog. Theor. Phys. 125, 1225, 2011.
- [4] S. A. Takumi Doi, T. Hatsuda, Y. Ikeda, T. Inoue, N. Ishii, K. Murano, H. Nemura, and K. S. Q. Collaboration. Prog. Theor. Phys. 127, 723, 2012.
- [5] R. Machleidt. Adv. Nucl. Phys. 19, 189, 1989.
- [6] R. Machleidt and D. Entem. Phys. Rep. 503, 1, 2011.
- [7] E. Epelbaum, H.-W. Hammer, and U.-G. Meißner. Rev. Mod. Phys. 81, 1773, 2009.
- [8] W. Leidemann and G. Orlandini. submitted to Progress in Particle and Nucl. Phys. arXiv:nucl-th/1204.4617v1, 2012.
- [9] D. R. Entem and R. Machleidt. Phys. Rev. C 68, 041001, 2003.
- [10] P. Navrátil, S. Quaglioni, I. Stetcu, and B. R. Barrett. J. Phys. G 36, 083101, 2009.
- [11] A. G. Taube and R. J. Bartlett. J. Chem. Phys. 128, 044110, 2008.
- [12] I. Shavitt and R. J. Bartlett. *Many-body methods in Chemistry and Physics*. Cambridge University Press, Cambridge, 2009.

-
- [13] G. R. Jansen, M. Hjorth-Jensen, G. Hagen, and T. Papenbrock. Phys. Rev. C 83, 054306, 2011.
 - [14] M. Włoch, J. R. Gour, P. Piecuch, D. J. Dean, M. Hjorth-Jensen, and T. Papenbrock. J. Phys. G 31, S1291, 2005.
 - [15] M. Musiał, S. A. Kucharski, and R. J. Bartlett. J. Chem. Phys. 118, 1128, 2003.
 - [16] M. Musiał and R. J. Bartlett. J. Chem. Phys. 119, 1901, 2003.
 - [17] O. Jensen, G. Hagen, M. Hjorth-Jensen, B. A. Brown, and A. Gade. Phys. Rev. Lett. 107, 032501, 2011.
 - [18] O. Jensen, G. Hagen, M. Hjorth-Jensen, and J. S. Vaagen. Phys. Rev. C 83, 021305, 2011.
 - [19] G. Hagen, T. Papenbrock, D. J. Dean, and M. Hjorth-Jensen. Phys. Rev. C 82, 034330, 2010.
 - [20] A. Bohr and B. R. Mottelson. *Nuclear structure*. Benjamin, New York, 1969.
 - [21] G. Hagen, T. Papenbrock, and D. J. Dean. Phys. Rev. Lett. 103, 062503, 2009.
 - [22] P. Navrátil and E. Caurier. Phys. Rev. C 69, 014311, 2004.
 - [23] P. Ellis and T. Engeland. Nucl. Phys. A 144, 161, 1970.
 - [24] S. C. Pieper and R. B. Wiringa. Annu. Rev. Nucl. Part. Sci. 51, 53, 2001.
 - [25] S. K. Bogner, R. J. Furnstahl, and R. J. Perry. Phys. Rev. C 75, 061001, 2007.
 - [26] R. Roth, J. Langhammer, A. Calci, S. Binder, and P. Navrátil. Phys. Rev. Lett. 107, 072501, 2011.
 - [27] G. Hagen, T. Papenbrock, D. J. Dean, A. Schwenk, A. Nogga, M. Włoch, and P. Piecuch. Phys. Rev. C 76, 034302, 2007.
 - [28] R. Roth, S. Binder, K. Vobig, A. Calci, J. Langhammer, and P. Navratil. Probably published soon. arXiv:nucl-th/1112.0287v1, 2011.
 - [29] J. W. Holt, N. Kaiser, and W. Weise. Phys. Rev. C 81, 024002, 2010.

- [30] G. Hagen, M. Hjorth-Jensen, G. R. Jansen, R. Machleidt, and T. Papenbrock. Accepted for publication in Phys. Rev. Lett. arXiv:nucl-th/1202.2839v1, 2012.
- [31] G. Hagen, M. Hjorth-Jensen, G. R. Jansen, R. Machleidt, and T. Papenbrock. Submitted to PRL. arXiv:nucl-th/1204.3612v1, 2012.
- [32] N. Michel, W. Nazarewicz, and M. Płoszajczak. Phys. Rev. C 70, 064313, 2004.
- [33] T. Berggren. Nucl. Phys. A 109, 265, 1968.
- [34] G. Hagen, M. Hjorth-Jensen, and N. Michel. Phys. Rev. C 73, 064307, 2006.
- [35] G. Hagen, D. J. Dean, M. Hjorth-Jensen, and T. Papenbrock. Phys. Lett. B 656, 169, 2007.
- [36] A. Volya and V. Zelevinsky. Phys. Rev. Lett. 94, 052501, 2005.
- [37] G. Hagen, T. Papenbrock, D. J. Dean, M. Hjorth-Jensen, and B. V. Asokan. Phys. Rev. C 80, 021306, 2009.
- [38] T. Otsuka, T. Suzuki, J. D. Holt, A. Schwenk, and Y. Akaishi. Phys. Rev. Lett. 105, 032501, 2010.
- [39] P. Thirolf *et al.* Phys. Lett. B 485, 16, 2000.
- [40] C. Hoffman *et al.* Phys. Lett. B 672, 17, 2009.
- [41] R. Kanungo *et al.* Phys. Rev. Lett. 102, 152501, 2009.
- [42] C. R. Hoffman *et al.* Phys. Rev. C 83, 031303, 2011.
- [43] A. Lapierre, M. Brodeur, T. Brunner, S. Ettenauer, P. Finlay, A. T. Gallant, V. V. Simon, P. Delheij, D. Lunney, R. Ringle, H. Savajols, and J. Dilling. Phys. Rev. C 85, 024317, 2012.
- [44] A. Gallant *et al.* submitted to PRL. arXiv:nucl-ex/1204.1987v1, 2012.
- [45] O. B. Tarasov, D. J. Morrissey, A. M. Amthor, T. Baumann, D. Bazin, A. Gade, T. N. Ginter, M. Hausmann, N. Inabe, T. Kubo, A. Nettleton, J. Pereira, M. Portillo, B. M. Sherrill, A. Stolz, and M. Thoennessen. Phys. Rev. Lett. 102, 142501, 2009.
- [46] M. Hjorth-Jensen. private communication, 2012.

- [47] W. Nazarewicz, J. Dobaczewski, T. R. Werner, J. A. Maruhn, P.-G. Reinhard, K. Rutz, C. R. Chinn, A. S. Umar, and M. R. Strayer. Phys. Rev. C 53, 740, 1996.
- [48] J. Meng, H. Toki, J. Y. Zeng, S. Q. Zhang, and S.-G. Zhou. Phys. Rev. C 65, 041302, 2002.
- [49] S. Fayans, S. Tolokonnikov, and D. Zawischa. Phys. Lett. B 491, 245, 2000.
- [50] J. D. Holt, T. Otsuka, A. Schwenk, and T. Suzuki. to be submitted. arXiv:nucl-th/1009.5984v2, 2011.
- [51] A. Huck, G. Klotz, A. Knipper, C. Miehé, C. Richard-Serre, G. Walter, A. Poves, H. L. Ravn, and G. Marguier. Phys. Rev. C 31, 2226, 1985.
- [52] A. Gade, R. V. F. Janssens, D. Bazin, R. Broda, B. A. Brown, C. M. Campbell, M. P. Carpenter, J. M. Cook, A. N. Deacon, D.-C. Dinca, B. Fornal, S. J. Freeman, T. Glasmacher, P. G. Hansen, B. P. Kay, P. F. Mantica, W. F. Mueller, J. R. Terry, J. A. Tostevin, and S. Zhu. Phys. Rev. C 74, 021302, 2006.
- [53] R. Janssens *et al.* Phys. Lett. B 546, 55, 2002.
- [54] J. Prisciandaro, P. Mantica, B. Brown, D. Anthony, M. Cooper, A. Garcia, D. Groh, A. Komives, W. Kumarasiri, P. Lofy, A. Oros-Peusquens, S. Tabor, and M. Wiedeking. Phys. Lett. B 510, 17, 2001.
- [55] N. Marginean *et al.* Phys. Lett. B 633, 696, 2006.
- [56] S. N. Liddick, P. F. Mantica, R. V. F. Janssens, R. Broda, B. A. Brown, M. P. Carpenter, B. Fornal, M. Honma, T. Mizusaki, A. C. Morton, W. F. Mueller, T. Otsuka, J. Pavan, A. Stolz, S. L. Tabor, B. E. Tomlin, and M. Wiedeking. Phys. Rev. Lett. 92, 072502, 2004.
- [57] D.-C. Dinca, R. V. F. Janssens, A. Gade, D. Bazin, R. Broda, B. A. Brown, C. M. Campbell, M. P. Carpenter, P. Chowdhury, J. M. Cook, A. N. Deacon, B. Fornal, S. J. Freeman, T. Glasmacher, M. Honma, F. G. Kondev, J.-L. Lecouey, S. N. Liddick, P. F. Mantica, W. F. Mueller, H. Olliver, T. Otsuka, J. R. Terry, B. A. Tomlin, and K. Yoneda. Phys. Rev. C 71, 041302, 2005.

-
- [58] M. Rejmund, S. Bhattacharyya, A. Navin, W. Mittig, L. Gaudenfroy, M. Gelin, G. Mukherjee, F. Rejmund, P. Roussel-Chomaz, and C. Theisen. *Phys. Rev. C* 76, 021304, 2007.
 - [59] M. Honma, T. Otsuka, B. A. Brown, and T. Mizusaki. *Phys. Rev. C* 65, 061301, 2002.
 - [60] E. Caurier, G. Martínez-Pinedo, F. Nowacki, A. Poves, and A. P. Zuker. *Rev. Mod. Phys.* 77, 427, 2005.
 - [61] L. Coraggio, A. Covello, A. Gargano, and N. Itaco. *Phys. Rev. C* 80, 044311, 2009.

Appendix A

Attachments

- A.1 Paper 1: Towards open-shell nuclei with coupled-cluster theory
- A.2 Paper 2: Spherical coupled-cluster theory for open-shell nuclei
- A.3 Paper 3: Continuum effects and three-nucleon forces in neutron-rich oxygen isotopes
- A.4 Paper 4: Evolution of shell structure in neutron-rich calcium isotopes

Toward open-shell nuclei with coupled-cluster theory

G. R. Jansen,¹ M. Hjorth-Jensen,¹ G. Hagen,^{2,3} and T. Papenbrock^{2,3,4,5}

¹*Department of Physics and Center of Mathematics for Applications, University of Oslo, N-0316 Oslo, Norway*

²*Physics Division, Oak Ridge National Laboratory, Oak Ridge, Tennessee 37831, USA*

³*Department of Physics and Astronomy, University of Tennessee, Knoxville, Tennessee 37996, USA*

⁴*GSI Helmholtzzentrum für Schwerionenforschung GmbH, D-64291 Darmstadt, Germany*

⁵*Institut für Kernphysik, Technische Universität Darmstadt, D-64289 Darmstadt, Germany*

(Received 8 February 2011; published 12 May 2011)

We develop a method based on equation-of-motion coupled-cluster theory to describe properties of open-shell nuclei with $A \pm 2$ nucleons outside a closed shell. We perform proof-of-principle calculations for the ground states of the helium isotopes $^3\text{--}^6\text{He}$ and the first excited 2^+ state in ^6He . The comparison with exact results from matrix diagonalization in small model spaces demonstrates the accuracy of the coupled-cluster methods. Three-particle–one-hole excitations of ^4He play an important role for the accurate description of ^6He . For the open-shell nucleus ^6He , the computational cost of the method is comparable with the coupled-cluster singles-and-doubles approximation while its accuracy is similar to the coupled-cluster with singles, doubles, and triples excitations.

DOI: [10.1103/PhysRevC.83.054306](https://doi.org/10.1103/PhysRevC.83.054306)

PACS number(s): 21.60.De, 21.10.Dr, 21.60.Gx, 31.15.bw

I. INTRODUCTION

The nuclear shell model is the paradigm for our understanding of atomic nuclei [1]. Within this model, doubly magic nuclei (with fully occupied shells for protons and neutrons) are particularly important because they are stronger bound than their neighbors and can be approximated by a simple product of single-particle states. Within the nuclear-shell model, doubly magic nuclei are the cornerstones for our understanding of entire regions of the nuclear chart as they can be viewed as inert cores. For the *ab initio* description of doubly magic nuclei, the coupled-cluster (CC) method, based on particle-hole excitations of a reference Slater determinant that obey the linked-cluster theorem, is particularly well suited and arguably one of the most efficient methods [2–4]. Similar remarks hold for nuclei that differ from doubly magic nuclei by one nucleon; such nuclei still exhibit a simple structure and a single Slater determinant is a good reference state. The structure of all other nuclei is more complicated and requires the superposition of many product states and correspondingly large model spaces.

For the light *p*-shell nuclei, various *ab initio* methods [5–11] yield virtually exact results for realistic Hamiltonians. For heavier systems, one typically relies on approximations. Here, coupled-cluster theory is an ideal compromise between accuracy on the one hand and computational cost on the other. This method has been applied to various problems in nuclear structure [2,3,12–17].

In this paper, we use equation-of-motion (EOM) techniques within the coupled-cluster method (EOM-CC hereafter) for the description of nuclei that differ from closed-shell references by two nucleons. This extension of the coupled-cluster method is useful for two reasons. First, it significantly enlarges the set of nuclei that can be accessed within coupled-cluster theory. For the oxygen isotopes $^{14\text{--}28}\text{O}$, for instance, all nuclei except ^{19}O differ from closed-subshell references by two neutrons or less. Similar comments apply to isotopes of helium and calcium. Questions related to the evolution of shell structure

[18,19] could thus be addressed from first principles. Second, the coupled-cluster method yields a similarity-transformed Hamiltonian [see Eq. (7) below] for a doubly magic nucleus. The Hamiltonians for one and two nucleons attached to this doubly magic core provide us with effective single-particle energies and an effective two-body interaction, respectively. These matrix elements could enter the construction of effective shell-model interactions [20] that are the basis for large-scale shell-model calculations [21,22].

Within the EOM-CC methods, the equations for excited states and one-particle-attached (removed) are well known in quantum chemistry [4,23–27] and have also been applied to atomic nuclei [28–31]. However, the corresponding equations for two-particle-attached (removed) have seen very few applications in quantum chemistry [32,33] and are of current interest in nuclear physics. In this article, we will extend the range of the EOM-CC methods to include open-shell nuclei with $A = \pm 2$ nucleons outside a closed-shell core. We present here the necessary formalism for deriving such equations, including the pertinent diagrams and algebraic equations. The results from our EOM-CC calculations are compared with full configuration-interaction (FCI) calculations for helium isotopes, demonstrating the accuracy of this approach.

This paper is organized as follows. In Sec. II, we give a brief overview of the equation-of-motion method within coupled-cluster theory. The extension of this method to two valence nucleons outside a closed-shell core is presented in Sec. II B. We discuss and present our results in Sec. III. Section IV contains our conclusions and an outlook for future work.

II. COUPLED-CLUSTER THEORY AND EQUATIONS-OF-MOTION FOR NUCLEI

A. Single-reference coupled-cluster theory

In this section we introduce the Hamiltonian that enters our calculation, together with a brief review of single-reference

coupled-cluster theory. We limit the presentation to those details that are required for the derivation of the two-particle-attached (removed) [2PA(R)] amplitudes presented in Sec. II B. The interested reader is referred to [4] for details.

We use the intrinsic Hamiltonian

$$\hat{H} = \left(1 - \frac{1}{A^*}\right) \sum_{i=1}^A \frac{p_i^2}{2m} + \left(\sum_{i < j=1}^A \hat{v}_{ij} - \frac{\vec{p}_i \cdot \vec{p}_j}{mA^*} \right). \quad (1)$$

Here, A is the number of nucleons in the reference state, A^* is the mass number of the nucleus that we wish to describe, and \hat{v}_{ij} is the nucleon-nucleon interaction. We will limit ourselves to two-body interactions only. In second quantization, the Hamiltonian can be written as

$$\hat{H} = \sum_{pq} \varepsilon_q^p a_p^\dagger a_q + \frac{1}{4} \sum_{pqrs} \langle pq || rs \rangle a_p^\dagger a_q^\dagger a_s a_r. \quad (2)$$

The term $\langle pq || rs \rangle$ is a shorthand for the matrix elements (integrals) of the two-body part of the Hamiltonian of Eq. (1), p, q, r , and s represent various single-particle states, while ε_q^p stands for the matrix elements of the one-body operator in Eq. (1). Finally, operators such as a_q^\dagger and a_p create and annihilate a nucleon in the state q and p , respectively. These operators fulfill the canonical anticommutation relations.

In single-reference coupled-cluster theory, the many-body ground state $|\Psi_0\rangle$ is given by the exponential ansatz,

$$|\Psi_0\rangle = \exp(\hat{T})|\Phi_0\rangle. \quad (3)$$

Here, $|\Phi_0\rangle$ is a single-reference Slater determinant and \hat{T} is the cluster operator that generates correlations. The operator \hat{T} is expanded as a linear combination of particle-hole excitation operators

$$\hat{T} = \hat{T}_1 + \hat{T}_2 + \dots + \hat{T}_A, \quad (4)$$

where \hat{T}_n is the n -particle– n -hole (n P- n H) excitation operator

$$\hat{T}_n = \left(\frac{1}{n!}\right)^2 \sum_{a_1 \dots a_n} t_{i_1 \dots i_n}^{a_1 \dots a_n} a_{a_1}^\dagger \dots a_{a_n}^\dagger a_{i_n} \dots a_{i_1}.$$

Throughout this work we use the convention that the indices i, j, k, \dots denote states below the Fermi level (holes), while the indices a, b, c, \dots denote states above the Fermi level (particles). For an unspecified state, the indices p, q, r, \dots are used. The amplitudes $t_{i_1 \dots i_n}^{a_1 \dots a_n}$ will be determined by solving the coupled-cluster equations. In the singles and doubles approximation, we truncate the cluster operator as

$$\hat{T} \approx \hat{T}_{\text{CCSD}} \equiv \hat{T}_1 + \hat{T}_2, \quad (5)$$

which defines the coupled-cluster approach with singles and doubles excitations, the so-called CCSD approximation. The unknown amplitudes result from the solution of the CCSD equations given by

$$\begin{aligned} \langle \Phi_i^a | \bar{H} | \Phi_0 \rangle &= 0, \\ \langle \Phi_{ij}^{ab} | \bar{H} | \Phi_0 \rangle &= 0. \end{aligned} \quad (6)$$

The term

$$\bar{H} = \exp(-\hat{T}) \hat{H} \exp(\hat{T}) = (\hat{H} \exp(\hat{T}))_C, \quad (7)$$

is the similarity transform of the normal-ordered Hamiltonian. The state $|\Phi_{ij \dots}^{ab \dots}\rangle$ is a Slater determinant that differs from the reference $|\Phi_0\rangle$ by holes in the orbitals i, j, \dots and by particles in the orbitals a, b, \dots . The subscript C indicates that only connected diagrams enter.

Once the t_i^a and t_{ij}^{ab} amplitudes have been determined from Eq. (6), the correlated ground-state energy is given by

$$E_{\text{CC}} = \langle \Phi_0 | \bar{H} | \Phi_0 \rangle + E_0. \quad (8)$$

Here, E_0 denotes the vacuum expectation value with respect to the reference state. The coupled-cluster equations (6) show that the reference state $|\Phi_0\rangle$ is an eigenstate of the similarity-transformed Hamiltonian (7) within the space of the 1P-1H and 2P-2H excitations.

B. Equation-of-motion coupled-cluster theory for nuclei with $A \pm 2$ nucleons outside a closed shell

In this work, our focus is on the development of coupled-cluster theory for nuclei that differ from a closed shell by two nucleons. These are systems where no single reference can be constructed without breaking symmetries (such as rotational invariance). One could apply the CCSD method to the deformed (symmetry breaking) Hartree-Fock ground state of an open-shell nucleus. However, the restoration of angular momentum requires more than singles and doubles cluster excitations (see, for example, Ref. [15]) and is computationally expensive. Here, we wish to stay within the computationally inexpensive CCSD scheme.

Open-shell systems can be computed with multireference methods. In such an approach, many reference wave functions are included and treated on an equal footing. However, the loss of mathematical simplicity, transparency, and problems related to intruder states make these multireference approaches difficult to pursue. For a detailed discussion, we refer the reader to Ref. [34]. Equation-of-motion methods [26,27] avoid these problems as they exhibit the transparency and computational simplicity of single-reference coupled-cluster theory.

Within the EOM-CCSD approach, the states of the $A \pm 2$ open-shell nuclei are computed from the ground state of the A -body system as

$$|\Psi_\mu^{(A\pm 2)}\rangle = \hat{R}_\mu^{(A\pm 2)} |\Psi_0^{(A)}\rangle = \hat{R}_\mu^{(A\pm 2)} \exp(\hat{T}) |\Phi_0\rangle. \quad (9)$$

Here, $\hat{R}_\mu^{(A\pm 2)}$ is a particle-removal or particle-addition operator that generates an $A \pm 2$ -body state from the A -body coupled-cluster wave function. The label μ identifies the quantum numbers (energy, angular momentum, ...) of the state of interest.

The operator \hat{R}_μ and the energies E_μ of the states of interest solve the eigenvalue problem [4,23–27]

$$(\bar{H} \hat{R}_\mu^{(A\pm 2)})_C |\Phi_0\rangle = \omega_\mu \hat{R}_\mu^{(A\pm 2)} |\Phi_0\rangle. \quad (10)$$

Here, the expression $(\bar{H} \hat{R}_\mu^{(A\pm 2)})_C$ denotes all terms that connect the similarity-transformed Hamiltonian \bar{H} with the excitation operator $\hat{R}_\mu^{(A\pm 2)}$. The energy difference $\omega_\mu \equiv E_\mu - E_0^*$ is the excitation energy of the state μ in the nucleus $A \pm 2$ with respect to the ground-state energy E_0^* of the closed-shell reference nucleus with the mass shift $A^* = A \pm 2$. This mass shift in the intrinsic Hamiltonian (1) ensures that the correct

kinetic energy of the center-of-mass is utilized in computing the $A \pm 2$ nuclei.

The operators \hat{R}_μ relevant for this work are (we drop the label μ for convenience)

$$\hat{R}^{(A+2)} = \frac{1}{2} \sum_{ba} r^{ab} a_a^\dagger a_b^\dagger + \frac{1}{6} \sum_{iabc} r_i^{abc} a_a^\dagger a_b^\dagger a_c^\dagger a_i + \dots, \quad (11)$$

$$\hat{R}^{(A-2)} = \frac{1}{2} \sum_{ij} r_{ij} a_i a_j + \frac{1}{6} \sum_{ijk a} r_{ijk}^a a_a^\dagger a_k a_j a_i + \dots, \quad (12)$$

where the unknown amplitudes r (subscripts and superscripts dropped) can be grouped into a vector that solves the eigenvalue problem of Eq. (10). The operator (11) consists of a 2P-0H term, a 3P-1H term, and in general up to an $(A+2)$ P-AH term. In this work, we will truncate the operator (11) at the 3P-1H level. Clearly, this truncation will only be a good approximation for states in the $A \pm 2$ -body system that have a relatively simple structure built on the A -body nucleus. We will introduce two different truncations for the particle-attached and the particle-removed method, and identify them by the number of particle-hole excitations kept in the operator (11). A truncation after the first term in Eq. (11) is referred to as 2PA-EOM-CCSD (2P-0H), while the truncation after the second term is denoted as 2PA-EOM-CCSD (3P-1H). Similarly for 2PR-EOM-CCSD, we will use the abbreviations 2PR-EOM-CCSD (0P-2H) and 2PR-EOM-CCSD (1P-3H) for truncations after the first and second term in Eq. (12), respectively. Table I shows the excitation operators used in these truncation schemes.

We construct the matrix (i.e., the connected part of $\bar{H} \hat{R}$) of the eigenvalue problem of Eq. (10) diagrammatically. As usual, lines directed upward represent particle states, while lines directed downward represent hole states [4]. The horizontal lines represent the operators and we use a heavy and a wiggly line to differentiate the two operators in the composite diagrams. Table II shows the diagrams corresponding to the r amplitudes, while the matrix elements of the similarity-transformed Hamiltonian are represented by the diagrams shown in Table III. These elements are well known and computed from the corresponding contractions of the cluster operator (5) with the Hamiltonian of Eq. (1) (see, for instance, Ref. [4]). They result from the construction of the operator (7) after the CCSD equations (6) have been solved.

TABLE I. Definition of the EOM excitation operators for the two-particle-attached (removed) method, using a truncation at both the 2P-0H (0P-2H) and 3P-1H (1P-3H) level. The operator \hat{R}_{2P-0H}^{A+2} defines 2PA-EOM-CCSD (2P-0H), the operator \hat{R}_{3P-1H}^{A+2} defines 2PA-EOM-CCSD (3P-1H), the operator \hat{R}_{0P-2H}^{A-2} defines 2PR-EOM-CCSD (0P-2H) while the operator \hat{R}_{1P-3H}^{A-2} defines 2PR-EOM-CCSD (1P-3H). These operators enter the eigenvalue problem of Eq. (10).

Operator	Expression
\hat{R}_{2P-0H}^{A+2}	$\frac{1}{2} \sum_{ab} r^{ab} a_a^\dagger a_b^\dagger$
\hat{R}_{3P-1H}^{A+2}	$\frac{1}{2} \sum_{ab} r^{ab} a_a^\dagger a_b^\dagger + \frac{1}{6} \sum_{abci} r_i^{abc} a_a^\dagger a_b^\dagger a_c^\dagger a_i$
\hat{R}_{0P-2H}^{A-2}	$\frac{1}{2} \sum_{ij} r_{ij} a_i a_j$
\hat{R}_{1P-3H}^{A-2}	$\frac{1}{2} \sum_{ij} r_{ij} a_i a_j + \frac{1}{6} \sum_{aijk} r_{ijk}^a a_a^\dagger a_k a_j a_i$

TABLE II. Diagrams corresponding to the excitation operators defined in Table I. Upward-directed lines denote unoccupied orbitals (particle states) and downward-directed lines denote occupied orbitals (hole states). The heavy horizontal line represents the operator vertex, used to distinguish the \hat{R} operators from the similarity-transformed Hamiltonian \bar{H} .

Amplitude	Diagram
r^{ab}	
r_{ij}	
r_i^{abc}	
r_{ijk}^a	

Table IV shows the algebraic expressions for the matrix elements of the similarity-transformed Hamiltonian \bar{H} . For notational efficiency, some intermediate objects (χ) that are common among several of the matrix elements, are defined separately in Table V. In the numerical implementation, the storage of the similarity-transformed Hamiltonian requires some memory. However, this modest cost in memory yields a significant reduction in computational cycles. For a detailed analysis, we refer the reader to Refs. [35,36].

In a diagrammatic language, the left-hand side of the eigenvalue problem (10) consists of all topologically different diagrams that result from connecting a diagram from Table II with a diagram in Table III. Figures 1 and 2 show the diagrams of $(\bar{H} \hat{R})_C$ for the two truncations of the 2PA-EOM-CCSD method. Let us briefly discuss some of these diagrams.

For the 2PA-EOM-CCSD (2P-0H) method, the relevant diagrams correspond to the matrix element $\langle \Phi^{ab} | (\bar{H} \hat{R})_C | \Phi_0 \rangle$ (i.e., they have two outgoing particle lines and consist of contractions of the similarity-transformed Hamiltonians with r^{ab}). As an example, consider the diagram of Fig. 1(b). It results from combining the diagram of r^{ab} (Table II) with the diagram of $\langle ab | \bar{H} | cd \rangle$ (Table III). For the 2PA-EOM-CCSD (3P-1H) method, additional diagrams of the form $\langle \Phi^{abc} | (\bar{H} \hat{R})_C | \Phi_0 \rangle$ enter because the amplitude r_i^{abc} is also permitted. In addition, diagrams corresponding to the matrix element $\langle \Phi_i^{abc} | (\bar{H} \hat{R})_C | \Phi_0 \rangle$ (i.e., diagrams with three outgoing particle lines and one incoming hole line) enter. The diagram in Fig. 2(h), for instance, is constructed by combining the diagram element representing r_i^{abc} in Table II with the diagram element representing $\langle ab | \bar{H} | cd \rangle$ in Table III.

Let us turn to the diagrams for two-particle removal. Figures 3 and 4 show the diagrams of $(\bar{H} \hat{R})_C$ for the two truncations of the 2PR-EOM-CCSD method. Here, topologies of the form $\langle \Phi_{ij} | (\bar{H} \hat{R})_C | \Phi_0 \rangle$ and $\langle \Phi_{ijk}^a | (\bar{H} \hat{R})_C | \Phi_0 \rangle$ are necessary, using the r_{ij} and r_{ijk}^a diagrams in Table II.

The algebraic expressions corresponding to these diagrams are derived according to the standard rules (see, for example,

TABLE III. Diagrams of the matrix elements of the similarity-transformed Hamiltonian \bar{H} . The horizontal wiggly line represents the operator vertex. The top three diagrams represent the one-body matrix elements of \bar{H} , the last four diagrams represent the three-body matrix elements of \bar{H} , and the remaining diagrams denote two-body matrix elements of \bar{H} , respectively. The corresponding algebraic expressions are shown in Table IV.

Matrix element	Diagram
$\langle i \bar{H} a\rangle$	
$\langle a \bar{H} b\rangle$	
$\langle i \bar{H} j\rangle$	
$\langle ai \bar{H} bc\rangle$	
$\langle ij \bar{H} ka\rangle$	
$\langle ab \bar{H} cd\rangle$	
$\langle ij \bar{H} kl\rangle$	
$\langle ia \bar{H} bj\rangle$	
$\langle ab \bar{H} ci\rangle$	
$\langle ia \bar{H} jk\rangle$	
$\langle abc \bar{H} dei\rangle$	
$\langle ija \bar{H} klm\rangle$	
$\langle aib \bar{H} cdj\rangle$	
$\langle ija \bar{H} kbl\rangle$	

Ref. [4]) and shown in Table VI. The computational cost is $n_u^5 n_o$ for the 2PA-EOM-CCSD (3P-1H) method, and the most expensive diagram is shown in Fig. 2(h). Likewise, the most expensive diagram for the 2PR-EOM-CCSD (1P-3H) is shown in Fig. 4(i) and requires of the order of $n_u^2 n_o^4$ operations. Here, n_u is the number of unoccupied orbitals (equal to the size of the valence space), and n_o is the number of occupied orbitals in the reference state. For comparison, the computational costs of the

TABLE IV. Algebraic expressions for the matrix elements of the similarity-transformed Hamiltonian in terms of the cluster amplitudes t_i^a and t_{ij}^{ab} , the matrix elements $\langle ij||ef\rangle$ of the two-body interaction, and the one-body matrix elements $f_q^p = \varepsilon_q^p + \sum_i \langle pi|v|qi\rangle$ of the normal-ordered Hamiltonian. The permutation operator \hat{P}_{pq} permutes the indices p and q , and we define $\hat{P}(pq) = 1 - \hat{P}_{pq}$, $\hat{P}(pq, r) = 1 - \hat{P}_{pr} - \hat{P}_{qr}$, and $\hat{P}(p, qr) = 1 - \hat{P}_{pq} - \hat{P}_{pr}$. The intermediates χ are defined in Table V.

Matrix element	Shorthand	Expression
$\langle i \bar{H} a\rangle$	\bar{H}_a^i	$f_a^i + \langle im ae\rangle t_m^e$
$\langle a \bar{H} b\rangle$	\bar{H}_b^a	$\chi_b^a - \frac{1}{2} \langle mn be\rangle t_{mn}^{ae} - t_m^a \bar{H}_b^m$
$\langle i \bar{H} j\rangle$	\bar{H}_j^i	$f_j^i + \langle im je\rangle t_m^e + \frac{1}{2} \langle im ef\rangle t_{jm}^{ef} + t_j^e \bar{H}_e^i$
$\langle ai \bar{H} bc\rangle$	\bar{H}_{bc}^{ai}	$\chi_{bc}^{ai} - \frac{1}{2} \langle mi bc\rangle t_m^a$
$\langle ij \bar{H} ka\rangle$	\bar{H}_{ka}^{ij}	$\chi_{ka}^{ij} + \frac{1}{2} \langle ij ea\rangle t_k^e$
$\langle ab \bar{H} cd\rangle$	\bar{H}_{cd}^{ab}	$\langle ab cd\rangle + \frac{1}{2} \langle mn cd\rangle t_{mn}^{ab} - \hat{P}(ab) t_m^b \chi_{cd}^{am}$
$\langle ij \bar{H} kl\rangle$	\bar{H}_{kl}^{ij}	$\langle ij kl\rangle + \frac{1}{2} \langle ij ef\rangle t_{kl}^{ef} + \hat{P}(kl) t_l^e \chi_{ke}^{ij}$
$\langle ia \bar{H} bj\rangle$	\bar{H}_{bj}^{ia}	$\chi_{bj}^{ia} + \frac{1}{2} \langle mi eb\rangle t_{jm}^{ae}$
$\langle ab \bar{H} ci\rangle$	\bar{H}_{ci}^{ab}	$\frac{1}{2} \langle ab ce\rangle t_i^e + \chi_{ci}^{ab} - t_{mi}^{ab} \bar{H}_c^m - \frac{1}{2} t_{mn}^{ab} \bar{H}_{ic}^{mn} + \hat{P}(ab) t_{mi}^{eb} \bar{H}_{ce}^{am} - \hat{P}(ab) t_m^a \chi_{ci}^{mb}$
$\langle ia \bar{H} jk\rangle$	\bar{H}_{jk}^{ia}	$\chi_{jk}^{ia} + t_{jk}^{ea} \bar{H}_e^i + \hat{P}(jk) t_{mk}^{ea} \bar{H}_{je}^{im} - \frac{1}{2} t_m^a \bar{H}_{jk}^{im}$
$\langle abc \bar{H} dei\rangle$	\bar{H}_{dei}^{abc}	$\hat{P}(a, bc) \langle mn de\rangle t_{ni}^{abc} - \hat{P}(a, bc) \langle am de\rangle t_{mi}^{bc}$
$\langle ija \bar{H} klm\rangle$	\bar{H}_{klm}^{ija}	$\hat{P}(k, lm) \langle ij ke\rangle t_{lm}^{ea} + \hat{P}(k, lm) \langle ij ef\rangle t_{kl}^{ef} t_{lm}^{fa} - \langle mi cd\rangle t_{mj}^{ab}$
$\langle aib \bar{H} cdj\rangle$	\bar{H}_{cdj}^{aib}	$\langle ij eb\rangle t_{kl}^{ea}$
$\langle ija \bar{H} kbl\rangle$	\bar{H}_{kbl}^{ija}	

TABLE V. The intermediates that enter the construction of the similarity-transformed Hamiltonian \bar{H} in Table IV. All other terms are defined in Table IV.

Intermediate	Expression
χ_b^a	$f_b^a + \langle am be\rangle t_m^e$
χ_{bc}^{ai}	$\langle ai bc\rangle - \frac{1}{2} \langle mi bc\rangle t_m^a$
χ_{ka}^{ij}	$\langle ij ka\rangle + \frac{1}{2} \langle ij ea\rangle t_k^e$
χ_{bj}^{ia}	$\langle ia bj\rangle + \frac{1}{2} \langle ai eb\rangle t_j^e$
χ_{bj}^{ia}	$\chi_{bj}^{ia} + \frac{1}{2} \langle ai eb\rangle t_j^e - \frac{1}{2} t_m^a \bar{H}_{jb}^{mi}$
χ_{bj}^{ia}	$\chi_{bj}^{ia} - \frac{1}{2} t_m^a \bar{H}_{jb}^{mi} + \frac{1}{2} \langle mi eb\rangle t_{jm}^{ae}$
χ_{ci}^{ab}	$\langle ab ci\rangle + \frac{1}{2} \langle ab ce\rangle t_i^e$
χ_{jk}^{ia}	$\langle ia jk\rangle + \frac{1}{2} \langle ia ef\rangle t_{jk}^{ef} + \hat{P}(jk) t_{jk}^{ea} \chi_{ek}^{ia} - \frac{1}{2} t_m^a \bar{H}_{jk}^{im}$

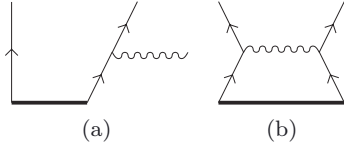


FIG. 1. Diagrams corresponding to the matrix element $\langle \Phi^{ab} | (\bar{H} \hat{R})_C | \Phi_0 \rangle$ for the 2PA-EOM-CCSD (2P-0H) amplitude equation. All diagrams are constructed by connecting a diagram from Table II, with a diagram from Table III. Only diagrams that satisfy the topological form of $\langle \Phi^{ab} | (\bar{H} \hat{R})_C | \Phi_0 \rangle$, with two external particle lines in the upper part of the diagram and no external lines in the bottom part of the diagram, are selected.

single-reference CCSD and CCSDT (which includes triples clusters) methods are $n_u^4 n_o^2$ and $n_u^5 n_o^3$, respectively. This shows that the 2PA(R)-EOM-CCSD methods developed in this work are relatively inexpensive from a computational point of view, and comparable to the cost of CCSD. Note that the three-body matrix elements of the similarity-transformed Hamiltonian are not stored. Instead, they are calculated when needed and do not contribute significantly to the overall cost of the calculations. For a detailed analysis we refer the reader to Refs. [35,36].

The eigenvalue problem of Eq. (10) for the two-particle-attached system thus becomes

$$\begin{aligned} \langle \Phi^{ab} | (\bar{H} \hat{R})_C | \Phi_0 \rangle &= \omega r^{ab} \\ \langle \Phi_i^{abc} | (\bar{H} \hat{R})_C | \Phi_0 \rangle &= \omega r_i^{abc}. \end{aligned} \quad (13)$$

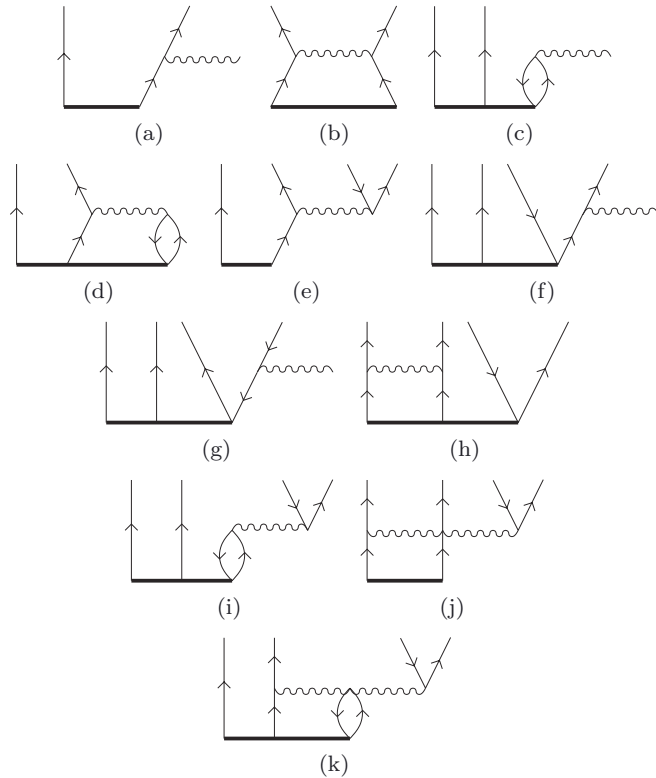


FIG. 2. Diagrams corresponding to the matrix elements $\langle \Phi^{ab} | (\bar{H} \hat{R})_C | \Phi_0 \rangle$, (a)–(d), and $\langle \Phi_i^{abc} | (\bar{H} \hat{R})_C | \Phi_0 \rangle$, (e)–(k), for the 2PA-EOM-CCSD (3P-1P) amplitude equation.

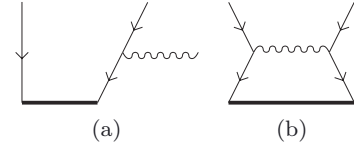


FIG. 3. Diagrams corresponding to the matrix element $\langle \Phi_{ij} | (\bar{H} \hat{R})_C | \Phi_0 \rangle$ for the 2PR-EOM-CCSD (0P-2H) amplitude equation. All diagrams are constructed by combining a diagram from Table II, with a diagram from Table III. Only diagrams that satisfy the topological form of $\langle \Phi_{ij} | (\bar{H} \hat{R})_C | \Phi_0 \rangle$, with two external hole lines in the upper part of the diagram and no external lines in the bottom part of the diagram, are selected.

Here, the left-hand side is a linear function of the vector $R = (r^{ab}, r_i^{abc})$ of amplitudes (Table VI) and constitutes a matrix-vector product. Note that the two equations are coupled and constitute a single eigenvalue problem for the 3P-1H truncation. Likewise, we find for the two-particle removed problem

$$\begin{aligned} \langle \Phi_{ij} | (\bar{H} \hat{R})_C | \Phi_0 \rangle &= \omega r_{ij} \\ \langle \Phi_{ijk}^a | (\bar{H} \hat{R})_C | \Phi_0 \rangle &= \omega r_{ijk}^a. \end{aligned} \quad (14)$$

We are usually only interested in the few lowest eigenvalues of Eq. (10). For this purpose, we use the Arnoldi method for asymmetric eigenvalue problems (see, for example, Ref. [37] and references therein). This method is based on repeated

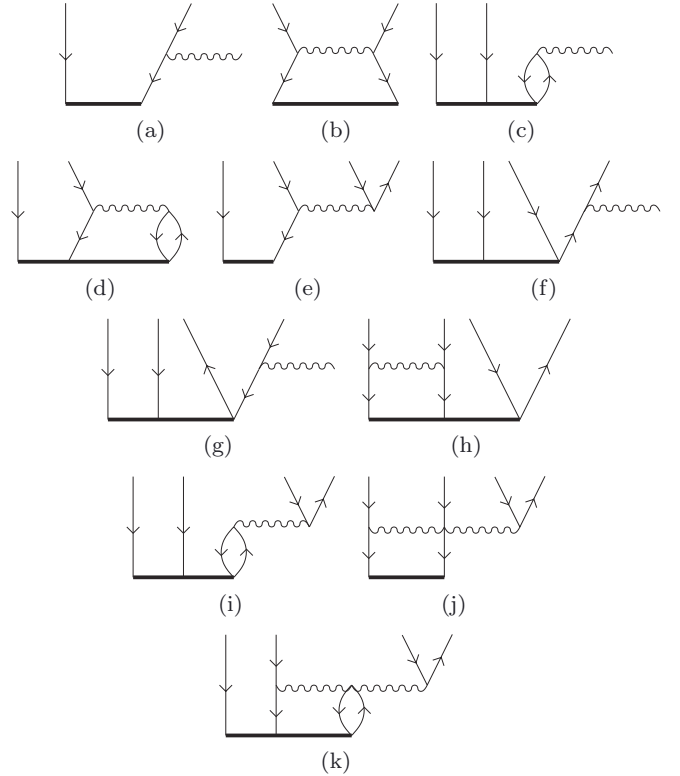


FIG. 4. Diagrams corresponding to the matrix elements $\langle \Phi_{ij} | (\bar{H} \hat{R})_C | \Phi_0 \rangle$ (a)–(d) and $\langle \Phi_{ijk}^a | (\bar{H} \hat{R})_C | \Phi_0 \rangle$ (e)–(k) for the 2PR-EOM-CCSD (1P-3H) amplitude equation.

TABLE VI. Algebraic expressions for the 2PA(R)-EOM-CCSD [2P-0H (0P-2H)] and 2PA(R)-EOM-CCSD [3P-1H (1P-3H)] approximations. All terms are defined in Table IV.

Matrix element	Expression
$\langle \Phi^{ab} (\tilde{H} \hat{R})_C \Phi_0 \rangle$	2PA-EOM-CCSD (2P-0H) $\hat{P}(ab) \tilde{H}_e^b r^{ae} + \frac{1}{2} \tilde{H}_{ef}^{ab} r^{ef}$
$\langle \Phi^{ab} (\tilde{H} \hat{R})_C \Phi_0 \rangle$	2PA-EOM-CCSD (3P-1H) $\hat{P}(ab) \tilde{H}_e^b r^{ae} + \frac{1}{2} \tilde{H}_{ef}^{ab} r^{ef}$ $+ \tilde{H}_e^m r_m^{abe} + \frac{1}{2} \hat{P}(ab) \tilde{H}_{ef}^{bm} r_m^{aef}$
$\langle \Phi_i^{abc} (\tilde{H} \hat{R})_C \Phi_0 \rangle$	$\hat{P}(a, bc) \tilde{H}_{ei}^{bc} r^{ae} + \hat{P}(ab, c) \tilde{H}_e^{c,abe} r_i^{efc}$ $- \tilde{H}_i^m r_m^{abc} + \frac{1}{2} \hat{P}(ab, c) \tilde{H}_{ef}^{ab} r_i^{efc}$ $+ \hat{P}(ab, c) \tilde{H}_{ei}^{mc} r_m^{abe} + \frac{1}{2} \tilde{H}_{efi}^{abc} r^{ef}$ $+ \frac{1}{2} \hat{P}(a, bc) \tilde{H}_{efi}^{bmc} r_m^{aef}$
$\langle \Phi_{ij} (\tilde{H} \hat{R})_C \Phi_0 \rangle$	2PR-EOM-CCSD (0P-2H) $-\hat{P}(ij) \tilde{H}_j^m r_{im} + \frac{1}{2} \tilde{H}_{ij}^{mn} r_{mn}$
$\langle \Phi_{ij} (\tilde{H} \hat{R})_C \Phi_0 \rangle$	2PR-EOM-CCSD (1P-3H) $-\hat{P}(ij) \tilde{H}_j^m r_{im} + \frac{1}{2} \tilde{H}_{ij}^{mn} r_{mn}$ $+ \tilde{H}_e^m r_{ijm}^e - \frac{1}{2} \hat{P}(ij) \tilde{H}_{je}^{mn} r_{imn}^e$ $-\hat{P}(i, jk) \tilde{H}_{jk}^{ma} r_{im} + \tilde{H}_e^a r_{ijk}^e$ $-\hat{P}(ij, k) \tilde{H}_k^m r_{ijm}^a + \frac{1}{2} \hat{P}(ij, k) \tilde{H}_{ij}^{mn} r_{mnk}^a$ $+ \hat{P}(ij, k) \tilde{H}_{ek}^{ma} r_{ijm}^e + \frac{1}{2} \tilde{H}_{ijk}^{mna} r_{mn}$ $-\frac{1}{2} \hat{P}(i, jk) \tilde{H}_{jek}^{mna} r_{imn}^e$

applications of the matrix-vector product $(\tilde{H} \hat{R})_C$. Specifically, our numerical implementation uses the ARPACK software [38] package. The expressions in Table VI can thus be used to solve the eigenvalue problem directly. In this paper, we employ the m -scheme basis for the vectors $R = (r^{ab}, r_i^{abc})$ of the 2PA method. Within this scheme, we are limited to small model spaces. However, in this work we are mainly interested in testing the developed methods and in gauging the accuracy of the employed cluster truncation through comparisons with exact diagonalization. Note that the similarity-transformed Hamiltonian \tilde{H} exhibits the symmetries of the underlying Hamiltonian. In the m -scheme basis, we can classify states by their projections J_z of angular momentum and T_z of isospin and their parity. Although the solutions will have a good total angular momentum \hat{J}^2 , we will not be able to exploit this symmetry in the m -scheme basis.

The FCI method we employ [39] is limited to relatively small model spaces. Note, however, that we are also working on an angular-momentum-coupled implementation [40] of the 2PA(R)-EOM-CCSD method. This will allow us to exploit rotational symmetries and give us access to much larger model spaces. These spaces are well beyond the reach of present full-diagonalization methods.

III. RESULTS

For the proof-of-principle study we consider the helium isotopes ^3He to ^6He . Here, ^3He and ^5He are viewed as one neutron removed from and attached to ^4He , respectively. In a shell-model picture, ^6He is a truly open-shell nucleus with

two valence neutrons in the $p_{3/2}$ shell. Thus, a single-reference Slater determinant may not be a good starting point for coupled-cluster calculations of this nucleus, and it seems advantageous to describe this six-nucleon system as two (halo) neutrons added to the ^4He core. We do not present results for ^2He using the 2PR-EOM-CCSD approach; an analysis of this method will be presented elsewhere [40].

For our calculations we use a realistic nucleon-nucleon (NN) potential derived from chiral effective field theory [41–45] at next-to-next-to-next-to-leading order using interaction matrix elements from Ref. [45]. The matrix elements of the bare interaction employ a cutoff at $\Lambda = 500$ MeV. The short-range parts of the interaction are removed via the similarity renormalization group transformation [46] with a cutoff at 1.9 fm^{-1} . We use the spherical harmonic oscillator with the oscillator frequency $\hbar\omega = 24$ MeV as our single-particle basis. Our model space consists of five major oscillator shells, with maximum orbital angular momentum $l_{\text{max}} = 2$. This results in a total of 76 single-particle states for neutrons and protons. We neglect three-body and four-body interactions. This leads to missing many-body physics but is not relevant for our proof-of-principle computation and comparison with FCI calculations.

We calculate the ground state energies of the $A = 3 - 6$ helium isotopes. For ^6He we also compute the first 2^+ state and the expectation values of the total angular momentum. In addition, we also discuss the first 1^- excited state, as an example where the 3P-1H truncation fails. We compare the EOM approach to the FCI method and to three different single-

TABLE VII. Ground-state energies (in MeV) for ^3He , ^4He , and ^5He , calculated with coupled-cluster methods truncated at the 2P-2H (CCSD) level, 3P-3H (CCSDT) level, and a hybrid (CCSDT-1) level where a small subset of the leading diagrams in CCSDT are included. For the EOM-CCSD approach, truncations has been made at the 1P-2H level, the 2P-2H level, and 2P-1H level for ^3He , ^4He , and ^5He , respectively. The energies are compared to the exact full configuration interaction (FCI).

	^3He	^4He	^5He
CCSD	-6.624	-27.468	-22.997
CCSDT-1	-6.829	-27.600	-23.381
CCSDT	-6.911	-27.619	-23.474
EOM-CCSD	-6.357	-27.468	-23.382
FCI	-6.911	-27.640	-23.640

reference coupled-cluster approximations. Recall that within the m scheme, one can also compute open-shell nuclei directly with the coupled-cluster method without resorting to EOM techniques. While such a direct approach may suffer from the lack of a good reference state (as is the case for the ground state of ^6He), the inclusion of more and more clusters must converge to the FCI results. Comparing the EOM-CCSD approach to these single-reference coupled-cluster calculations allows us to gauge the efficiency of the various coupled-cluster approximations.

The direct coupled-cluster calculations employ the CCSD approximation described above, the CCSDT approximation, and the CCSDT-1 approach, which includes some of the 3P-3H clusters of the full CCSDT approximation. For the EOM calculations, we use the CCSD wave function of ^4He as the reference wave function and employ the intrinsic Hamiltonian of Eq. (1) with $A = 3, 5, 6$ for $^3, 5, 6\text{He}$, respectively. We compare all results to an exact calculation done with the FCI approach, using the same interaction and model space. The ground-state energies of $^3\text{--}^5\text{He}$ are shown in Table VII. For ^3He , CCSDT becomes an exact method and agrees with FCI. Here, the single-reference coupled-cluster calculations are superior to the EOM-CCSD approach. Evidently, the weakly bound nucleus ^3He is not well described as a neutron removed from the tightly bound ^4He . This means, in turn, that correlations beyond 1P-2H excitations play a non-negligible role. For ^4He , the EOM-CCSD approach is identical to the CCSD approach. Here, triples corrections and full triples represent a significant improvement over the CCSD method, bringing the results close to the FCI ones. For ^5He , the EOM-CCSD method is superior to a single-reference CCSD calculation and competes well with the computationally more expensive triples correction CCSDT-1 method. Clearly, the valence neutron in ^5He is weakly correlated with the strongly bound ^4He core, and the PA-EOM-CCSD approach captures this state very well.

We turn to the open-shell nucleus ^6He and show our results in Table VIII. Here, the 2PA-EOM-CCSD (3P-1H) approach is clearly superior to the single-reference coupled-cluster approaches as it reproduces the energy and the spin of the ground state to a very good approximation. For the computation of the spin within the single-reference approaches, we compute the

TABLE VIII. Energies (in MeV) for the ground state and first excited state of ^6He and the expectation value of the total angular momentum, calculated with coupled-cluster methods truncated at the 2P-2H (CCSD) level, 3P-3H (CCSDT) level, and a hybrid (CCSDT-1) level where the 3P-3H amplitudes are treated perturbatively. The 2PA-EOM-CCSD results are calculated with a truncation at the 2PA-EOM-CCSD (2P-0H) level and at the 2PA-EOM-CCSD (3P-1H) level. All energies are compared to FCI results.

	0_1^+	2_1^+	$0^+ \langle J \rangle$	$2_1^+ \langle J \rangle$
CCSD	-22.732	-20.905	0.78	2
CCSDT-1	-24.617	-21.586	0.25	2
CCSDT	-24.530	-21.786	0.01	2
2PA-EOM-CCSD (2P-0H)	-21.185	-18.996	0	2
2PA-EOM-CCSD (3P-1H)	-24.543	-21.634	0	2
FCI	-24.853	-21.994	0	2

expectation value $\langle J^2 \rangle$ within the Hellmann-Feynman theorem and define $\langle J \rangle$ from the relation $\langle J^2 \rangle = \langle J \rangle(\langle J \rangle + 1)$. A direct computation within the CCSD or CCSDT approximations can only be based on a symmetry-breaking reference state. Clearly, 2P-2H excitations (CCSD) cannot restore the symmetry and we find that $\langle J \rangle = 0.78$ for the ground state of ^6He . Adding 3P-3H excitations (CCSDT approximation) almost restores the rotational symmetry, but some correlation energy is still missing. In the 2PA-EOM-CCSD approach, however, the rotational symmetry is preserved throughout the calculation and we obtain a very good approximation of the energy at a relatively low computational cost. As expected, the 2PA-EOM-CCSD (2P-0H) approach is less accurate than the 3P-1H approximation, since it is unable to simultaneously account for the correlations within the three-body system consisting of the two valence neutrons and the ^4He core. The ground state and the first excited 2_1^+ state of ^6He are both dominated by a configuration with two neutrons in the $p_{3/2}$ orbit. This is consistent with the shell-model picture of this nucleus. For the excited 2_1^+ state, the CCSD, CCSDT, and CCSDT-1 methods result in the correct value of the angular momentum due to the choice of reference state.

Let us define the fraction σ_{corr} of the correlation energy as

$$\sigma_{\text{corr}} = \frac{E_{2\text{PA}} - E_0}{E_{\text{FCI}} - E_0}. \quad (15)$$

Here $E_{2\text{PA}}$ is the energy from the 2PA-EOM-CCSD, E_{FCI} is the energy from the FCI, while E_0 is the energy expectation of the uncorrelated reference state $|\Phi_0\rangle$. Both $E_{2\text{PA}}$ and E_{FCI} are shown in Table VIII, and $E_0 = -16.807$ MeV. We also compute the norm

$$\mathcal{N} = \sum_{ab} |r^{ab}|^2 + \sum_{abi} |r_i^{ab}|^2. \quad (16)$$

The normalized squared weights

$$\begin{aligned} \rho_1^2 &\equiv \mathcal{N}^{-1} \sum_{ab} |r^{ab}|^2, \\ \rho_2^2 &\equiv \mathcal{N}^{-1} \sum_{abi} |r_i^{ab}|^2 \end{aligned} \quad (17)$$

TABLE IX. The relative correlation energy σ_{corr} defined in Eq. (15) for the lowest states with quantum numbers $J^\pi = 0^+$, 1^- , and 2^+ in ${}^6\text{He}$, respectively. The relative weights ρ_1 and ρ_2 of the 2P-0H and 3P-1H amplitudes, respectively, are defined in Eq. (17).

	σ_{corr}	ρ_1	ρ_2
0_1^+	0.96	0.84	0.16
1_1^-	0.64	0.34	0.66
2_1^+	0.93	0.81	0.19

fulfill $\rho_1^2 + \rho_2^2 = 1$ and measure the importance of the 2P-0H and 3P-1H amplitudes, respectively.

Table IX shows the relative correlation energies σ_{corr} and the relative weights ρ_1 and ρ_2 of the 2PA-EOM-CCSD (3P-1H) energy for the three lowest states with quantum numbers 0^+ , 1^- , and 2^+ of ${}^6\text{He}$, respectively. We see that the 2PA-EOM-CCSD energy accounts for more than 90% of the correlation energy for the 0^+ and 2^+ states, and that most of the weight is carried by the 2P-0H amplitude. The 1^- state, however, is not very accurately reproduced and much of the correlation energy is lacking. For this state, the 2PA-EOM-CCSD (3P-1H) energy is $E_{1^-} = -20.95$ MeV and deviates considerably from the FCI result $E_{1^-} = -23.26$ MeV. Consistent with this picture is the large weight carried by the 3P-1H amplitudes. For a converged computation, one would presumably also need to include 4P-2H or higher clusters. Inspection shows that the $J^\pi = 1^-$ state is dominated by two neutrons in the $0p_{3/2}$ single-particle state, but with an additional 1P-1H excitation of either a proton or a neutron to the $0p_{3/2}$ state or the $0p_{1/2}$ orbit. These 3P-1H configurations are energetically favored compared with a configuration with one neutron in the $0p_{3/2}$ state and one in the $0d_{5/2}$ state, a configuration which can also give a 1^- state. This explains why this state is dominated by the r_i^{abc} amplitudes. Note, finally, that we cannot expect a separation of the center-of-mass motion from the intrinsic dynamics in the small model space we considered [31,47]. Such a separation, if it exists, must be investigated further in larger model spaces. Thus, the low-lying 1^- state might also exhibit considerable admixtures with spurious center-of-mass excitation.

We have shown that EOM works very well for nuclei with two valence nucleons that are dominated by two-particle excitations on top of a correlated core. Moreover, the EOM wave function preserves the symmetries of the Hamiltonian and is expected to be useful in the computation of matrix elements besides the energy. Taking into account the low

computational cost of the EOM-CCSD methods as compared to the full CCSDT approach, our EOM approach is clearly well suited for these selected states. For states where more complicated particle-hole excitations are prominent, the various truncation schemes discussed here are insufficient and we will need additional correlations in the EOM operator to reach satisfactory results. The ground state of ${}^3\text{He}$ and the first excited 1^- state of ${}^6\text{He}$ discussed above, are examples of states where more complicated many-body correlations are needed.

IV. CONCLUSIONS AND FUTURE PERSPECTIVES

We have developed and implemented the equation-of-motion coupled-cluster method and performed microscopic calculations of helium isotopes with up to two valence nucleons outside the closed-shell alpha particle. The comparison with full configuration-interaction calculations shows that the equation-of-motion coupled-cluster methods yield accurate results for sufficiently simple states. The open-shell nucleus ${}^6\text{He}$, for instance, can be viewed and computed as two weakly correlated neutrons attached to the correlated core of ${}^4\text{He}$. The proof-of-principle calculations were performed in a reduced model space for a comparison with results from exact diagonalizations. We are working on implementing our formalism for the two-particle-attached (removed) equation-of-motion coupled-cluster methods in an angular momentum coupled basis. This will allow us to employ much larger model spaces. With this improvement, the first-principles computation of semimagic nuclei, single-particle energies, and effective two-particle interactions for the nuclear shell-model can be addressed.

ACKNOWLEDGMENTS

We thank Øyvind Jensen for several discussions. T.P. thanks the Institut für Kernphysik, Technische Universität Darmstadt, and the GSI Helmholtzzentrum für Schwerionenforschung for their hospitality. This work was supported in part by the US Department of Energy, Grants No. DE-FG02-96ER40963 (University of Tennessee), and No. DE-FC02-07ER41457 (UNEDF SciDAC), the Research Council of Norway, and the Alexander von Humboldt Stiftung. This research used computational resources of the Notur project in Norway and the National Center for Computational Sciences at Oak Ridge National Laboratory.

- [1] M. G. Mayer and J. H. D. Jensen, in *Nobel Lectures in Physics 1963–1970* (Elsevier, Amsterdam, 1972).
- [2] F. Coester and H. Kümmel, *Nucl. Phys.* **17**, 477 (1960).
- [3] H. Kümmel, K. H. Lührmann, and J. G. Zabolitzky, *Phys. Rep.* **36**, 1 (1978).
- [4] I. Shavitt and R. J. Bartlett, *Many-body methods in Chemistry and Physics* (Cambridge University Press, Cambridge, 2009).
- [5] H. Kamada *et al.*, *Phys. Rev. C* **64**, 044001 (2001).

- [6] K. Varga and Y. Suzuki, *Phys. Rev. C* **52**, 2885 (1995).
- [7] N. Barnea, W. Leidemann, and G. Orlandini, *Phys. Rev. C* **61**, 054001 (2000).
- [8] R. B. Wiringa and S. C. Pieper, *Annu. Rev. Nucl. Part. Sci.* **51**, 53 (2001).
- [9] P. Navrátil, S. Quaglioni, I. Stetcu, and B. R. Barrett, *J. Phys. G* **36**, 083101 (2009).

- [10] E. Epelbaum, H. Krebs, D. Lee, and Ulf-G. Meissner, *Phys. Rev. Lett.* **104**, 142501 (2010).
- [11] E. Epelbaum, H. Krebs, D. Lee, and Ulf-G. Meissner, *Eur. Phys. J. A* **45**, 335 (2010).
- [12] R. F. Bishop, M. F. Flynn, M. C. Boscá, E. Buendía, and R. Guardiola, *Phys. Rev. C* **42**, 1341 (1990).
- [13] J. H. Heisenberg and B. Mihaila, *Phys. Rev. C* **59**, 1440 (1999).
- [14] D. J. Dean and M. Hjorth-Jensen, *Phys. Rev. C* **69**, 054320 (2004).
- [15] G. Hagen, D. J. Dean, M. Hjorth-Jensen, and T. Papenbrock, *Phys. Lett. B* **656**, 169 (2007).
- [16] M. Horoi, J. R. Gour, M. Włoch, M. D. Ludvigito, B. A. Brown, and P. Piecuch, *Phys. Rev. Lett.* **98**, 112501 (2007).
- [17] G. Hagen, T. Papenbrock, D. J. Dean, and M. Hjorth-Jensen, *Phys. Rev. Lett.* **101**, 092502 (2008).
- [18] O. Sorlin and M. G. Porquet, *Prog. Part. Nucl. Phys.* **61**, 602 (2008).
- [19] R. Kanungo *et al.*, *Phys. Rev. Lett.* **102**, 152501 (2009).
- [20] M. Hjorth-Jensen, T. T. S. Kuo, and E. Osnes, *Phys. Rep.* **261**, 125 (1995).
- [21] B. A. Brown, *Prog. Part. Nucl. Phys.* **47**, 517 (2001).
- [22] M. Honma, T. Otsuka, B. A. Brown, and T. Mizusaki, *Phys. Rev. C* **69**, 034335 (2004).
- [23] M. Nooijen and J. G. Snijders, *Int. J. Quantum Chem.* **48**, 15 (1993).
- [24] M. Nooijen and R. J. Bartlett, *J. Chem. Phys.* **102**, 3629 (1995).
- [25] J. F. Stanton and J. Gauss, *J. Chem. Phys.* **103**, 1064 (1995).
- [26] A. I. Krylov, *Annu. Rev. Phys. Chem.* **59**, 433 (2008).
- [27] P. Piecuch, J. R. Gour, and M. Włoch, *Int. J. Quantum Chem.* **109**, 3268 (2009).
- [28] M. Włoch, D. J. Dean, J. R. Gour, M. Hjorth-Jensen, K. Kowalski, T. Papenbrock, and P. Piecuch, *Phys. Rev. Lett.* **94**, 212501 (2005).
- [29] J. R. Gour, P. Piecuch, M. Hjorth-Jensen, M. Włoch, and D. J. Dean, *Phys. Rev. C* **74**, 024310 (2006).
- [30] G. Hagen, T. Papenbrock, and M. Hjorth-Jensen, *Phys. Rev. Lett.* **104**, 182501 (2010).
- [31] G. Hagen, T. Papenbrock, D. J. Dean, and M. Hjorth-Jensen, *Phys. Rev. C* **82**, 034330 (2010).
- [32] M. Nooijen and R. J. Bartlett, *J. Chem. Phys.* **107**, 6812 (1997).
- [33] M. Wladyslawski and M. Nooijen, *Adv. Quant. Chem.* **49**, 1 (2005).
- [34] R. J. Bartlett, *Int. J. Mol. Sci.* **3**, 579 (2002).
- [35] S. A. Kucharski and R. J. Bartlett, *Adv. Quantum Chem.* **18**, 281 (1986).
- [36] G. Hagen, T. Papenbrock, D. J. Dean, A. Schwenk, A. Nogga, M. Włoch, and P. Piecuch, *Phys. Rev. C* **76**, 034302 (2007).
- [37] G. H. Golub and C. F. Van Loan, *Matrix Computations* (Johns Hopkins University Press, Baltimore, 1996).
- [38] R. B. Lehoucq, D. C. Sorensen, and Y. Yang, *ARPACK User's Guide: Solution to large scale eigenvalue problems with implicitly restarted Arnoldi methods* (SIAM Publications, Philadelphia, 1998); FORTRAN code available at [<http://www.caam.rice.edu/software/ARPACK>.]
- [39] T. Papenbrock and D. J. Dean, *Phys. Rev. C* **67**, 051303 (2003); T. Papenbrock, A. Juodagalvis, and D. J. Dean, *ibid.* **69**, 024312 (2004).
- [40] G. R. Jansen *et al.* (unpublished).
- [41] S. Weinberg, *Phys. Lett. B* **251**, 288 (1990).
- [42] S. Weinberg, *Nucl. Phys. B* **363**, 3 (1991).
- [43] P. Bedaque and U. van Kolck, *Annu. Rev. Nucl. Part. Sci.* **52**, 339 (2002).
- [44] E. Epelbaum, H.-W. Hammer, and U.-G. Meißner, *Rev. Mod. Phys.* **81**, 1773 (2009).
- [45] D. R. Entem and R. Machleidt, *Phys. Rev. C* **68**, 041001 (2003).
- [46] S. K. Bogner, R. J. Furnstahl, and R. J. Perry, *Phys. Rev. C* **75**, 061001 (2007).
- [47] G. Hagen, T. Papenbrock, and D. J. Dean, *Phys. Rev. Lett.* **103**, 062503 (2009).

Spherical coupled-cluster theory for open-shell nuclei

G. R. Jansen^{1,*}

¹*Department of Physics and Center of Mathematics for Applications, University of Oslo, N-0316 Oslo, Norway*

(Dated: 25th May 2012)

Background A microscopic description of nuclei is important to understand the nuclear shell-model from fundamental principles. This cannot be achieved without an effective approximation scheme, especially if three-nucleon forces are included.

Purpose Define and evaluate an approximation scheme that can be used to study nuclei that are described as two particles attached to a closed (sub-)shell nucleus.

Methods The equation-of-motion coupled-cluster formalism has been used to obtain ground and excited state energies. This method is based on the diagonalization of a non-Hermitian matrix obtained from a similarity transformation of the many-body nuclear Hamiltonian. A chiral interaction at the next-to-next-to-next-to leading order (N^3LO) using a cutoff at 500 MeV was used.

Results The ground state energies of ${}^6\text{Li}$ and ${}^6\text{He}$ were in good agreement with a no-core shell-model calculation using the same interaction. Several excited states were also produced with overall good agreement. Only the $J^\pi = 3^+$ excited state in ${}^6\text{Li}$ showed a sizeable deviation. The ground state energies of ${}^{18}\text{O}$, ${}^{18}\text{F}$ and ${}^{18}\text{Ne}$ were converged, but underbound compared to experiment. Also the calculated spectra were converged and comparable to both experiment and shell-model studies in this region. Some excited states in ${}^{18}\text{O}$ were high or missing in the spectrum.

Conclusions Converged results were obtained for all nuclei and the method can be used to describe nuclear states with simple structure. Especially the ground state energies were very close to an exact diagonalization. To obtain a closer match with experimental data, effects of three-nucleon forces, the scattering continuum as well as additional configurations in the coupled-cluster approximations, are necessary.

PACS numbers: 21.60.De, 21.10.Dr, 21.60.Gx, 31.15.bw

I. INTRODUCTION

In the past decade, the amount of computing resources made available for scientific research, has grown several orders of magnitude. This trend will continue during this decade, culminating in exascale computing facilities. This will promote new insights in every discipline as new problems can be solved and old problems can be solved faster and to a higher precision.

In nuclear physics, the long standing goal of a predictive theory, seems to approach fulfillment ever faster. However, complex obstacles have yet to be overcome. An exact solution to the nuclear many-body problem, is only possible for light nuclei (See Leidemann and Orlandini [1] for a recent review on many-body methods). With a finite basis expansion, a full diagonalization can currently be performed for nuclei in the p -shell region [2], with the possibility of approaching light sd -shell nuclei with sufficient computing resources. For *ab initio* access to larger nuclei, the problem has to be approached differently.

In coupled-cluster theory, a series of controlled approximations are performed to generate a similarity transformation of the nuclear Hamiltonian, where the ground state energy of a closed (sub-)shell reference nucleus is singled out. The similarity-transformed Hamiltonian is then diagonalized to calculate excited states and states of nuclei with one or more valence nucleons. This defines the equation-of-motion coupled-cluster (called EOM-CC

from now on) framework (see Bartlett and Musiał [3] for a recent review and Shavitt and Bartlett [4] for a textbook presentation). Recently, this method was applied to the oxygen [5] and the calcium [6] isotopic chains, extending the reach of *ab initio* methods in the medium mass region. Calculations in the nickel and tin regions are also planned.

In this work, we refine the EOM-CC method for two valence nucleons attached to a closed (sub-)shell reference. The general theory was presented in Jansen et al. [7], where calculations were performed in small model spaces. The working equations are now completely reworked in the spherical formalism, where analytical optimizations due to the rotational invariance of the Hamiltonian, enable calculations in large model spaces. This involves a fair bit of angular momentum algebra, where the potential for errors is quite large. We therefore explicitly include all equations and transformations that have been used in the spherical formalism for future reference.

Section II gives a brief overview of general coupled-cluster theory and the equation-of-motion extensions, emphasizing the parts that are necessary to develop the spherical scheme presented in Section III. In Section IV we discuss numerical results obtained for selected states in $A = 6$ and $A = 18$ systems, emphasizing the convergence properties. Finally, in Section V we present our conclusions and discuss the road ahead. We also include an appendix, where angular momentum transformations used in Section III are defined.

*Electronic address: g.r.jansen@fys.uio.no

II. COUPLED-CLUSTER THEORY

In this section we introduce the Hamiltonian that enters our calculation, a brief review of single reference coupled cluster-theory together with the equation-of-motion (EOM-CC) extensions to coupled cluster theory that allow the calculation of excited states. In this framework, also nuclei with different particle numbers can be approached by choosing the appropriate Slater determinant basis. We keep the presentation short and concentrate on the aspects important for deriving the spherical version of the 2PA-EOM-CCSD method presented in section III. The interested reader is referred to Shavitt and Bartlett [4] for details on coupled-cluster theory.

We use the intrinsic Hamiltonian

$$\hat{H} = \left(1 - \frac{1}{A^*}\right) \sum_{i=1}^A \frac{p_i^2}{2m} + \left[\sum_{i < j=1}^A \hat{v}_{ij} - \frac{\vec{p}_i \cdot \vec{p}_j}{mA^*} \right]. \quad (1)$$

Here A is the number of nucleons in the reference state, A^* is the mass number of the target nucleus, and \hat{v}_{ij} is the nucleon-nucleon interaction. We will limit ourselves to two-body interactions only. In second quantization, the Hamiltonian can be written as

$$\hat{H} = \sum_{pq} \varepsilon_q^p a_p^\dagger a_q + \frac{1}{4} \sum_{pqrs} \langle pq || rs \rangle a_p^\dagger a_q^\dagger a_s a_r. \quad (2)$$

The term $\langle pq || rs \rangle$ is a shorthand for the matrix elements (integrals) of the two-body part of the Hamiltonian of Eq. (1), p, q, r and s represent various single-particle states while ε_q^p stands for the matrix elements of the one-body operator in Eq. (1). Finally, second quantized operators like a_q^\dagger and a_p create and annihilate a nucleon in the state q and p , respectively. These operators fulfill the canonical anti-commutation relations.

A. Single-reference coupled-cluster theory

In single-reference coupled-cluster theory, the many-body ground-state $|\Psi_0\rangle$ is given by the exponential ansatz,

$$|\Psi_0\rangle = \exp(\hat{T})|\Phi_0\rangle. \quad (3)$$

Here, $|\Phi_0\rangle$ is the reference Slater determinant, where all states below the Fermi level are occupied and \hat{T} is the cluster operator that generates correlations. The operator \hat{T} is expanded as a linear combination of particle-hole excitation operators

$$\hat{T} = \hat{T}_1 + \hat{T}_2 + \dots + \hat{T}_A \quad (4)$$

where \hat{T}_n is the n -particle- n -hole(nP - nH) excitation operator

$$\hat{T}_n = \left(\frac{1}{n!}\right)^2 \sum_{a_\nu i_\nu} t_{i_1 \dots i_n}^{a_1 \dots a_n} a_{a_1}^\dagger \dots a_{a_n}^\dagger a_{i_n} \dots a_{i_1}. \quad (5)$$

Throughout this work we will use the convention that the indices $ijk\dots$ denote states below the Fermi level (holes), while the indices $abc\dots$ denote states above the Fermi level (particles). For an unspecified state, the indices $pqr\dots$ are used. The amplitudes $t_{i_1 \dots i_n}^{a_1 \dots a_n}$ will be determined by solving the coupled-cluster equations. In the singles and doubles approximation we truncate the cluster operator as

$$\hat{T} \approx \hat{T}_{\text{CCSD}} \equiv \hat{T}_1 + \hat{T}_2, \quad (6)$$

which defines the coupled-cluster approach with singles and doubles excitations, the so-called CCSD approximation. The unknown amplitudes result from the solution of the non-linear CCSD equations given by

$$\begin{aligned} \langle \Phi_i^a | \bar{H} | \Phi_0 \rangle &= 0, \\ \langle \Phi_{ij}^{ab} | \bar{H} | \Phi_0 \rangle &= 0. \end{aligned} \quad (7)$$

The term

$$\bar{H} = \exp(-\hat{T})\hat{H}\exp(\hat{T}) = \left(\hat{H}\exp(\hat{T})\right)_C, \quad (8)$$

is called the similarity-transform of the normal-ordered Hamiltonian, but (8) only defines a proper similarity transformation when the cluster operator (4) is used without truncation. The state $|\Phi_{ij\dots}^{ab\dots}\rangle$ is a Slater determinant that differs from the reference $|\Phi_0\rangle$ by holes in the orbitals $ij\dots$ and by particles in the orbitals $ab\dots$. The subscript C indicates that only connected diagrams enter.

Once the t_i^a and t_{ij}^{ab} amplitudes have been determined from Eq. (7), the correlated ground-state energy is given by

$$E_{\text{CC}} = \langle \Phi_0 | \bar{H} | \Phi_0 \rangle + E_0. \quad (9)$$

Here, E_0 denotes the vacuum expectation value with respect to the reference state.

The CCSD approximation is a very inexpensive method to obtain the ground state energy of a nucleus. In most cases however, the accuracy is not satisfactory [8]. The obvious solution would be to include triples excitations in Eq. (6) to define the CCSDT approximation. This leads to an additional set of non-linear equations

$$\langle \Phi_{ijk}^{abc} | \bar{H} | \Phi_0 \rangle = 0, \quad (10)$$

that has to be solved consistently. Unfortunately, such a calculation is very computationally expensive [9]. The computational cost of CCSDT scales as $n_o^3 n_u^5$, where n_o is the number of single-particle states occupied in the reference determinant and n_u are the number of unoccupied states. For comparison, the computational cost of the CCSD approximation scales as $n_o^2 n_u^4$.

Instead of solving the coupled-cluster equations (7) including triples excitations, we calculate a correction to the correlated ground state energy (9), using the Λ -CCSD(T) approach [10, 11]. Here, the

left-eigenvalue problem using the CCSD similarity-transformed Hamiltonian is solved, yielding a non-iterative triples correction to the ground state energy. The left-eigenvalue problem is given by

$$\langle \Phi_0 | \hat{\Lambda} \bar{H} = E \langle \Phi_0 | \hat{\Lambda}, \quad (11)$$

where $\hat{\Lambda}$ is a de-excitation operator,

$$\hat{\Lambda} = \hat{1} + \hat{\Lambda}_1 + \hat{\Lambda}_2, \quad (12)$$

and

$$\hat{\Lambda}_1 = \sum_{ia} \lambda_a^i a_a a_i^\dagger, \quad (13)$$

$$\hat{\Lambda}_2 = \sum_{ijab} \lambda_{ab}^{ij} a_b a_a a_i^\dagger a_j^\dagger. \quad (14)$$

The unknown amplitudes λ_a^i and λ_{ab}^{ij} are the components of the left-eigenvector with the lowest eigenvalue in Eq. (11). Once found, the energy correction is given by

$$\Delta E_3 = \frac{1}{(3!)^2} \sum_{ijkabc} \langle \Phi_0 | \hat{\Lambda} (\hat{F}_{hp} + \hat{V}_N) | \Phi_{ijk}^{abc} \rangle \times \frac{1}{\epsilon_{ijk}^{abc}} \langle \Phi_{ijk}^{abc} | (\hat{V}_N \hat{T}_2)_C | \Phi_0 \rangle. \quad (15)$$

Here, \hat{F}_{hp} is the part of the normal-ordered one-body Hamiltonian that annihilates particles and creates holes. The energy denominator is defined as

$$\epsilon_{ijk}^{abc} \equiv f_{ii} + f_{jj} + f_{kk} - f_{aa} - f_{bb} - f_{cc}, \quad (16)$$

where f_{pp} are the diagonal elements of the normal ordered one-body Hamiltonian \hat{F} .

Using this approach, the ground state wave function (3) and the similarity transformed Hamiltonian (8) are calculated using the CCSD approximation, while the ground state energy is given by

$$E_{\text{ACC}} = E_{\text{CC}} + \Delta E_3 \quad (17)$$

This approximation has proven to give very accurate results for closed (sub-)shell nuclei [12].

B. Equation-of-motion coupled-cluster(EOM-CC)

In nuclear physics, the single reference coupled cluster method defined by the coupled-cluster equations(7), is normally used to obtain the ground state energy of a closed (sub-)shell nucleus. While it is possible to apply the CC method to any reference determinant to obtain the energy of different states, the equation-of-motion coupled-cluster (EOM-CC) framework is usually employed for such endeavors.

When the cluster operator (4) is used without truncation, Eq. (8) defines a similarity transformation. This

guarantees that the eigenvalues of \bar{H} are equivalent to the eigenvalues of the intrinsic Hamiltonian (1) and that the eigenvectors are connected by the transformation defined by Eq. (3). When the cluster operator (4) is truncated, as in the CCSD approximation, Eq. (8) is an approximation to a similarity transformation. This means that the eigenvalues of \bar{H} are now only approximations to the exact eigenvalues. This is the foundation of the EOM-CC approach.

To simplify the equations and for effective calculations, we define the eigenvalue problem in the EOM-CC approach to be that of the difference between a target state and the coupled cluster ground state (3). Formally, a general state of the A -body nucleus is written

$$|\Psi_\mu\rangle = \hat{\Omega}_\mu |\Psi_0\rangle = \hat{\Omega}_\mu e^{\hat{T}} |\Phi_0\rangle. \quad (18)$$

Here $\hat{\Omega}_\mu$ is an excitation operator that creates the state $|\Psi_\mu\rangle$, when applied to the coupled cluster ground state $|\Psi_0\rangle$. The label μ identifies the quantum numbers(energy, angular momentum, ...) of the target state. The Schrödinger equations for the target state and the coupled-cluster ground state are written

$$\hat{H} \hat{\Omega}_\mu e^{\hat{T}} |\Phi_0\rangle = E_\mu \hat{\Omega}_\mu e^{\hat{T}} |\Phi_0\rangle \quad (19)$$

$$\hat{H} e^{\hat{T}} |\Phi_0\rangle = E_{\text{CC}} e^{\hat{T}} |\Phi_0\rangle. \quad (20)$$

Here E_μ is the energy of the target state and E_{CC} is the coupled-cluster reference energy in Eq. (9).

We can now multiply Eq. (19) by $e^{-\hat{T}}$ and Eq. (20) by $\hat{\Omega}_\mu e^{-\hat{T}}$ from the left and take the difference between the two equations

$$[\bar{H}, \hat{\Omega}_\mu] |\Psi_0\rangle = \omega_\mu \hat{\Omega}_\mu |\Psi_0\rangle, \quad (21)$$

where $\omega_\mu = E_\mu - E_{\text{CC}}$ and we have used that $[\hat{\Omega}_\mu, \hat{T}] = 0$. Finally, none of the unconnected terms in the evaluation of the commutator survive, resulting in

$$(\bar{H} \hat{\Omega}_\mu)_C |\Phi_0\rangle = \omega_\mu \hat{\Omega}_\mu |\Phi_0\rangle. \quad (22)$$

This operator equation can be posed as a matrix eigenvalue problem where ω_μ are the eigenvalues and the matrix elements of $\hat{\Omega}_\mu$ are the components of the eigenvectors. The subscript C implies that only terms where \bar{H} and $\hat{\Omega}_\mu$ are connected by at least one contraction survive. In diagrammatic terms, this means that only connected diagrams appear in the operator product $(\bar{H} \hat{\Omega}_\mu)_C$.

The similarity-transformed Hamiltonian (8) is a non-hermitian operator and is diagonalized by the scheme formulated by the Arnoldi algorithm(for details see for example Golub and Van Loan [13]). This scheme relies on the repeated application of the connected matrix vector product defined by Eq. (22). A left-eigenvalue problem is solved to obtain the conjugate eigenvectors [14], but this is beyond the scope of this article.

To find the explicit expressions for the connected matrix vector product, the excitation operator must be properly defined. When used for excited states of an A -body nucleus, the excitation operator in Eq. (18) is parametrized in terms of n P- n H operators. We define

$$\hat{\Omega}_\mu = \hat{R} = \hat{1} + \hat{R}_1 + \hat{R}_2 + \dots \hat{R}_A, \quad (23)$$

where

$$\hat{R}_n = \frac{1}{(n!)^2} \sum_{\substack{i_1, \dots, i_n \\ a_1, \dots, a_n}} r_{i_1 \dots i_n}^{a_1 \dots a_n} a_{a_1}^\dagger \dots a_{a_n}^\dagger a_{i_n} \dots a_{i_1}. \quad (24)$$

The unknown amplitudes r (sub and superscripts dropped) are the matrix elements of \hat{R} ,

$$r_{i_1 \dots i_n}^{a_1 \dots a_n} = \langle \Phi_{i_1 \dots i_n}^{a_1 \dots a_n} | \hat{R} | \Phi_0 \rangle, \quad (25)$$

and can be grouped into a vector that solves the eigenvalue problem in Eq. (22). The matrix vector product is found by looking at each individual element

$$\left(\bar{H} \hat{R} \right)_{i_1 \dots i_n}^{a_1 \dots a_n} \equiv \langle \Phi_{i_1 \dots i_n}^{a_1 \dots a_n} | \left(\bar{H} \hat{R} \right)_C | \Phi_0 \rangle, \quad (26)$$

and find the appropriate expressions using a diagrammatic approach.

Calculations using the full excitation operator (23), are not computationally tractable, so an additional level of approximation is introduced by a truncation. When the CCSD approximation is used to obtain the reference wave function, the excitation operator is truncated at the 2P-2H level [15] and defines EOM-CCSD.

In the EOM-CC approach, the states of $A \pm k$ nuclei are also treated as excited states of an A -body nucleus. We write

$$|\Psi_\mu^{A \pm k}\rangle = \hat{\Omega}_\mu |\Psi_0^{(A)}\rangle = \hat{\Omega}_\mu e^{\hat{T}} |\Phi_0\rangle. \quad (27)$$

The operator $\hat{\Omega}_\mu$ and the energies E_μ of the target state, also solve the eigenvalue problem in Eq. (22). The energy difference $\omega_\mu = E_\mu - E_0^*$ is now the excitation energy of the target state in the nucleus $A \pm k$, with respects to the closed-shell reference nucleus with the mass shift $A^* = A \pm k$ in the Hamiltonian (1). This mass shift ensures the correct kinetic energy of the center-of-mass is used in computing the $A \pm k$ nuclei.

The operators

$$\hat{\Omega}_\mu = \hat{R}^{A \pm 1} = \hat{R}_1^{A \pm 1} + \hat{R}_2^{A \pm 1} + \dots \hat{R}_A^{A \pm 1} \quad (28)$$

where

$$\begin{aligned} \hat{R}_n^{A+1} &= \frac{1}{(n!)(n-1)!} \sum_{\substack{i_1, \dots, i_{n-1} \\ a_1, \dots, a_n}} r_{i_1 \dots i_{n-1}}^{a_1 \dots a_n} \\ &\times a_{a_1}^\dagger \dots a_{a_n}^\dagger a_{i_{n-1}} \dots a_{i_1} \end{aligned} \quad (29)$$

$$\begin{aligned} \hat{R}_n^{A-1} &= \frac{1}{(n!)(n-1)!} \sum_{\substack{i_1, \dots, i_n \\ a_1, \dots, a_{n-1}}} r_{i_1 \dots i_n}^{a_1 \dots a_{n-1}} \\ &\times a_{a_1}^\dagger \dots a_{a_{n-1}}^\dagger a_{i_n} \dots a_{i_1} \end{aligned} \quad (30)$$

define the particle attached equation-of-motion coupled-cluster [16] (PA-EOM-CC) and the particle removed equation-of-motion coupled-cluster [17] (PR-EOM-CC) approaches. These methods have been used successfully in quantum chemistry for some time (see Bartlett and Musial [3] for a review), but have also recently been implemented for use in nuclear structure calculations [18].

In Jansen et al. [7] we defined the 2PA-EOM-CCSD and 2PR-EOM-CCSD methods for two particle attached to and removed from a closed (sub-)shell nucleus. For this problem, the excitation operators were given by

$$\hat{\Omega}_\mu = \hat{R}^{A \pm 2} = \hat{R}_2^{A \pm 2} + \hat{R}_3^{A \pm 2} + \dots \hat{R}_A^{A \pm 2} \quad (31)$$

where

$$\begin{aligned} \hat{R}_n^{A+2} &= \frac{1}{(n!)(n-2)!} \sum_{\substack{i_1, \dots, i_{n-2} \\ a_1, \dots, a_n}} r_{i_1 \dots i_{n-2}}^{a_1 \dots a_n} \\ &\times a_{a_1}^\dagger \dots a_{a_n}^\dagger a_{i_{n-2}} \dots a_{i_1} \end{aligned} \quad (32)$$

$$\begin{aligned} \hat{R}_n^{A-2} &= \frac{1}{(n!)(n-2)!} \sum_{\substack{i_1, \dots, i_n \\ a_1, \dots, a_{n-2}}} r_{i_1 \dots i_n}^{a_1 \dots a_{n-2}} \\ &\times a_{a_1}^\dagger \dots a_{a_{n-2}}^\dagger a_{i_n} \dots a_{i_1}. \end{aligned} \quad (33)$$

In this article, our focus is on the 2PA-EOM-CCSD method, where we truncate the operator at the 3P-1H level. This approximation is suitable for states with a dominant 2P structure. It is already computationally intensive with up to 10^9 basis states for the largest nuclei attempted. A full inclusion of 4P-2H amplitudes is therefore not feasible at this time.

C. Spherical coupled cluster theory

For nuclei with closed (sub-)shell structure, the reference state has good spherical symmetry and zero total angular momentum. For these systems, the cluster operator (4) is a scalar under rotation and depends only on reduced amplitudes. Thus,

$$\hat{T}_1 = \sum_{ia} t_i^a(J) [a_a^\dagger(J) \otimes \tilde{a}_i(J)]^0$$

and

$$\hat{T}_2 = \sum_{ijabJ} t_{ij}^{ab}(J) \left[[a_a^\dagger(j_a) \otimes a_b^\dagger(j_b)]^J \otimes [\tilde{a}_j(j_j) \otimes \tilde{a}_i(j_i)]^J \right]^0,$$

where the amplitudes $t(J)$ (sub- and superscript dropped) are a short form of the reduced matrix elements of the cluster operator (4) (See appendix A for details). Also, J is a label specifying the total angular momentum of a many-body state and standard tensor notation has been used to specify the tensor couplings.

As the similarity-transformed Hamiltonian (8) is a product of three scalar operators (remember that the exponential of an operator is defined in terms of its Taylor

expansion), it is also a scalar under rotation. This allows a formulation of the coupled-cluster equations that is completely devoid of magnetic quantum numbers, thus reducing the size of the single-particle space and the number of coupled non-linear equations to solve in Eq. (7). For further details, see Hagen et al. [12].

Within the same formalism, we wish to establish the connected operator product in Eq. (22). This will greatly reduce the computational cost of calculating the product, but also allow a major reduction in both the single-particle basis and the number of allowed configurations in the many-body basis.

Given a target state with total angular momentum J (in units of $\hbar c$), the excitation operator, $\Omega_\mu(18)$, is a spherical tensor operator by definition (see for example Bohr and Mottelson [19]). It has a rank of J , with $2J+1$ components labelled by the magnetic quantum number $M \in [-J, \dots, J]$. We write

$$\Omega_\mu = \hat{R}_\mu^{A\pm k}(J, M), \quad (34)$$

where A is the number of particles in the reference state, $A\pm k$ is the number of particles in the target state, while μ identifies a specific set of quantum numbers. Identifying the excitation operator as a spherical tensor operator, invokes an extensive machinery of angular momentum algebra with important theorems. Of special importance is the Wigner-Eckart theorem (see for example Edmunds [20]), which states that the matrix elements of a spherical tensor operator can be factorized into two parts. The first is a geometric part identified by a Clebsch-Gordon coefficient, while the second is a reduced matrix element that does not depend on the magnetic quantum numbers.

To derive the spherical form of any EOM-CCSD method, a suitable spherical many-body basis has to be defined. The Slater determinant basis where we use the particle-hole formalism is substituted with the standard form. That means that for a general operator \hat{O} , we will write

$$\langle ab|\hat{O}|ij\rangle \equiv \langle \Phi_{ij}^{ab}|\hat{O}|\Phi_0\rangle, \quad (35)$$

where the single-particle states labelled a and b are occupied in the outgoing state, while the single-particle states labelled i and j are occupied in the incoming state. All single-particle states shared between the incoming and outgoing many-body state are dropped from the notation.

In general form, we write a component of the spherical basis as

$$|\alpha; J_\alpha M_\alpha\rangle, \quad (36)$$

where α denotes a particular many-body state, while $J_\alpha(M_\alpha)$ is the total angular momentum (projection) of this state. Using the spherical notation, the matrix elements of the excitation operator are written

$$r_\beta^\alpha(J_\alpha, J_\beta) = \langle \alpha; J_\alpha M_\alpha | \hat{R}_M^J | \beta; J_\beta M_\beta \rangle, \quad (37)$$

where we have dropped the cumbersome sub- and superscripts on the excitation operator in favour of standard tensor notation. The matrix elements of the matrix vector product in Eq. (22) are written

$$\langle \alpha; J_\alpha M_\alpha | \left(\bar{\mathbf{H}} \hat{\mathbf{R}}_M^J \right)_C | \beta; J_\beta M_\beta \rangle = \omega \langle \alpha; J_\alpha M_\alpha | \hat{\mathbf{R}}_M^J | \beta; J_\beta M_\beta \rangle. \quad (38)$$

Now, the Wigner-Eckart theorem allows a factorization of the matrix elements into two factors

$$C_{MM_\beta M_\alpha}^{JJ_\beta J_\alpha} \langle \alpha; J_\alpha || \left(\bar{\mathbf{H}} \hat{\mathbf{R}}^J \right)_C || \beta; J_\beta \rangle = \omega C_{MM_\beta M_\alpha}^{JJ_\beta J_\alpha} \langle \alpha; J_\alpha || \hat{\mathbf{R}}^J || \beta; J_\beta \rangle. \quad (39)$$

Here, $C_{MM_\beta M_\alpha}^{JJ_\beta J_\alpha}$ is a Clebsch-Gordon coefficient and the double bars denote reduced matrix elements and does not depend on any of the projection quantum numbers. This equation is simplified by dividing by the Clebsch-Gordon coefficient. This means that for each set of α, β, J_α and J_β , where J, J_α and J_β satisfy the triangular condition, there are $(2J+1) \times (2J_\alpha+1) \times (2J_\beta+1)$ identical equations for a given J . Of course, we only need one to solve the eigenvalue problem, resulting in a significantly smaller dimensionality. We are left with an eigenvalue problem where the unknown components of the eigenvectors are the reduced matrix elements of the excitation operator

$$\langle \alpha; J_\alpha || \left(\bar{\mathbf{H}} \hat{\mathbf{R}}^J \right)_C || \beta; J_\beta \rangle = \omega \langle \alpha; J_\alpha || \hat{\mathbf{R}}^J || \beta; J_\beta \rangle. \quad (40)$$

The eigenvalue problem in Eq. (40) is the spherical formulation of the general EOM-CC diagonalization problem. For a given excitation operator, both the connected operator product and the reduced amplitudes must be defined explicitly.

III. DERIVATION OF SPHERICAL 2PA-EOM-CCSD

In this work we derive the spherical formulation of the 2PA-EOM-CCSD [7] method, where the excitation operator in Eq. (31) has been truncated at the 3P-1H level. We write

$$\hat{\mathbf{R}} = \frac{1}{2} \sum_{ab} r^{ab} a_a^\dagger a_b^\dagger + \frac{1}{6} \sum_{abci} r_i^{abc} a_a^\dagger a_b^\dagger a_c^\dagger a_i, \quad (41)$$

where we have dispersed with the cumbersome sub- and subscripts in the operator.

The unknown amplitudes r are the matrix elements of $\hat{\mathbf{R}}$ and defined by

$$r^{ab} = \langle \Phi^{ab} | \hat{\mathbf{R}} | \Phi_0 \rangle \equiv \langle ab | \hat{\mathbf{R}} | 0 \rangle$$

$$r_i^{abc} = \langle \Phi_i^{abc} | \hat{\mathbf{R}} | \Phi_0 \rangle \equiv \langle abc | \hat{\mathbf{R}} | i \rangle, \quad (42)$$

while we define a shorthand form of the components of the matrix-vector product by

$$\left(\bar{\mathbf{H}}\hat{\mathbf{R}}\right)^{ab} = \langle \Phi^{ab} | \left(\bar{\mathbf{H}}\hat{\mathbf{R}}\right)_C | \Phi_0 \rangle \quad (43)$$

$$\left(\bar{\mathbf{H}}\hat{\mathbf{R}}\right)_i^{abc} = \langle \Phi_i^{abc} | \left(\bar{\mathbf{H}}\hat{\mathbf{R}}\right)_C | \Phi_0 \rangle. \quad (44)$$

The eigenvalue problem in Eq. (22) can now be posed in terms of the individual equations

$$\begin{aligned} \left(\bar{\mathbf{H}}\hat{\mathbf{R}}\right)^{ab} &= \omega r^{ab} \\ \left(\bar{\mathbf{H}}\hat{\mathbf{R}}\right)_i^{abc} &= \omega r_i^{abc}. \end{aligned} \quad (45)$$

In the spherical formulation, the excitation operator is a spherical tensor operator of rank J and projection M ,

$$\begin{aligned} \hat{\mathbf{R}}_M^J &= \frac{1}{2} \sum_{ab} r^{ab}(J) \left[a_a^\dagger(j_a) \otimes a_b^\dagger(j_b) \right]_M^J \\ &\quad + \frac{1}{6} \sum_{\substack{abci \\ J_{ab}J_{abc}}} r_i^{abc}(J, J_{abc}, J_{ab}) \\ &\quad \times \left[\left[a_a^\dagger(j_a) \otimes a_b^\dagger(j_b) \right]^{J_{ab}} \otimes a_c^\dagger(j_c) \right]^{J_{abc}} \otimes \tilde{a}_i(j_i) \Big]_M^J. \end{aligned} \quad (46)$$

Here the $a_a^\dagger(j_a)$ and $\tilde{a}_i(j_i)$ are spherical tensor operators of rank j_a and j_i respectively, where the latter is the time-reversed operator of $a_i^\dagger(j_i)$. Standard tensor notation has been used to define the spherical tensor couplings. The reduced amplitudes are now the reduced matrix elements of the spherical excitation operator (46). We write

$$r^{ab}(J) = \langle ab; j_a j_b; J | \hat{\mathbf{R}}^J | 0 \rangle, \quad (47)$$

where j_a and j_b are coupled to J in left to right order. Also

$$r_i^{abc}(J, J_{abc}, J_{ab}) = \langle abc; j_a j_b; J_{ab} j_c; J_{abc} | \hat{\mathbf{R}}^J | i; j_i \rangle, \quad (48)$$

where we have coupled the angular momentums j_a and j_b to J_{ab} , as well as J_{ab} and j_c to J_{abc} , also in left to right order. The shorthand form of the reduced matrix elements of the connected operator product is defined analogously by

$$\left(\bar{\mathbf{H}}\hat{\mathbf{R}}^J\right)^{ab}(J) = \langle ab; j_a j_b; J | \left(\bar{\mathbf{H}}\hat{\mathbf{R}}^J\right)_C | 0 \rangle \quad (49)$$

and

$$\begin{aligned} \left(\bar{\mathbf{H}}\hat{\mathbf{R}}^J\right)_i^{abc}(J, J_{abc}, J_{ab}) &= \\ \langle abc; j_a j_b; J_{ab} j_c; J_{abc} | \left(\bar{\mathbf{H}}\hat{\mathbf{R}}^J\right)_C | i; j_i \rangle. \end{aligned} \quad (50)$$

The transformations that connect the reduced matrix elements of $\hat{\mathbf{R}}^J$ with the uncoupled matrix elements are given in Eqs. (A16)-(A19).

The spherical eigenvalue problem (40) can now be written

$$\begin{aligned} \left(\bar{\mathbf{H}}\hat{\mathbf{R}}^J\right)^{ab}(J) &= \omega r^{ab}(J) \\ \left(\bar{\mathbf{H}}\hat{\mathbf{R}}^J\right)_i^{abc}(J, J_{abc}, J_{ab}) &= \omega r_i^{abc}(J, J_{abc}, J_{ab}), \end{aligned} \quad (51)$$

where the amplitudes are now the reduced matrix elements defined above.

In Table I we list the main result of this section. The first column lists all possible diagrams that contribute to the matrix-vector product in Eqs. (45), and (51). The other two columns contain the closed form expressions for these diagrams, in both the uncoupled and in the spherical representation. All matrix elements and amplitudes are defined in appendix A, while the permutation operators $\hat{P}(a, b)$ and $\hat{P}(ab, c)$ are defined in appendix B. Note that in the spherical representation the permutation operators also change the coupling order.

The last two diagrams contain the three-body parts of the similarity-transformed Hamiltonian (8) and have been joined in the spherical representation. The details of this merger and the definition of the intermediate operator $\hat{\chi}$ are contained in appendix C.

Let us briefly discuss how we arrive at the spherical diagram expressions, where we will use the first diagram in Table I as an example. This diagram contributes to the 2P matrix elements defined in Eq. (43) in the uncoupled representation and to the reduced matrix elements defined in Eq. (49) in the spherical representation.

The first step is to use the transformation in Eq. (A16) to write the reduced matrix elements (49) in terms of the uncoupled matrix elements (43). This gives us

$$\left(\bar{\mathbf{H}}\hat{\mathbf{R}}^J\right)^{ab}(J) = \frac{1}{\hat{j}_2} \sum_{M m_a m_b} C_{m_a m_b M}^{j_a j_b J} \left(\bar{\mathbf{H}}\hat{\mathbf{R}}\right)^{ab}, \quad (52)$$

where we introduce the notation $\hat{J} = \sqrt{2J+1}$. The diagram contributions to the uncoupled matrix elements are given by

$$\left(\bar{\mathbf{H}}\hat{\mathbf{R}}\right)^{ab} \leftarrow \hat{P}(ab) \bar{\mathbf{H}}_e^b r^{ae}, \quad (53)$$

where we let the arrow indicate that this is only one of several contributions to this matrix element. Here, $\bar{\mathbf{H}}_e^b$ is a matrix element of the one-body part of the similarity-transformed Hamiltonian (8) and both $\bar{\mathbf{H}}_e^b$ and r^{ae} are in the uncoupled representation.

Second, we insert Eq. (53) into Eq. (52) and get

$$\left(\bar{\mathbf{H}}\hat{\mathbf{R}}\right)^{ab}(J) \leftarrow \frac{1}{\hat{j}_2} \sum_{M m_a m_b} C_{m_a m_b M}^{j_a j_b J} \bar{\mathbf{H}}_e^b r^{ae} \quad (54)$$

Note that for the moment, we have ignored the permutation operator $\hat{P}(ab)$ that is a part of the diagram. We will discuss this later.

Diagram	Uncoupled expression	Coupled expression
	$\hat{P}(ab)\bar{H}_e^b r^{ae}$	$\hat{P}(ab)\bar{H}_e^b(j_b)r^{ae}(J)$
	$\frac{1}{2}\bar{H}_{ef}^{ab}r^{ef}$	$\frac{1}{2}\bar{H}_{ef}^{ab}(J)r^{ef}(J)$
	$\bar{H}_e^m r_m^{abe}$	$\sum_{J_{abe}} \bar{H}_e^m(j_e)r_m^{abe}(J_{ab}, J_{abe}, J) \frac{j_{abe}^2}{j^2}$
	$\frac{1}{2}\hat{P}(ab)\bar{H}_{ef}^{bm}r_m^{aef}$	$\frac{1}{2}\hat{P}(ab)\sum_{J_{efb}, J_{ef}}(-1)^{1+j_b+j_m-J_{ef}-J}\frac{j_{efb}^2 j_{ef}}{J}\left\{\begin{matrix} j_b & j_a & J \\ j_m & J_{efb} & J_{ef} \end{matrix}\right\}$ $\times \bar{H}_{ef}^{am}(J_{ef})r_m^{efb}(J_{ef}, J_{efb}, J)$
	$\hat{P}(a, bc)\bar{H}_{ei}^{bc}r^{ae}$	$\hat{P}(ab, c)(-1)^{1+j_c+j_i+J_{ab}-J}\hat{J}_{ab}\hat{J}\left\{\begin{matrix} j_c & j_e & J \\ j_i & J_{abc} & J_{ab} \end{matrix}\right\}\bar{H}_{ab}^{ei}(J_{ab})r^{ec}(J)$
	$\hat{P}(ab, c)\bar{H}_e^c r_i^{abe}$	$\hat{P}(ab, c)\bar{H}_e^c(j_c)r_i^{abe}(J_{ab}, J_{abe}, J)$
	$-\bar{H}_i^m r_m^{abc}$	$-\bar{H}_i^m(j_i)r_m^{abc}(J_{ab}, J_{abc}, J)$
	$\frac{1}{2}\hat{P}(ab, c)\bar{H}_{ef}^{ab}r_i^{efc}$	$\frac{1}{2}\hat{P}(ab, c)\bar{H}_{ef}^{ab}(J_{ab})r_i^{efc}(J_{ab}, J_{abc}, J)$
	$\hat{P}(ab, c)\bar{H}_{ei}^{mc}r_m^{abe}$	$\hat{P}(ab, c)\sum_{J_{abe}, J_{mc}}(-1)^{1+j_e+j_m+J_{abe}+J_{abc}+J_{mc}}\hat{J}_{abe}^2\hat{J}_{mc}^2\left\{\begin{matrix} J_{ab} & j_e & J_{abe} \\ j_c & J_{mc} & j_m \\ J_{abc} & j_i & J \end{matrix}\right\}$ $\times \bar{H}_{ei}^{mc}(J_{mc})r_m^{abe}(J_{ab}, J_{abe}, J)$
	$\frac{1}{2}\bar{H}_{efi}^{abc}r^{ef}$	$(-1)^{1+j_c+j_m-J}\hat{J}\hat{J}_{ab}\left\{\begin{matrix} j_c & j_m & J \\ j_i & J_{abc} & J_{ab} \end{matrix}\right\}\chi_m^c(J)t_{im}^{ab}(J_{ab})$
	$\frac{1}{2}\hat{P}(a, bc)\bar{H}_{efi}^{bmc}r_m^{aef}$	

Table I: All diagrams for the 2PA-EOM-CCSD method with both ordinary and reduced amplitudes and matrix elements. The reduced amplitudes and matrix elements are defined in appendix A, while $\chi_i^a(J)$ is defined in appendix C. Note that the two last diagrams are combined into one expression in the spherical formulation and that repeated indices are summed over.

Third, we use the reverse transformations in Eqs. (A11) and (A17) to transform the uncoupled matrix elements of \bar{H}_e^b and r^{ae} to the corresponding reduced matrix elements. This gives us

$$\begin{aligned} (\bar{H}\hat{R})^{ab}(J) &\leftarrow \frac{1}{\hat{J}^2} \sum_M \bar{H}_e^b(j_b)r^{ae}(J) \\ &\times \sum_{m_a m_b} \delta_{j_b, j_e} \delta_{m_b, m_e} C_{m_a m_b M}^{j_a j_b J} C_{m_a m_e M}^{j_a j_e J}, \end{aligned} \quad (55)$$

where δ is the Kronecker delta and results from the application of the Wigner-Eckart theorem to the matrix element of \bar{H} . Orthogonality of the Clebsch-Gordon coefficients

gives

$$\sum_{m_a m_b} \delta_{j_b, j_e} \delta_{m_b, m_e} C_{m_a m_b M}^{j_a j_b J} C_{m_a m_e M}^{j_a j_e J} = 1, \quad (56)$$

and we are left with

$$(\bar{H}\hat{R})^{ab}(J) \leftarrow \bar{H}_e^b(j_b)r^{ae}(J). \quad (57)$$

Note that $\sum_M 1 = 2J + 1$ and that repeated indices are summed over.

Initially, we left out the permutation operator $\hat{P}(a, b)$ that is needed to generate antisymmetric amplitudes. In the uncoupled representation this operator is defined as

$$\hat{P}(ab) = \hat{1} - \hat{P}_{a,b}, \quad (58)$$

where $\hat{1}$ is the identity operator and $\hat{P}_{a,b}$ changes the order of the two indices a and b , but leaves the coupling order unchanged. Let us apply this operator to $(\bar{H}\hat{R})^{ab}(J)$. The result is

$$\hat{P}(a,b)(\bar{H}\hat{R})^{ab}(J) = (\bar{H}\hat{R})^{ab}(J) - \langle ba; j_a j_b; J || (\bar{H}\hat{R})_C || 0 \rangle, \quad (59)$$

where the last matrix element has the wrong coupling order compared to the reduced amplitudes defined in Eq. (49) where

$$(\bar{H}\hat{R})^{ba}(J) = \langle ba; j_b j_a; J || (\bar{H}\hat{R})_C || 0 \rangle. \quad (60)$$

To change the coupling order, we exploit the symmetry properties of the Clebsch-Gordon coefficients and write

$$\begin{aligned} \langle ba; j_a j_b; J || (\bar{H}\hat{R})_C || 0 \rangle &= (-1)^{j_a + j_b - J} \langle ba; j_b j_a; J || (\bar{H}\hat{R})_C || 0 \rangle \\ &= (-1)^{j_a + j_b - J} (\bar{H}\hat{R})^{ba}(J). \end{aligned} \quad (61)$$

As a consequence of this, we define the permutation operator in the spherical representation to also change the coupling order. This results in the following definition

$$\hat{P}(ab) = \hat{1} - (-1)^{j_a + j_b - J} \hat{P}_{a,b}. \quad (62)$$

The total contribution from the first diagram in Table I in the spherical representation is

$$(\bar{H}\hat{R})^{ab}(J) \leftarrow \hat{P}(ab) \bar{H}_e^b(j_b) r^{ae}(J), \quad (63)$$

where $\hat{P}(ab)$ is defined by Eq. (62).

We define the more complicated three-body permutation operators $\hat{P}(ab,c)$ in the same manner, but they must change the coupling order of three angular momentums. The details have been left to appendix B.

IV. RESULTS

A. Model space and interaction

All calculations in this section have been done in a spherical Hartree-Fock basis, based on harmonic oscillator single-particle wave functions. These are identified with the set of quantum numbers $\{nlj\}$ for both protons and neutrons, where n represents the number of nodes, l represents the orbital momentum, and finally j is the total angular momentum of the single-particle wave function.

We will identify the size of the model space by the variable

$$N_{\max} = \max(N), \quad (64)$$

where $N = 2n + l$, so that the number of harmonic oscillator shells is $N_{\max} + 1$. All single-particle states with

$$2n + l \leq N_{\max}$$

are included and no additional restrictions are made on the allowed configurations. Thus, N_{\max} completely determines the computational size and complexity of the calculations.

N_{\max}	Size	Elements	Memory
10	132	145 623 788	1.1 Gb
12	182	587 531 302	4.4 Gb
14	240	1 963 734 704	14.6 Gb
16	306	5 687 352 954	42.4 Gb
18	380	14 715 230 212	109 Gb
20	458	33 622 665 364	250 Gb

Table II: The first column contains the size of the single-particle basis employed for different model spaces labelled by N_{\max} (See text for details). Column two and three list the number of matrix elements for the different model spaces and the memory footprint of the interaction in our implementation. All numbers are based on the coupled representation, also known as the jj -scheme basis.

In Table II we list the size of the single-particle space for different values of N_{\max} in the spherical representation. In addition, the table includes the total number of matrix elements defining the interaction in Eq. (1), as well as the memory footprint in our calculations. Given the memory requirements alone, it is clear that a distributed storage scheme is needed from the beginning.

In addition to the interaction elements, we also need to store the Arnoldi vectors in the diagonalization procedure. Typically 150 iterations are performed, where one vector has to be stored for each iteration. Table III lists the size of a single vector for selected target states in various model spaces. For a double precision calculation, where each element requires 8 bytes of storage, the Arnoldi diagonalization would require ≈ 76 Gb of memory for a calculation of the $J^\pi = 3^+$ state of ${}^6\text{Li}$ with $N_{\max} = 16$. Thus the Arnoldi procedure quickly becomes the largest memory consumer in this method. In general, there is a steep performance penalty in increasing the total angular momentum of the target state, comparable to increasing the size of the model space.

Our interaction is derived from chiral perturbation theory at next-to-next-to-next-to-leading order ($N^3\text{LO}$) using interaction matrix elements of Entem and Machleidt [21]. The matrix elements of this interaction employs a cutoff $\Lambda = 500$ MeV and all partial waves up to relative angular momentum $J_{\text{rel}} = 6$ are included. We do not include relevant three- and four-body interactions defined by the chiral expansion at this order.

State	$N_{\max} = 10$	$N_{\max} = 12$	$N_{\max} = 14$	$N_{\max} = 16$	$N_{\max} = 18$	$N_{\max} = 20$
${}^6\text{He}(0^+)$	516 048	1 323 972	2 981 930	6 088 376	11 513 088	20 176 104
${}^6\text{He}(1^-)$	1 507 930	3 894 028	8 808 688	18 040 354	34 190 482	60 011 982
${}^6\text{He}(2^+)$	2 391 692	6 251 128	14 255 896	29 364 090	55 885 624	98 356 664
${}^6\text{Li}(0^+)$	775 992	1 989 508	4 478 936	9 142 216	17 284 308	30 285 212
${}^6\text{Li}(1^+)$	2 268 746	5 853 534	13 234 004	27 093 632	51 335 514	90 080 136
${}^6\text{Li}(2^+)$	3 595 384	9 391 650	21 409 878	44 088 456	83 893 672	147 629 532
${}^6\text{Li}(3^+)$	4 676 372	12 438 258	28 699 916	59 604 726	114 125 048	201 657 602
${}^{18}\text{O}(0^+)$	1 908 474	5 022 710	11 485 808	23 680 034	45 071 990	79 331 610
${}^{18}\text{O}(1^-)$	5 594 899	14 802 528	33 974 801	70 231 288	133 940 727	236 049 974
${}^{18}\text{O}(2^+)$	8 891 923	23 794 936	55 036 119	114 391 274	219 038 683	387 077 788
${}^{18}\text{O}(2^-)$	8 897 760	23 803 219	55 047 530	114 406 595	219 058 796	387 083 193
${}^{18}\text{O}(3^+)$	11 613 562	31 596 862	73 906 056	154 840 950	298 237 942	529 098 382
${}^{18}\text{O}(3^-)$	11 621 868	31 608 838	73 922 708	154 863 424	298 267 524	529 107 862
${}^{18}\text{O}(4^+)$	13 629 562	37 905 214	89 982 332	190 504 054	369 757 342	659 327 780
${}^{18}\text{F}(0^+)$	2 868 568	7 545 420	17 248 686	35 552 756	67 658 660	119 071 548
${}^{18}\text{F}(1^+)$	8 403 602	22 228 738	51 009 366	105 427 688	201 040 066	354 285 892
${}^{18}\text{F}(2^+)$	13 362 878	35 742 012	82 642 970	171 734 254	328 788 766	580 957 010
${}^{18}\text{F}(3^+)$	17 451 568	47 458 334	110 973 350	232 452 890	447 659 068	794 095 862
${}^{18}\text{F}(4^+)$	20 479 376	56 930 198	135 106 850	285 982 274	554 996 372	989 530 134
${}^{18}\text{F}(5^+)$	22 363 324	63 896 228	154 444 460	331 158 558	648 765 300	1 163 943 530

Table III: Size of the many-body space in the diagonalization procedure in the Arnoldi algorithm for all states calculated in this work. All numbers are based on the coupled representation, also known as the jj -scheme basis.

When we discuss the center-of-mass contamination of the final solution, we will also need a softer interaction where the short range parts are removed via the similarity renormalization group transformation (SRG) [22]. We will use a cutoff $\lambda = 2.0\text{fm}^{-1}$ for this purpose.

B. Center of mass contamination

Recently, Hagen et al. [23] showed that the coupled-cluster wave function separates into an intrinsic part and a Gaussian for the center-of-mass coordinate. This means that we do not have to worry about the center-of-mass contamination of physical states, as the results will converge to a separated solution.

In the EOM-CC approach we make further approximations by truncating the many-body basis before the diagonalization is performed. It is therefore not clear that the final wave functions separates in the same way as the coupled-cluster reference state.

Following the procedure in Hagen et al. [23], we calculated the expectation value of the center-of-mass energy at the proper frequency, for the ground state of ${}^6\text{He}$, the first excited $J^\pi = 1^-$ state in ${}^6\text{He}$ and the first excited $J^\pi = 3^+$ state in ${}^6\text{Li}$. The calculations were performed in a model space defined by $N_{\max} = 14$, with an SRG interaction with a momentum cutoff at $\lambda = 2.0\text{fm}^{-1}$.

Fig. 1 shows the calculated center-of-mass frequency as a function of the oscillator parameter $\hbar\omega$ defining the single-particle basis, while Fig. 2 shows the center-of-

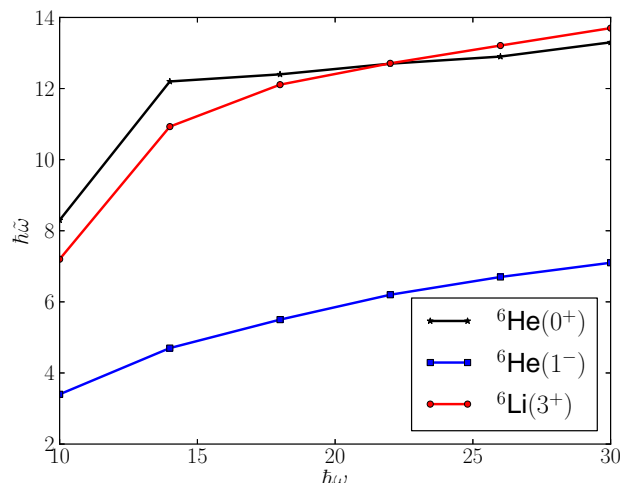


Figure 1: Center-of-mass frequency as calculated by the description in Hagen et al. [23] as a function of the oscillator parameter $\hbar\omega$. Three different states are shown – the $J^\pi = 0^+$ ground state of ${}^6\text{He}$, the $J^\pi = 1^-$ excited state in ${}^6\text{He}$ and the $J^\pi = 3^+$ excited state in ${}^6\text{Li}$.

mass energy at this new frequency.

Immediately, two things are evident. First, the $J^\pi = 1^-$ state in ${}^6\text{He}$ does not separate. The center-of-mass energy is very high and we conclude that this state is unphysical. There are no documented $J^\pi = 1^-$ low-lying states in the ${}^6\text{He}$ spectrum. Second, the ground state of ${}^6\text{He}$ separates, as the center-of-mass energy is

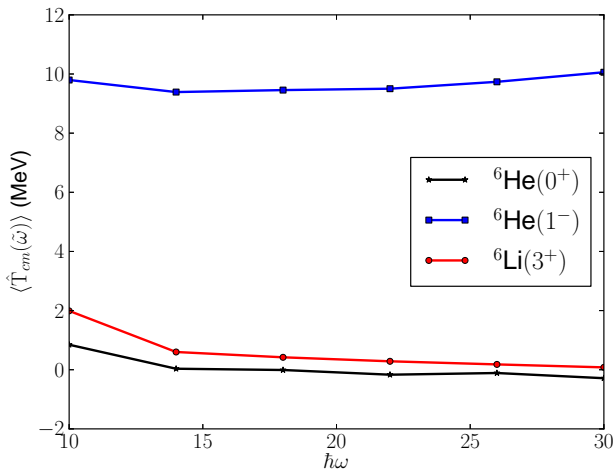


Figure 2: The expectation value of the center-of-mass energy is calculated at the center-of-mass frequency $\hbar\omega$ for the $J^\pi = 0^+$ ground state of ${}^6\text{He}$, the $J^\pi = 1^-$ excited state in ${}^6\text{He}$ and the $J^\pi = 3^+$ excited state in ${}^6\text{Li}$.

approximately zero. At low frequencies, the calculation is not quite converged, yielding a higher center-of-mass admixture in the wave function.

Let us comment further on the $J^\pi = 3^+$ state in ${}^6\text{Li}$. Here, the center-of-mass energy is not quite zero, although very close at approximately 300 keV. This is a physical state, as ${}^6\text{Li}$ has this state low in its spectrum. It must be said that the Hellman-Feynmann theorem used to calculate these values is not exact, so small errors can occur. In addition, the calculation might not be fully converged, but we saw no significant changes between calculations done at $N_{\text{max}} = 12$ and $N_{\text{max}} = 14$. Finally, it can be that the result is not converged with respect to the truncations made in the theory. If this is the case, it might be possible to use the center-of-mass contamination as a measure of convergence. We will touch upon this subject in the next two sections, but a detailed analysis is left to future work.

C. Applications to ${}^6\text{Li}$ and ${}^6\text{He}$

For any given reference nucleus, there are only three nuclei accessible to the 2PA-EOM-CC method. Using ${}^4\text{He}$ as the reference, we can add two protons to calculate properties of ${}^6\text{Be}$, two neutrons for ${}^6\text{He}$ and finally a proton and a neutron to calculate properties of ${}^6\text{Li}$. Of these, only ${}^6\text{Li}$ and ${}^6\text{He}$ are stable with respect to nucleon emission and we will only concentrate our efforts on these. Looking at the structure of ${}^6\text{Li}$ and ${}^6\text{He}$, they are very different. This is an important point, because the quality of the current level of approximation will inevitably depend on the structure of the nucleus.

${}^6\text{Li}$ is well bound and has four bound states below the nucleon emission threshold at 4.433 MeV [24]. The ground state has spin parity assignment $J^\pi = 1^+$, while

the first excited states have $J^\pi = 3^+$, 2^+ and 0^+ . The $J^\pi = 0^+$ ground state in ${}^6\text{He}$ is a two neutron halo state, bound by only 800 keV [24] compared to ${}^4\text{He}$. There are no bound excited states – only a narrow resonance at 1.710 MeV is documented [24].

First we discuss convergence with respect to the size of the model space. Our approach is based on a finite basis expansion, where N_{max} effectively determines the numerical cutoff. We increase the cutoff until the corrections are so small that the uncertainties in our calculation outweighs these differences.

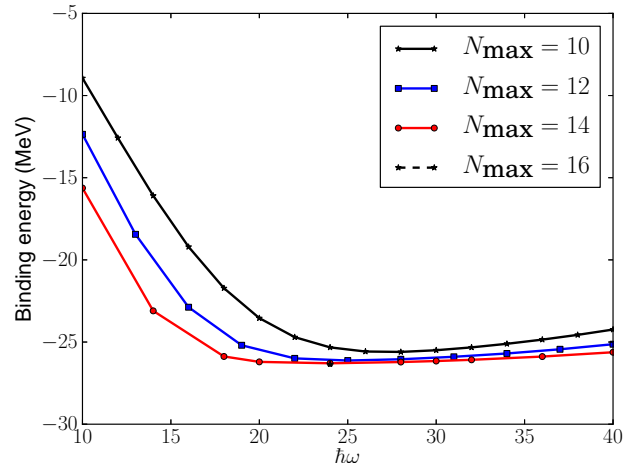


Figure 3: Ground state energy of ${}^6\text{Li}$ as a function of the oscillator parameter $\hbar\omega$ and the size of the model space N_{max} (see text for details).

Fig. 3 shows the calculated total binding energy of ${}^6\text{Li}$, as a function of the oscillator frequency $\hbar\omega$. Different lines correspond to different model spaces. At $N_{\text{max}} = 16$, there is a shallow minimum around $\hbar\omega = 24$ MeV and in a 10 MeV range including this minimum, the binding energy varies by approximately 100 keV. This is less than half a percent of the total energy. At low frequencies, the energy deviates substantially from the minimum, due to the lack of resolution in the single-particle space.

Note that the gain in binding energy when going from $N_{\text{max}} = 14$ to $N_{\text{max}} = 16$ is also very small, about 40 keV. We conclude that the binding energy of ${}^6\text{Li}$ is converged with respect to the size of the model space (N_{max}). The energy at $\hbar\omega = 24$ MeV will be our tabulated result.

The picture is largely identical for the binding energy of ${}^6\text{He}$, only the minimum in energy occurs at $\hbar\omega = 20$ MeV. Here the difference in energy between the two largest model space is about 140 keV.

To show that the excited states follow the same pattern of convergence as the ground state, in Fig. 4 we plot the total energy of the $J^\pi = 3^+$ state in ${}^6\text{Li}$. As before, the energy is plotted as a function of $\hbar\omega$ and different lines correspond to different values of N_{max} . Our estimation of excitation energies will also be taken at specific values of $\hbar\omega$, where we simply take the difference in energy to the ground state at the minimum value. For the calcula-

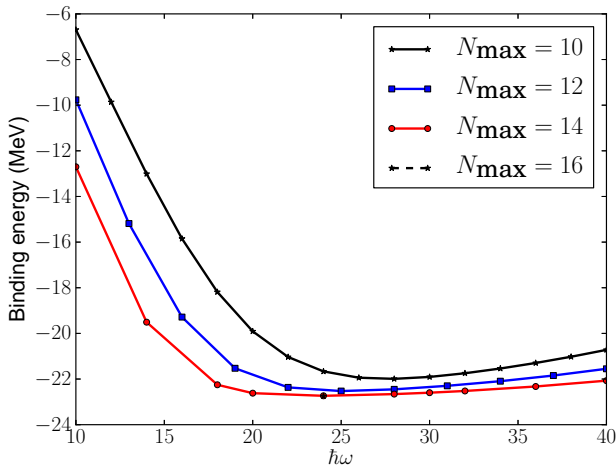


Figure 4: The total energy of the first excited $J^\pi = 3^+$ state of ${}^6\text{Li}$ as a function of the oscillator parameter $\hbar\omega$ and the size of the model space N_{max} (see text for details).

tion of excitation energies in this section, this causes no concern as the minima in energies for all excited states are located at the same $\hbar\omega$ value as the minima for the ground states. (See next section for a discussion of cases where this is not correct.)

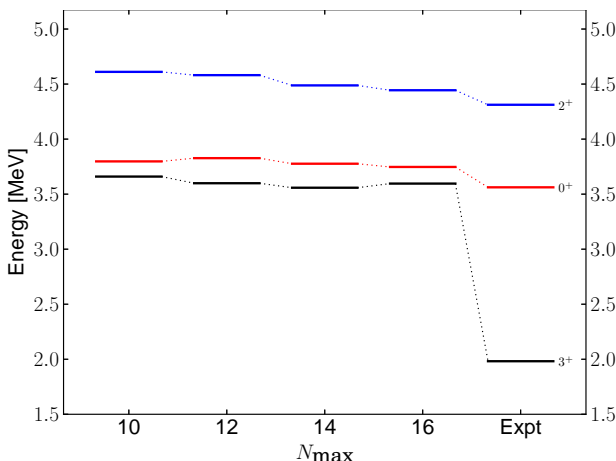


Figure 5: Excitation energy for selected states of ${}^6\text{Li}$, as a function of the size of the model space defined by N_{max} . The rightmost column shows the experimental values from Tilley et al. [24].

In Fig. 5 we show the convergence of the excitation energies for selected states in the spectrum of ${}^6\text{Li}$. The horizontal axis denotes the size of the model space, where the rightmost column are the experimental values [24]. All excitation energies have been calculated at $\hbar\omega = 24$ MeV, which correspond to the minimum of the ground state energy. All three states show very little dependence on the size of the model space at $N_{\text{max}} = 16$. None of the states show any significant center-of-mass contamination, so we conclude that they are converged. We also found an additional $J^\pi = 1^+$ state higher in the spectrum, but this

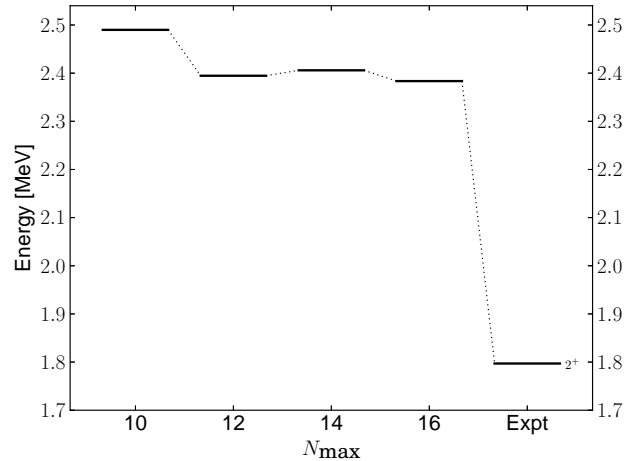


Figure 6: Excitation energy for the first excited $J^\pi = 2^+$ state of ${}^6\text{He}$, as a function of the size of the model space defined by N_{max} . The rightmost column shows the experimental value from Tilley et al. [24].

state had a large center-of-mass admixture in the wave function and is therefore not included.

In Fig. 6 we show an equivalent plot for the first $J^\pi = 2^+$ excited state in ${}^6\text{He}$, which is also converged with respect to the size of the model space. No significant center-of-mass contamination was found neither in this state nor the ground state, but this was not the case for the $J^\pi = 1^-$ state, as already discussed. Note that the scale of the vertical axis of this plot is significantly smaller than that of Fig. 5 and that all excitation energies for ${}^6\text{He}$ were calculated at $\hbar\omega = 20$ MeV.

We also look at some properties of the wave function. Although it is not an observable, other expectation values might be more sensitive to changes in the wave function than the energy. For this purpose we define two properties. First, the partial norms are defined by

$$n(2p0h) = \sum_{ab} (2J+1) (r^{ab}(J))^2 \quad (65)$$

$$n(3p1h) = \sum_{\substack{abci \\ J_{ab}J_{abc}}} (2J_{abc}+1) (r_i^{abc}(J_{ab}, J_{abc}, J))^2, \quad (66)$$

where $n(2p0h) + n(3p1h) = 1$. The amplitudes $r^{ab}(J)$ and $r_i^{abc}(J_{ab}, J_{abc}, J)$ are the spherical amplitudes defined in Eqs. (A16) and (A18), respectively, while J_x are angular momentum labels. Note that the angular momentum factors are included so that the partial norms are consistent between the coupled and uncoupled scheme. These norms quantify the part of the wave function in 2P-0H and 3P-1H configurations, respectively.

Second, we define the total weights

$$w_{pw}^{ab} = (2J+1) \sum_{a,b} \left[(r_{pw}^{ab}(J))^2 + (r_{pw}^{ba}(J))^2 \right], \quad (67)$$

where the label pw identifies the partial wave content of the weight. The sum is over all configurations with this

partial wave content, because the weights of individual configurations are not stable. Only at high frequencies do single configurations dominate. The total weights however, are reasonably stable already at this level.

State	$n(2p0h)$	Dominant configuration(s)	Weight(s)
${}^6\text{Li}(1^+)$	0.77	$(\pi p_{3/2} \nu p_{1/2}), (p_{3/2})^2$	0.40, 0.30
${}^6\text{Li}(3^+)$	0.76	$(p_{3/2})^2$	0.67
${}^6\text{Li}(0^+)$	0.72	$(p_{3/2})^2, (p_{1/2})^2$	0.60, 0.11
${}^6\text{Li}(2^+)$	0.77	$(\pi p_{3/2} \nu p_{1/2})$	0.640
${}^6\text{He}(0^+)$	0.71	$(p_{3/2})^2, (p_{1/2})^2$	0.59, 0.11
${}^6\text{He}(2^+)$	0.74	$(p_{3/2})^2, (p_{3/2} p_{1/2})$	0.47, 0.25
${}^6\text{He}(1^-)$	0.65	$(s_{1/2} p_{3/2}), (d_{5/2} p_{3/2})$	0.32, 0.18

Table IV: This table shows the 2P-0H partial norms (65), as well as the dominant configurations for calculated states in both ${}^6\text{Li}$ and ${}^6\text{He}$. The weights are calculated according to Eq. (67) where all nodes for a given partial wave contribute to the sum. The numbers in parenthesis are the differences of the maximum and minimum values for $\hbar\omega = 20 - 40$ and indicate the level of convergence of the wave function.

We list the partial norms and dominant weights of selected states in ${}^6\text{Li}$ and ${}^6\text{He}$ in Table IV. The ground state of ${}^6\text{Li}$ is dominated by configurations that have a proton in the $p_{3/2}$ orbital and a neutron in the $p_{1/2}$ or the $p_{3/2}$ orbitals. Note that both partial norms and the total weights are more sensitive to changes in the model space than the energy and that the weights are becoming more unstable approaching the nucleon emission threshold. Again the $J^\pi = 1^-$ stands out with a low 2P-0H content. The 2P-0H structure of all the physical states in this table conform with the shell-model picture of two nucleons in the p -shell, but all states have an additional 3P-1H content that cannot be neglected. Additional refinements of our method using also 4P-2H configurations are necessary to analyze this further.

In Table V we show results with estimated numerical uncertainties for the ground and selected excited states of both ${}^6\text{He}$ and ${}^6\text{Li}$. For comparison, both experimental values and results from a no-core shell-model (NCSM) calculation [25] are tabulated where data is available. Note that the results from the NCSM calculation are based on the same interaction as the results from this work, but the interaction is renormalized using the procedure defined in Suzuki and Lee [26], before the diagonalization was performed. In addition, the final results were extrapolated to an infinite model space.

Let us discuss the uncertainties indicated by the parenthesis in the table. For the results from this work, listed in the second column, the numbers in parenthesis simply give the difference in energy between the two largest model spaces. The results from Navrátil and Caurier [25] give the extrapolation errors in the last column, while the experimental energies [24] in the first column are listed without uncertainties.

Fig. 7 shows a graphical representation of the data in Table V. Compared to the results from the NCSM calculation, our results are quite promising. First, the ground state energy of ${}^6\text{Li}$ is well within the uncertain-

${}^6\text{Li}$	Expt.	N ³ LO ($\Lambda = 500\text{MeV}$)	NCSM[25]
$E_{\text{gs}}(1^+)$	-31.993	-28.44(5)	-28.5(5)
$E_{\text{gs}}(1^+)$	0.0	0.0	0.0
$E_x(3^+)$	+2.186	+3.60(4)	+2.91(3)
$E_x(0^+)$	+3.562	+3.76(3)	+3.30(10)
$E_x(2^+)$	+4.312	+4.44(4)	+4.10(15)

${}^6\text{He}$			
$E_{\text{gs}}(0^+)$	-29.270	-25.51(14)	-26.2(5)
$E_{\text{gs}}(0^+)$	0.0	0.0	0.0
$E_x(2^+)$	1.797	2.35(4)	

Table V: Binding energies and excitation energies for selected states of ${}^6\text{Li}$ and ${}^6\text{He}$ with estimated numerical uncertainties. The uncertainties in our results are the differences between the values for the two largest model spaces. The data is compared to NCSM results [25] in the rightmost column, where the parenthesis list extrapolation errors and experimental data in the leftmost column. All experimental data are from Tilley et al. [24].

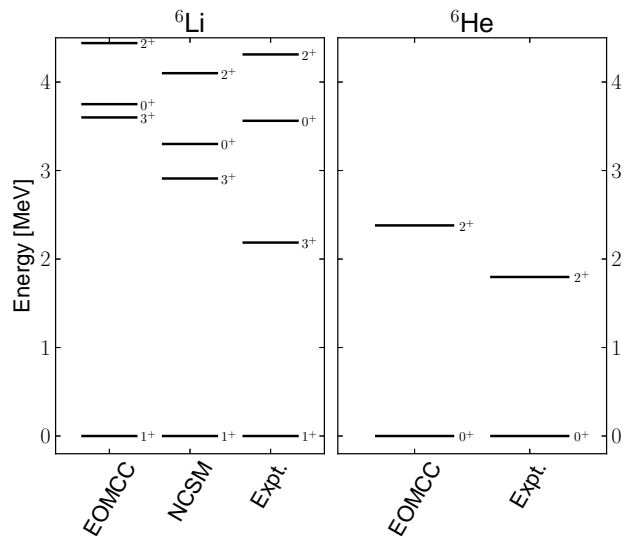


Figure 7: Excitation levels of selected states in ${}^6\text{Li}$ and ${}^6\text{He}$, calculated using 2PA-EOM-CC(this work) and NCSM [25], while compared to experimental [24] values.

ties of the “exact” result, while the ground state energy of ${}^6\text{He}$ is just outside. The difference between the two nuclei can be explained by the extended spatial distribution of ${}^6\text{He}$. Additional correlations are necessary to account for this structure. Although the alpha core in ${}^6\text{He}$ is expected to stay largely unchanged when adding two neutrons, the distribution of these extra neutrons are biased in one direction. This results in a skewed center-of-mass compared to the center-of-mass of the alpha core alone. Additional correlations are necessary to absorb the resulting oscillations of the alpha core with respect to the combined center-of-mass. The spatial distribution of ${}^6\text{Li}$ is tighter, so this effect is not that prominent in

this nucleus. Second, the ordering of excited states in ${}^6\text{Li}$ is reproduced.

We do however, consistently overestimate the excitation energies. While the difference for the first $J^\pi = 0^+$ and 2^+ states are small enough to be attributed to the difference between the calculations, this is not so for the $J^\pi = 3^+$ state. Our results differ by about 700 keV for this state. Neither the partial norms nor the total weights listed in Table IV provide any hint of explanation for this discrepancy. About 76 percent of the wave function is in 2P-0H configurations, which is comparable to the ground state. The wave function is dominated by configurations where both nucleons are in $p_{3/2}$ orbitals, which is consistent with the shell-model picture. Furthermore, the level of convergence for this state is no different from the other excited states. We do however, find a slight center-of-mass admixture in the wave function of the $J^\pi = 3^+$ state, which is not present in the other states. This was illustrated in Fig. 2, where we used a softer renormalized interaction. Now, the calculated center-of-mass contamination is too small to be conclusive, especially since the calculation is only approximate and the analysis has been performed using a softer renormalized interaction. We include it because it might indicate that additional correlations are needed in the calculation, either in the reference or the EOM operator. This matter needs to be investigated further, but currently the implementation will not allow model spaces large enough for a converged description of the center-of-mass admixture in the final wave function.

Using the in-medium similarity renormalization group (IM-SRG), Tsukiyama et al. [27] performed a similar study with a softer interaction. Here, the $J^\pi = 3^+$ state in ${}^6\text{Li}$ is reproduced on the same level of accuracy as the other bound states. We therefore conclude that the discrepancy in our result is due to the approximations done in the 2PA-EOM-CCSD method.

Let us also comment on the differences between our results and the experimental values. First, we see that all excitation energies are overestimated compared to data. Again, the $J^\pi = 3^+$ states is exceptional, but this has been discussed in detail by Navrátil and Caurier [25]. The matter was resolved by the inclusion of three-nucleon forces [28], which also brought the binding energy very close to data.

For the $J^\pi = 2^+$ resonance in ${}^6\text{He}$, this seems not to be the case. We also calculated this state using a chiral interaction with a different cutoff of 600 MeV and found the excitation energy of this state to be largely cutoff independent. This was not so for the excited states in ${}^6\text{Li}$, where especially the $J^\pi = 3^+$ state turned out to be very cutoff dependent. We can better explain the discrepancy in energy of the resonance in ${}^6\text{He}$, by missing continuum degrees of freedom. The current single-particle basis cannot handle the description of both bound, resonance and continuum states necessary in this case. While we are working on the inclusion of the Gamow shell-model [29] in the 2PA-EOM-CC method, as has been done for coupled-

cluster in Hagen et al. [30] a discussion of this is beyond the scope of this article.

Summing up this section, we conclude that for well bound states, with simple structure, the current approximation will yield total energies comparable to exact diagonalization. For weakly bound states, continuum degrees of freedom are necessary for a quantitative comparison to exact results. In addition, we find that we are able to reach sufficiently large model-spaces for our results to be converged for six nucleons, but for certain states, especially the $J^\pi = 3^+$ state in ${}^6\text{Li}$, the effects of 4P-2H configurations need to be investigated.

D. Applications to ${}^{18}\text{O}$ and ${}^{18}\text{F}$

When ${}^{16}\text{O}$ is used as a reference state, the three isobars ${}^{18}\text{O}$, ${}^{18}\text{F}$ and ${}^{18}\text{Ne}$ are reachable by the 2PA-EOM-CCSD method. All have well bound ground states and a rich spectra of bound excited states below their respective nucleon emission thresholds. The spectrum of ${}^{18}\text{F}$ is especially rich, as the exclusion principle does not affect the placement of nucleons in the sd -shell. The proton-neutron interaction is responsible for the compressed spectrum in the fluorine isotope, while strong pairing effects in ${}^{18}\text{O}$ and ${}^{18}\text{Ne}$ result in lower ground state energies. In both ${}^{18}\text{O}$ and ${}^{18}\text{Ne}$ the spectra are opened up and the first excited states are higher in energy. Our current focus is on convergence and the viability of this method. Thus, ${}^{18}\text{Ne}$ is not explicitly discussed, as results are similar to those of ${}^{18}\text{O}$.

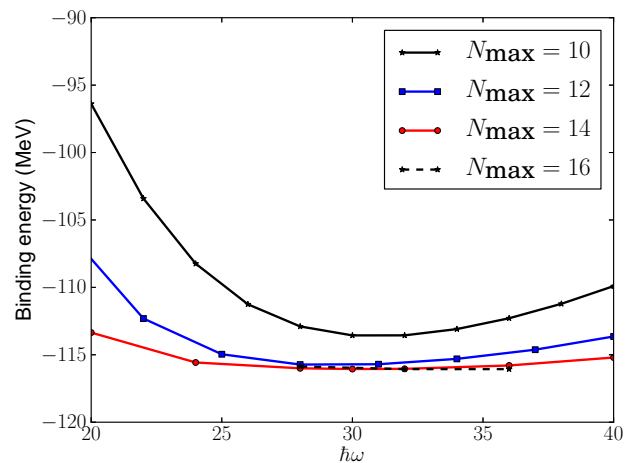


Figure 8: The ground state energy of ${}^{18}\text{O}$ as a function of the oscillator parameter, $\hbar\omega$. Different lines correspond to different model spaces, parametrized by the variable N_{max} (64).

Let us first look at the convergence of the binding energy of ${}^{18}\text{O}$. In Fig. 8, we plot the ground state energy of ${}^{18}\text{O}$ as a function of the oscillator parameter $\hbar\omega$. The different lines correspond to different model spaces, parametrized by the variable N_{max} (64). A shallow minimum develops around $\hbar\omega = 32$ MeV, where the energy is con-

verged with respect to the size of the model space. The difference in energy is about 20 keV when the size of the model space is increased from $N_{\max} = 14$ to $N_{\max} = 16$. We also see that for a wide range of values around the minimum, the ground state energy shows very little dependence on the $\hbar\omega$ parameter. This state is exceptionally well converged and is a testament to the bound nature of this state.

A similar result is obtained for the ground state energy of ^{18}F , where the difference in energy is around 160 keV between the two largest model spaces. This is almost an order of magnitude larger than for the ground state of ^{18}O , but is still well within one percent of the total energy.

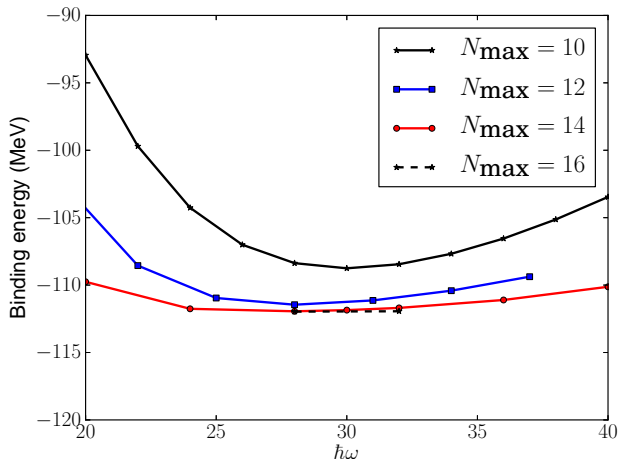


Figure 9: The total energy of the $J^\pi = 3^+$ state in ^{18}O as a function of the oscillator parameter, $\hbar\omega$. Different lines correspond to different model spaces, parametrized by the variable N_{\max} (64).

In Fig. 9 we plot the total energy of the first excited $J^\pi = 3^+$ state in ^{18}O for different model spaces. Here we see a shallow minimum develop at $\hbar\omega = 28$ MeV. Also this state is very well converged, with a difference in energy of only about 25 keV between calculations in the two largest model spaces. We clearly see that the rate of convergence is different for different values of $\hbar\omega$. This will be an issue when we want to calculate excitation energies, as different choices of $\hbar\omega$ lead to different results. To evaluate the excitation energy, we highlight two options. We can treat the total energies as variational results and choose the lowest energy for the ground state and the lowest energy for the $J^\pi = 3^+$ excited state. Thus, at $N_{\max} = 16$ we calculate the excitation energy as

$$E_x(3^+) = E_{3^+}(28\text{MeV}) - E_{0^+}(32\text{MeV}), \quad (68)$$

where $E_{3^+}(28\text{MeV})$ is the total energy of the $J^\pi = 3^+$ excited state, calculated at $\hbar\omega = 28$ MeV, while $E_{0^+}(32\text{MeV})$, is the ground state energy calculated at $\hbar\omega = 32$ MeV.

The second option is to use the same value of $\hbar\omega$ for both energies, where we choose the value where the

ground state has a minimum. Thus, for the current case we calculate the excitation energy as

$$E_x(3^+) = E_{3^+}(32\text{MeV}) - E_{0^+}(32\text{MeV}). \quad (69)$$

The difference in energy between these two options is minimal if sufficiently large model spaces are used, but it will have a significant impact on the rate of convergence.

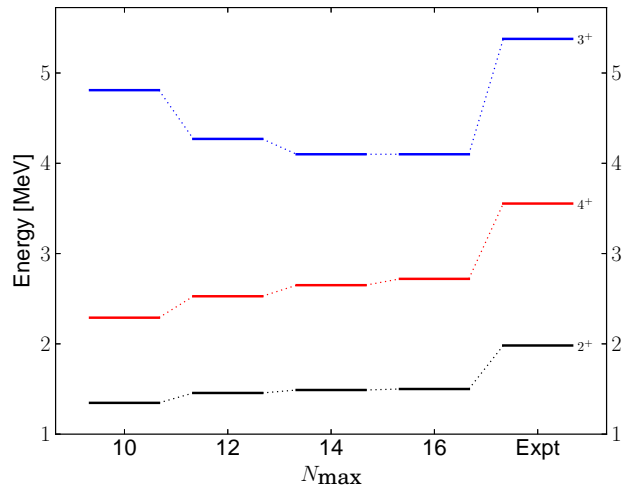


Figure 10: The excitation energies of the first $J^\pi = 2^+$, 3^+ and 4^+ excited states in ^{18}O where the best values for $\hbar\omega$ has been chosen for each state. The different columns represent different model spaces parametrized by the variable N_{\max} (64). The rightmost column contains experimental values from Tilley et al. [31].

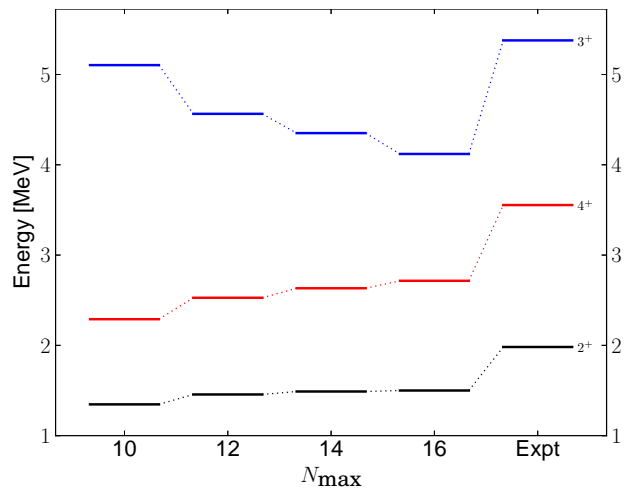


Figure 11: The excitation energies of the first $J^\pi = 2^+$, 3^+ and 4^+ excited states in ^{18}O for $\hbar\omega = 32$ MeV. The different columns represent different model spaces parametrized by the variable N_{\max} (64). The rightmost column contains experimental values from Tilley et al. [31].

The effect is best viewed in Figs. 10 and 11, where we plot the excitation energy of the first $J^\pi = 2^+$, 3^+ and 4^+ excited states in ^{18}O as functions of the size of the model

space. In Fig. 10, the excitation energy is calculated according to Eq. (68), while it is calculated according to Eq. (69) in Fig. 11. For ^{18}O , this choice will only affect the $J^\pi = 3^+$ state, as the other states all have minimum values at $\hbar\omega = 32$ MeV. The effect is significant, but we feel the first approach of Fig. 10 correctly depicts the level of convergence of the excited states. All three states in this plot are very well converged, but the $J^\pi = 4^+$ state displays a slightly larger model space dependence than the other two states.

To further evaluate these states, we look at some of the properties of the wave function. First, we checked that the wave function separates approximately into an intrinsic part and a center-of-mass part, following the recipe outlined in Hagen et al. [23]. None of these states showed any center-of-mass contamination. Second, we looked at the partial norm defined in Eq. (65) and also the relative weights of the different configurations in the final wave function. In Table VI we list these properties for all states calculated in this section.

The $J^\pi = 2^+$ and 4^+ states are dominated by configurations where two neutrons are in the $d_{5/2}$ orbital, but as can be seen in Table VI, the $J^\pi = 2^+$ state shows significant admixture of configurations where one neutron is in the $d_{5/2}$ orbital while the other is in the $s_{1/2}$ orbital. The $J^\pi = 3^+$ state is dominated by the latter configuration. Thus, all three states conform with the shell-model picture of two neutrons in the sd -shell outside an ^{16}O core. They also show the same level of 2P-0H content – around 70 percent.

In contrast, we can look at the three negative parity states that show up in the ^{18}O spectrum. First, from Table VI we see that the 2P-0H content of the wave functions are significantly lower for the negative parity states.

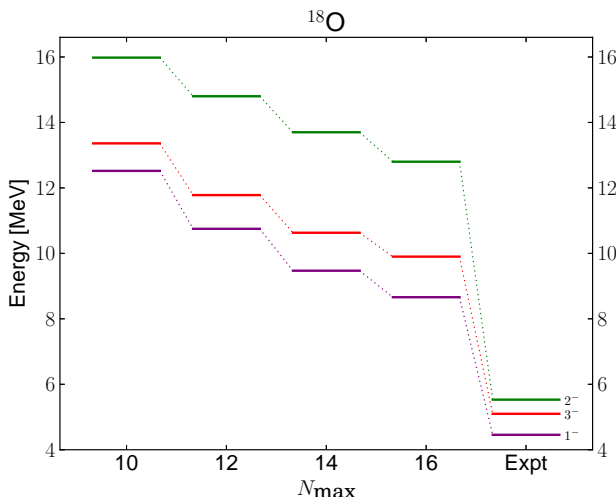


Figure 12: The excitation energies of the first $J^\pi = 1^-, 2^-$ and 3^- excited states in ^{18}O for $\hbar\omega = 32$ MeV. The different columns represents different model spaces parametrized by the variable N_{max} (64). The rightmost column contains experimental values from Tilley et al. [31].

Second, Fig. 12 shows that the excitation energies of these states are not converged at $N_{\text{max}} = 16$, and far from experimental data. Finally, the center-of-mass contamination of all three states is rather large and similar to the $J^\pi = 1^-$ state in ^6He (see Fig. 2). We must therefore conclude that the current truncation is not sufficient to reproduce these states. It will be necessary to include 4P-2H correlations to get the negative parity states right. We can understand this by examining how negative parity states can be produced in ^{18}O . First, it can be produced by placing one neutron in the sd -shell, while the other is placed in the pf -shell. If this was the dominant configuration, the current truncation would have been enough. Secondly, it can also be produced by placing two neutrons in the sd -shell and excite nucleons from the p -shell up to the sd -shell. If this excitation is comparable in energy to the first configuration, 3P-1H configurations start to dominate and 4P-2H configurations are probably necessary.

As a side note, we also see that the wave function of these negative parity states are spread over a large number of configurations with significant contributions from higher partial waves.

In the spectrum of ^{18}O , there are three bound $J^\pi = 0^+$ and 2^+ states. The second $J^\pi = 0^+$ state is especially interesting for this method, as it is a 4P-2H state [32]. In the shell-model language, it is an intruder state, because configurations outside the sd -shell are important to get this state right. As the current implementation only includes 3P-1H configuration, this state can provide clues as to what behaviour we can expect from states that are not converged with respect to the level of approximation.

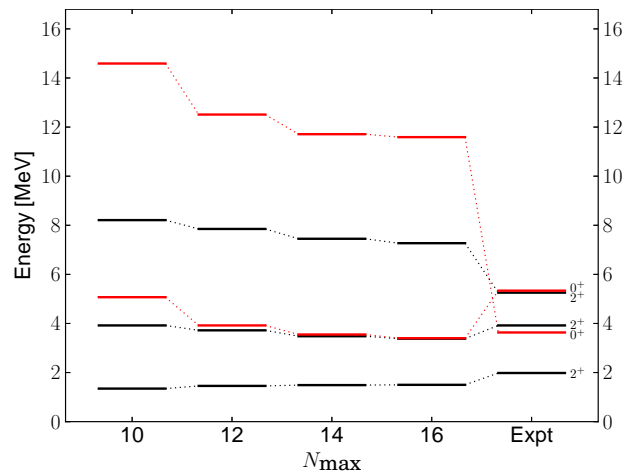


Figure 13: The excitation energies of the first few $J^\pi = 0^+$ and 2^+ states in ^{18}O for $\hbar\omega = 32$ MeV. The different columns represents different model spaces parametrized by the variable N_{max} (64). The rightmost column contains experimental values from Tilley et al. [31].

In Table VI we list three $J^\pi = 0^+$ states in ^{18}O and none of them stands out. They all have similar partial norms of around 70 percent and are dominated by two

State	$n(2p0h)$	Dominant configuration(s)	Weight(s)
$^{18}\text{O}(0_1^+)$	0.69	$(d_{5/2})^2, (s_{1/2})^2$	0.52, 0.12
$^{18}\text{O}(0_2^+)$	0.69	$(s_{1/2})^2$	0.62
$^{18}\text{O}(0_3^+)$	0.70	$(d_{3/2})^2$	0.62
$^{18}\text{O}(2_1^+)$	0.70	$(d_{5/2})^2, (s_{1/2}d_{5/2})$	0.37, 0.27
$^{18}\text{O}(2_2^+)$	0.71	$(s_{1/2}d_{5/2}), (d_{5/2})^2$	0.44, 0.26
$^{18}\text{O}(2_3^+)$	0.70	$(d_{5/2})d_{3/2}, (s_{1/2}d_{3/2})$	0.49, 0.17
$^{18}\text{O}(3_1^+)$	0.71	$(s_{1/2}d_{5/2})$	0.71
$^{18}\text{O}(4_1^+)$	0.71	$(d_{5/2})^2$	0.64
$^{18}\text{O}(1_1^-)$	0.62	$(p_{3/2}d_{5/2}), (p_{3/2}s_{1/2}), (d_{5/2}f_{7/2})$	0.22, 0.17, 0.12
$^{18}\text{O}(2_1^-)$	0.65	$(p_{3/2}d_{5/2})$	0.49
$^{18}\text{O}(3_1^-)$	0.62	$(p_{3/2}d_{5/2}), (p_{1/2}d_{5/2}), (s_{1/2}f_{7/2}), (d_{5/2}f_{7/2})$	0.19, 0.12, 0.11, 0.10
$^{18}\text{F}(0_1^+)$	0.69	$(d_{5/2})^2$	0.51
$^{18}\text{F}(1_1^+)$	0.73	$(d_{5/2}d_{3/2}), (d_{5/2})^2, (s_{1/2})^2$	0.28, 0.22, 0.16
$^{18}\text{F}(2_1^+)$	0.72	$(s_{1/2}d_{5/2}), (d_{5/2}d_{3/2}), (s_{1/2}d_{3/2})$	0.34, 0.20, 0.14
$^{18}\text{F}(3_1^+)$	0.71	$(s_{1/2}d_{5/2}), (d_{5/2})^2$	0.47, 0.18
$^{18}\text{F}(4_1^+)$	0.72	$(d_{5/2})^2$	0.64
$^{18}\text{F}(5_1^+)$	0.72	$(d_{5/2})^2$	0.70

Table VI: This table shows the 2P-0H partial norms(65), as well as the dominant configurations for calculated states in both ^{18}O and ^{18}F . The weights are calculated according to Eq. (67) where all nodes for a given partial wave contribute to the sum.

neutrons in $d_{5/2}$, $s_{1/2}$ and $d_{3/2}$ respectively. In Fig. 13 we show the convergence patterns for these states, along with those of the three $J^\pi = 2^+$ states. All states show similar level of convergence and it is not possible to single out one of the states. However, if we look at the center-of-mass contamination of these states, the third $J^\pi = 0^+$ shows massive contamination, while the other two show almost none. We therefore chose to associate our $J^\pi = 0^+$ state at 11.6 MeV, with the experimentally observed $J^\pi = 0^+$ state at 3.63 MeV. Our $J^\pi = 0^+$ state at 3.4 MeV is closer in energy, but including effects of three-nucleon forces, pushes this state higher in energy and very close to the experimentally observed $J^\pi = 0^+$ state at 5.34 MeV. [5]. A similar effect occurs among the $J^\pi = 2^+$ excited states, but it is less prominent. Here, the center-of-mass contamination were negligible for all three states.

Let us summarize our discussion of missing many-body correlations. We have identified four different markers to indicate missing physics. Unfortunately, none of them can be used quantitatively and all must be evaluated simultaneously to form a general picture. First, the partial norm can be used to differentiate between different states. From these calculations it seems that a 2P-0H norm of around 70 percent is the standard. A lower partial norm, might indicate the need for 4P-2H correlations. Second, we look at the total weights in the different configurations. If the weights are spread over many different configurations, as they were in the wave functions of the negative parity states calculated in ^{18}O , this might also indicate missing 4P-2H configurations. Third, we look at the convergence patterns and if energies converge

slowly, this probably means that something is missing from the calculation. In weakly bound states for example, continuum effects result in the need for additional resolution in the single-particle basis. Finally, we look at the level of center-of-mass contamination present in the wave function. None of these arguments can be analyzed in detail, before 4P-2H configurations are included. We are working on this, but computationally, it will only be possible to include these configurations in a small single-particle space. If the 3P-1H and 4P-2H configurations are defined only in a so-called active space around the Fermi level, the computational cost might be manageable. This has been done successfully in Gour et al. [33] and should prove to be a valuable approximation also in this method. The formation of a correlated alpha cluster around the Fermi level is important in this mass region and can hopefully be accounted for using a minimal set of 4P-2H configurations.

Let us also look at the convergence of selected states in ^{18}F . In Fig. 14 we show the excitation energy of the first few states in ^{18}F for different model spaces. Here all states are relative well converged, with only the $J^\pi = 4^+$ state showing some model space dependence at $N_{\text{max}} = 16$. None of these states have significant center-of-mass contamination and all partial norms are on the same level as can be seen in Table VI. This table also shows that the dominant weights are spread over several different configurations, but all within the sd -shell. According to our earlier discussion, we can find no fault with these states.

In Fig. 15, we plot selected states from the excitation spectra of ^{18}O , ^{18}F and ^{18}Ne . Only states that are con-

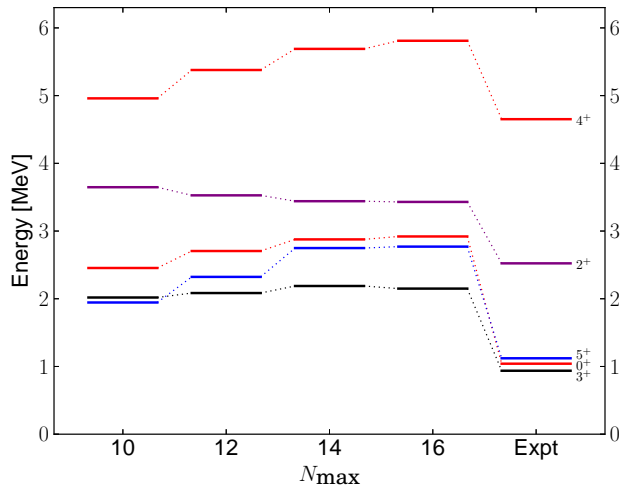


Figure 14: The excitation energies of the first $J^\pi = 0^+, 2^+, 3^+, 4^+$ and 5^+ states in ^{18}F , calculated at $\hbar\omega = 30$ MeV. The different columns represents different model spaces parametrized by the variable N_{max} (64). The rightmost column contains experimental values from Tilley et al. [31].

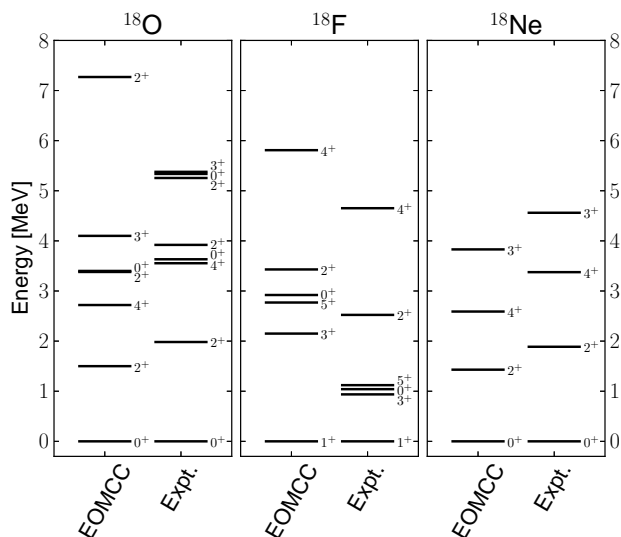


Figure 15: Excitation energies for selected states in ^{18}O , ^{18}F and ^{18}Ne compared to experimental values from Tilley et al. [31].

sidered good are plotted and compared to their experimental values.

Table VII lists the numerical values, used in Fig. 15 together with the ground state energies for future comparison. The difference in energy between calculations in the two largest model spaces, is listed as the uncertainty of our results in this table. The experimental values are from Tilley et al. [31]

It is clear that the spectrum in ^{18}O and ^{18}Ne is compressed compared to data, while for ^{18}F , the spectra is more open. This is consistent with other calculations using different interactions [34–37], where the ^{18}F spectra

^{18}O	Expt.	N^3LO ($\Lambda = 500\text{MeV}$)
$E_{\text{gs}}(0^+)$	−139.807	−130.00(2)
$E_{\text{gs}}(0_1^+)$	0.0	0.0
$E_x(2_1^+)$	+1.982	+1.50(1)
$E_x(4_1^+)$	+3.554	+2.72(7)
$E_x(0_2^+)$	+3.633	NA
$E_x(2_2^+)$	+3.92	+3.38(2)
$E_x(2_3^+)$	+5.255	+7.27(18)
$E_x(0_3^+)$	+5.336	+3.40(15)
$E_x(3_1^+)$	+5.3778	+4.12(1)
^{18}F		
$E_{\text{gs}}(1^+)$	−137.370	−129.75(16)
$E_{\text{gs}}(1^+)$	0.0	0.0
$E_x(3^+)$	+0.937	+2.15(4)
$E_x(0^+)$	+1.041	+2.92(4)
$E_x(5^+)$	+1.121	+2.77(2)
$E_x(2^+)$	+2.523	+3.43(1)
$E_x(4^+)$	+4.652	+5.81(12)
^{18}Ne		
$E_{\text{gs}}(0^+)$	−132.143	−122.56(15)
$E_{\text{gs}}(0^+)$	0.0	0.0
$E_x(2^+)$	+1.887	+1.43(3)
$E_x(4^+)$	+3.376	+2.59(6)
$E_x(3^+)$	+4.561	+3.83(4)

Table VII: Ground and excited state energies for the $A = 18$ system, compared to experimental data. The experimental energies are from Tilley et al. [31]. The number in parenthesis indicates the level of convergence and is the difference in energy between calculations in the two largest model spaces.

is much more open compared to experiment than that of ^{18}O . The level ordering is largely reproduced, except for the cases already discussed. A more detailed comparison to experimental data in this region, is difficult to perform before both three-nucleon forces and continuum degrees of freedom are included [5, 38–40].

V. CONCLUSIONS AND OUTLOOK

We have presented the spherical version of the 2PA-EOM-CCSD method, appropriate for the calculation of energy eigenstates in nuclei that can be described as two particles attached to a closed (sub-)shell reference. The method has been evaluated in both $A = 6$ and $A = 18$ nuclei, where the results were mostly converged with respect to the single-particle basis.

In comparison with a full diagonalization, both ground state and excited state energies were in general very accurate. However, a singular excited state in ^6Li deviated significantly from the “exact” result, showing the need to include additional correlations like 4P-2H configurations for the accurate treatment of complex states. For simple states, where a 2P structure is dominant, the current

level of truncation is adequate.

In comparison with experiment, both three-nucleon

forces and a correct treatment of the scattering continuum are needed to refine our results.

-
- [1] W. Leidemann and G. Orlandini (2012), submitted to Progress in Particle and Nucl. Phys., nucl-th/1204.4617v1, URL <http://arxiv.org/abs/1204.4617v1>.
 - [2] P. Navrátil, S. Quaglioni, I. Stetcu, and B. R. Barrett, J. Phys. G **36**, 083101 (2009), URL <http://stacks.iop.org/0954-3899/36/i=8/a=083101>.
 - [3] R. J. Bartlett and M. Musiał, Rev. Mod. Phys. **79**, 291 (2007), URL <http://link.aps.org/doi/10.1103/RevModPhys.79.291>.
 - [4] I. Shavitt and R. J. Bartlett, *Many-body methods in Chemistry and Physics* (Cambridge University Press, Cambridge, 2009).
 - [5] G. Hagen, M. Hjorth-Jensen, G. R. Jansen, R. Machleidt, and T. Papenbrock (2012), accepted for publication in Phys. Rev. Lett., nucl-th/1202.2839v1.
 - [6] G. Hagen, M. Hjorth-Jensen, G. R. Jansen, R. Machleidt, and T. Papenbrock (2012), submitted to PRL, nucl-th/1204.3612v1.
 - [7] G. R. Jansen, M. Hjorth-Jensen, G. Hagen, and T. Papenbrock, Phys. Rev. C **83**, 054306 (2011), URL <http://link.aps.org/doi/10.1103/PhysRevC.83.054306>.
 - [8] G. Hagen, T. Papenbrock, D. J. Dean, and M. Hjorth-Jensen, Phys. Rev. Lett. **101**, 092502 (2008).
 - [9] G. Hagen, D. J. Dean, M. Hjorth-Jensen, T. Papenbrock, and A. Schwenk, Phys. Rev. C **76**, 044305 (2007).
 - [10] S. A. Kucharski and R. J. Bartlett, The Journal of Chemical Physics **108**, 5243 (1998), URL <http://link.aip.org/link/?JCP/108/5243/1>.
 - [11] A. G. Taube and R. J. Bartlett, J. Chem. Phys. **128**, 044110 (2008), URL <http://link.aip.org/link/?JCP/128/044110/1>.
 - [12] G. Hagen, T. Papenbrock, D. J. Dean, and M. Hjorth-Jensen, Phys. Rev. C **82**, 034330 (2010).
 - [13] G. H. Golub and C. F. Van Loan, *Matrix Computations* (Johns Hopkins University Press, Baltimore, 1996).
 - [14] J. F. Stanton and R. J. Bartlett, J. Chem. Phys. **98**, 7029 (1993).
 - [15] D. C. Comeau and R. J. Bartlett, Chem. Phys. Letters **207**, 414 (1993).
 - [16] M. Musiał and R. J. Bartlett, J. Chem. Phys. **119**, 1901 (2003).
 - [17] M. Musiał, S. A. Kucharski, and R. J. Bartlett, J. Chem. Phys. **118**, 1128 (2003).
 - [18] G. Hagen, T. Papenbrock, and M. Hjorth-Jensen, Phys. Rev. Lett. **104**, 182501 (2010), URL <http://link.aps.org/doi/10.1103/PhysRevLett.104.182501>.
 - [19] A. Bohr and B. R. Mottelson, *Nuclear structure* (Benjamin, New York, 1969).
 - [20] R. Edmunds, A., *Angular momentum in quantum mechanics* (Princeton university press, Princeton, New Jersey, 1960), 2nd ed.
 - [21] D. R. Entem and R. Machleidt, Phys. Rev. C **68**, 041001 (2003), URL <http://link.aps.org/doi/10.1103/PhysRevC.68.041001>.
 - [22] S. K. Bogner, R. J. Furnstahl, and R. J. Perry, Phys. Rev. C **75**, 061001 (2007), URL <http://link.aps.org/doi/10.1103/PhysRevC.75.061001>.
 - [23] G. Hagen, T. Papenbrock, and D. J. Dean, Phys. Rev. Lett. **103**, 062503 (2009), URL <http://link.aps.org/doi/10.1103/PhysRevLett.103.062503>.
 - [24] D. Tilley, C. Cheves, J. Godwin, G. Hale, H. Hofmann, J. Kelley, C. Sheu, and H. Weller, Nucl. Phys. A **708**, 3 (2002), ISSN 0375-9474, URL <http://www.sciencedirect.com/science/article/pii/S0375947402005973>.
 - [25] P. Navrátil and E. Caurier, Phys. Rev. C **69**, 014311 (2004), URL <http://link.aps.org/doi/10.1103/PhysRevC.69.014311>.
 - [26] K. Suzuki and S. Y. Lee, Prog. Theor. Phys. **64**, 2091 (1980), URL <http://ptp.ipap.jp/link?PTP/64/2091/>.
 - [27] K. Tsukiyama, S. K. Bogner, and A. Schwenk (2012), nucl-th/1203.2515.
 - [28] P. Navrátil, V. G. Gueorguiev, J. P. Vary, W. E. Ormand, and A. Nogga, Phys. Rev. Lett. **99**, 042501 (2007), URL <http://link.aps.org/doi/10.1103/PhysRevLett.99.042501>.
 - [29] N. Michel, W. Nazarewicz, and M. Płoszajczak, Phys. Rev. C **70**, 064313 (2004), URL <http://link.aps.org/doi/10.1103/PhysRevC.70.064313>.
 - [30] G. Hagen, D. J. Dean, M. Hjorth-Jensen, and T. Papenbrock, Phys. Lett. B **656**, 169 (2007).
 - [31] D. Tilley, H. Weller, C. Cheves, and R. Chasteler, Nucl. Phys. A **595**, 1 (1995), ISSN 0375-9474, URL <http://www.sciencedirect.com/science/article/pii/S0375947495003381>.
 - [32] P. Ellis and T. Engeland, Nucl. Phys. A **144**, 161 (1970), ISSN 0375-9474, URL <http://www.sciencedirect.com/science/article/pii/S0375947470904999>.
 - [33] J. R. Gour, P. Piecuch, and M. Włoch, J. Chem. Phys. **123**, 134113 (2005).
 - [34] M. F. Jiang, R. Machleidt, D. B. Stout, and T. T. S. Kuo, Phys. Rev. C **46**, 910 (1992), URL <http://link.aps.org/doi/10.1103/PhysRevC.46.910>.
 - [35] X.-W. Pan, T. Kuo, M. Vallières, D. H. Feng, and A. Novoselsky, Phys. Rep. **264**, 311 (1996), ISSN 0370-1573, URL <http://www.sciencedirect.com/science/article/pii/S0370157395000453>.
 - [36] J. D. Holt, J. W. Holt, T. T. S. Kuo, G. E. Brown, and S. K. Bogner, Phys. Rev. C **72**, 041304 (2005), URL <http://link.aps.org/doi/10.1103/PhysRevC.72.041304>.
 - [37] H. Dong, T. T. S. Kuo, and J. W. Holt (2011), to be submitted, nucl-th/1105.4169v1, URL <http://arxiv.org/abs/1105.4169v1>.
 - [38] A. Volya and V. Zelevinsky, Phys. Rev. Lett. **94**, 052501 (2005), URL <http://link.aps.org/doi/10.1103/PhysRevLett.94.052501>.
 - [39] G. Hagen, T. Papenbrock, D. J. Dean, M. Hjorth-Jensen, and B. V. Asokan, Phys. Rev. C **80**, 021306 (2009).
 - [40] T. Otsuka, T. Suzuki, J. D. Holt, A. Schwenk, and Y. Akaishi, Phys. Rev. Lett. **105**, 032501 (2010), URL <http://link.aps.org/doi/10.1103/PhysRevLett.105.032501>.

Appendix A: REDUCED MATRIX ELEMENTS

The reduced matrix elements of a spherical tensor operator \hat{T}_M^J of rank J and projection M , are defined according to the Wigner-Eckart theorem,

$$\langle \alpha; J_\alpha M_\alpha | \hat{T}_M^J | \beta; J_\beta M_\beta \rangle = C_{MM_\beta M_\alpha}^{JJ_\beta J_\alpha} \langle \alpha; J_\alpha || \hat{T}^J || \beta; J_\beta \rangle. \quad (A1)$$

Here, α and β are general labels representing all quantum numbers except angular momentum and its projection, while $J_\alpha(M_\alpha)$ and $J_\beta(M_\beta)$ are the total angular momentum(projection) of the bra and ket state respectively. The double bars denote reduced matrix elements and does not depend on any of the angular momentum projections and $C_{MM_\beta M_\alpha}^{JJ_\beta J_\alpha}$ is a Clebsch-Gordon coefficient.

In coupled-cluster, the unknown amplitudes are the matrix elements of the cluster operator \hat{T}_0^0

$$\begin{aligned} t_i^a &= \langle a; j_a m_a | \hat{T}_0^0 | i; j_i m_i \rangle \\ t_{ij}^{ab} &= \langle ab; j_a m_a j_b m_b | \hat{T}_0^0 | ij; j_i m_i j_j m_j \rangle \\ &\vdots \end{aligned}$$

where the operator sub- and superscript identifies the cluster operator as a scalar under rotation. Also, the labels $abij \dots$, denote single-particle states and we have singled out the angular momentum(projection) in the labels $j_a(m_a)$ etc.

Now, the reduced matrix elements of the cluster operator are defined according to Eq. (A1). For example,

$$\begin{aligned} \langle ab; j_a m_a j_b m_b | \hat{T}_0^0 | ij; j_i m_i j_j m_j \rangle = \\ \sum_{\substack{J_{ab} M_{ab} \\ J_{ij} M_{ij}}} C_{m_a m_b M_{ab}}^{j_a j_b J_{ab}} C_{m_i m_j M_{ij}}^{j_i j_j J_{ij}} C_{0 M_{ij} M_{ab}}^{0 J_{ij} J_{ab}} \\ \times \langle ab; j_a j_b; J_{ab} || \hat{T}^0 || ij; j_i j_j; J_{ij} \rangle, \end{aligned}$$

where the sum and the first two Clebsch-Gordon coefficients come from the coupling of j_a and j_b to J_{ab} and of j_i and j_j to J_{ij} , in that specific order. This expression is simplified by the explicit evaluation of the third Clebsch-Gordon coefficient

$$C_{0 M_{ij} M_{ab}}^{0 J_{ij} J_{ab}} = \delta_{J_{ab}, J_{ij}=J} \delta_{M_{ab}, M_{ij}=M},$$

where $\delta_{\alpha, \beta}$ is the Kronecker delta. We get

$$\begin{aligned} \langle ab; j_a m_a j_b m_b | \hat{T}_0^0 | ij; j_i m_i j_j m_j \rangle = \\ \sum_{JM} C_{m_a m_b M}^{j_a j_b J} C_{m_i m_j M}^{j_i j_j J} \langle ab; j_a j_b; J || \hat{T}^0 || ij; j_i j_j; J \rangle. \end{aligned}$$

When this specific coupling order is used(left to right) and no confusion will arise, we will use a shorthand notation for the reduced matrix elements, defined by

$$t_i^a(J) = \langle a; J || \hat{T}^0 || i; J \rangle \quad (A2)$$

$$t_{ij}^{ab}(J) = \langle ab; j_a j_b; J || \hat{T}^0 || ij; j_i j_j; J \rangle. \quad (A3)$$

The transformations between the reduced amplitudes and the original amplitudes of the cluster operator are defined as

$$t_i^a(J) = \delta_{j_a, j_i=J} t_i^a \quad (A4)$$

$$t_i^a = \delta_{j_a, j_i=J} t_i^a(J) \quad (A5)$$

$$t_{ij}^{ab}(J) = \frac{1}{J^2} \sum_{\substack{m_a m_b M \\ m_i m_j M}} C_{m_a m_b M}^{j_a j_b J} C_{m_i m_j M}^{j_i j_j J} t_{ij}^{ab} \quad (A6)$$

$$t_{ij}^{ab} = \sum_{JM} C_{m_a m_b M}^{j_a j_b J} C_{m_i m_j M}^{j_i j_j J} t_{ij}^{ab}(J), \quad (A7)$$

where we use the convention $\hat{J} = \sqrt{2J+1}$.

As the similarity-transformed Hamiltonian(\bar{H}) is a scalar under rotation as well, the shorthand form of its reduced matrix elements are defined analogously

$$\bar{H}_q^p(J) = \langle p; J || \bar{H}^0 || q; J \rangle \quad (A8)$$

$$\bar{H}_{rs}^{pq}(J) = \langle pq; j_p j_q; J || \bar{H}^0 || rs; j_r j_s; J \rangle. \quad (A9)$$

The transformations between the original and reduced matrix elements are given by

$$\bar{H}_q^p(J) = \delta_{j_p, j_q=J} \bar{H}_q^p \quad (A10)$$

$$\bar{H}_q^p = \delta_{j_p, j_q=J} \bar{H}_q^p(J) \quad (A11)$$

$$\bar{H}_{rs}^{pq}(J) = \frac{1}{J^2} \sum_{\substack{m_p m_q M \\ m_r m_s M}} C_{m_p m_q M}^{s_p s_q J} C_{m_r m_s M}^{r_s r_s J} \bar{H}_{rs}^{pq} \quad (A12)$$

$$\bar{H}_{rs}^{pq} = \sum_{JM} C_{m_p m_q M}^{s_p s_q J} C_{m_r m_s M}^{r_s r_s J} \bar{H}_{rs}^{pq}(J). \quad (A13)$$

The original matrix elements of the similarity-transformed Hamiltonian are defined in Jansen et al. [7].

The r -amplitudes are the matrix elements of the excitation operator in Eq. (46)

$$r^{ab} = \langle ab; j_a m_a j_b m_b | \hat{R}_M^J | 0 \rangle$$

$$r_i^{abc} = \langle abc; j_a m_a j_b m_b j_c m_c | \hat{R}_M^J | i; j_i m_i \rangle,$$

where the operator is now a general tensor operator of rank J and projection M . The bra side contains up to three indices and we have to couple three angular momentum vectors to be able to define the reduced amplitudes. Using r_i^{abc} as an example, we couple from left to right and get

$$\begin{aligned} \langle abc; j_a m_a j_b m_b j_c m_c | \hat{R}_M^J | i; j_i m_i \rangle = \\ \sum_{\substack{J_{ab} M_{ab} \\ J_{abc} M_{abc}}} C_{m_a m_b M_{ab}}^{j_a j_b J_{ab}} C_{M_{ab} m_c M_{abc}}^{J_{ab} j_c J_{abc}} C_{M m_i M_{abc}}^{J J_{ab} J_{abc}} \\ \langle abc; j_a j_b; J_{ab} j_c; J_{abc} || \hat{R}^J || i; j_i \rangle, \end{aligned}$$

where the last Clebsch-Gordon coefficient is due to the Wigner-Eckart theorem. We let the order of the angular momentum labels on the bra-side specify the coupling order, where j_a and j_b couples to J_{ab} . In turn, J_{ab} and j_c

couples to J_{abc} . When this coupling order has been used and no confusion will arise, we will use the shorthand notation for the reduced elements, defined by

$$r^{ab}(J) = \langle ab; j_a j_b; J | \hat{R}^J | 0 \rangle \quad (\text{A14})$$

$$r_i^{abc}(J, J_{abc}, J_{ab}) = \langle abc; j_a j_b; J_{ab} j_c; J_{abc} | \hat{R}^J | i; j_i \rangle. \quad (\text{A15})$$

In the shorthand notation, the transformations between the reduced and the original amplitudes is

$$r^{ab}(J) = \frac{1}{\hat{j}_2^2} \sum_{M m_a m_b} r^{ab} C_{m_a m_b M}^{j_a j_b J} \quad (\text{A16})$$

$$r^{ab} = C_{m_a m_b M}^{j_a j_b J} r^{ab}(J) \quad (\text{A17})$$

$$\begin{aligned} r_i^{abc}(J, J_{abc}, J_{ab}) &= \frac{1}{\hat{j}_{abc}^2} \sum_{\substack{M M_{abc} M_{ab} \\ m_a m_b m_c m_i}} r_i^{abc} C_{m_a m_b M_{ab}}^{j_a j_b J_{ab}} \\ &\quad \times C_{M_{ab} m_c M_{abc}}^{J_{ab} j_c J_{abc}} C_{M m_i M_{abc}}^{J j_i J_{abc}}. \end{aligned} \quad (\text{A18})$$

$$\begin{aligned} r_i^{abc} &= \sum_{\substack{J_{abc} M_{abc} \\ J_{ab} M_{ab}}} r_i^{abc}(J, J_{abc}, J_{ab}) \\ &\quad \times C_{m_a m_b M_{ab}}^{j_a j_b J_{ab}} C_{M_{ab} m_c M_{abc}}^{J_{ab} j_c J_{abc}} C_{M m_i M_{abc}}^{J j_i J_{abc}}. \end{aligned} \quad (\text{A19})$$

Appendix B: PERMUTATION OPERATORS

The diagrams in Table I contain permutation operators that guarantees an antisymmetric final wave function. In the uncoupled formalism, these were simple and defined by

$$\hat{P}(ab) = \hat{1} - \hat{P}_{a,b} \quad (\text{B1})$$

$$\hat{P}(ab, c) = \hat{1} - \hat{P}_{a,c} - \hat{P}_{b,c}, \quad (\text{B2})$$

where $\hat{P}_{a,b}$ permutes indices a and b and $\hat{1}$ is the identity operator. In the spherical formalism, this simple form is not adequate, as a specific coupling order is used in all reduced amplitudes. To see why, let us apply $\hat{P}_{a,b}$ to a reduced amplitude $r^{ab}(J)$

$$\hat{P}_{a,b} \langle ab; j_a j_b; J | \hat{R}^J | 0 \rangle = \langle ba; j_a j_b; J | \hat{R}^J | 0 \rangle$$

While this coupling order is the correct order when calculating the contribution to $(\bar{H}\hat{R})^{ab}$, the reduced amplitudes are defined in a different coupling order. To compensate, we change the coupling order and introduce a phase (See Edmunds [20] for details)

$$|ba; j_a j_b; J\rangle = (-1)^{j_a + j_b - J} |ba; j_b j_a; J\rangle.$$

Thus, we define

$$\hat{P}(ab) = \hat{1} - (-1)^{j_a + j_b - J} \hat{P}_{a,b}, \quad (\text{B3})$$

and applied to the reduced amplitude $r^{ab}(J)$ this has the correct form

$$\hat{P}(ab) r^{ab}(J) = r^{ab}(J) - (-1)^{j_a + j_b - J} r^{ba}(J).$$

The permutation operators $\hat{P}_{a,c}$ and $\hat{P}_{b,c}$ in Eq. (B2) are a bit more complicated, as they involve three particle states. We use standard expressions for coupling three angular momentum

$$\begin{aligned} |cba; j_a j_b; J_{ab} j_c; J_{abc} M_{abc}\rangle &= - \sum_{J_{cb}} \hat{j}_{cb} \hat{j}_{ab} \begin{Bmatrix} j_c & j_b & J_{cb} \\ j_a & J_{abc} & J_{ab} \end{Bmatrix} \\ &\quad \times |cba; j_c j_b; J_{cb} j_a; J_{abc} M_{abc}\rangle \\ |acb; j_a j_b; J_{ab} j_c; J_{abc} M_{abc}\rangle &= \sum_{J_{ac}} (-1)^{j_b + j_c - J_{ab} + J_{ac}} \hat{j}_{ab} \hat{j}_{ac} \\ &\quad \times \begin{Bmatrix} j_c & j_a & J_{ac} \\ j_b & J_{abc} & J_{ab} \end{Bmatrix} \\ &\quad \times |acb; j_a j_c; J_{ac} j_b; J_{abc} M_{abc}\rangle \end{aligned}$$

Thus, we define

$$\begin{aligned} \hat{P}(ab, c) &= \hat{1} + \sum_{J_{cb}} \hat{j}_{cb} \hat{j}_{ab} \begin{Bmatrix} j_c & j_b & J_{cb} \\ j_a & J_{abc} & J_{ab} \end{Bmatrix} \hat{P}_{a,c} - \\ &\quad \sum_{J_{ac}} (-1)^{j_b + j_c - J_{ab} + J_{ac}} \hat{j}_{ab} \hat{j}_{ac} \times \begin{Bmatrix} j_c & j_a & J_{ac} \\ j_b & J_{abc} & J_{ab} \end{Bmatrix} \hat{P}_{b,c}, \end{aligned} \quad (\text{B4})$$

Since this anti symmetrization contributes a significant part of the overall calculation, all diagrams containing this operator is applied only once to the sum of all diagrams containing this operator.

Appendix C: THREE-BODY PARTS OF \bar{H}

There are two three-body matrix elements of \bar{H} that contributes to the 3P-1H amplitudes. But since the original Hamiltonian does not contain three-body elements, these deserve special attention. These elements can be factorized in just the same way as the coupled-cluster amplitude equations, to reduce the computational cost of these diagrams. The two three-body contributions to the 3P-1H amplitudes are

$$\begin{aligned} (\bar{H}\hat{R})_i^{abc} &\leftarrow \frac{1}{2} \bar{H}_{efi}^{abc} r^{ef} + \frac{1}{2} P(a, bc) \bar{H}_{efi}^{bmc} r_m^{aef} \\ &= -\frac{1}{2} P(a, bc) \bar{H}_{ef}^{am} r^{ef} t_{mi}^{bc} + \frac{1}{2} P(a, bc) \bar{H}_{ef}^{mn} r^{ef} t_{ni}^{bc} t_m^a \\ &\quad + \frac{1}{2} P(a, bc) \bar{H}_{ef}^{mn} t_{ni}^{bc} r_m^{aef}. \end{aligned}$$

These terms are factorized to get

$$(\bar{H}\hat{R})_i^{abc} \leftarrow \frac{1}{2} P(a, bc) t_{im}^{ab} \chi_m^c$$

where we have defined the intermediate

$$\chi_m^c = \bar{H}_{ef}^{cm} r^{ef} + \bar{H}_{ef}^{mn} t_n^c + r_n^{efc}. \quad (\text{C1})$$

Note that we have swapped the indices to facilitate the angular momentum coupling. Now the angular momentum coupling in the coupled-cluster amplitudes match the coupling in the 3P-1H amplitudes, so we do not need to break these couplings when rewriting the diagram in a spherical basis.

In the spherical formulation, it is clear that χ_m^c are the reduced matrix elements of the tensor operator $\hat{\chi}^J$, which has the same rank as \hat{R}^J . This is a consequence of the scalar character of \bar{H} . By coupling the matrix elements in Eq. (C1) to form reduced matrix elements, we get the

following expression for the reduced matrix elements of $\hat{\chi}^J$

$$\begin{aligned} \chi_m^c(J) = & -r^{ef}(J)\bar{H}_{ef}^{mc}(J) + r^{ef}(J)\bar{H}_{ef}^{mn}(J)t_n^c \\ & + \sum_{J_{ef}, J_{efc}} (-1)^{j_c+j_m+J_{ef}-J} \frac{\hat{J}_{ef}}{\hat{J}_{efc}^2} \left\{ \begin{matrix} j_c & j_m & J \\ j_m & J_{efc} & J_{ef} \end{matrix} \right\} \\ & \times r_n^{efc}(J_{ef}, J_{efc}, J)\bar{H}_{ef}^{mn}(J_{ef}). \quad (C2) \end{aligned}$$

Continuum effects and three-nucleon forces in neutron-rich oxygen isotopes

G. Hagen,^{1,2} M. Hjorth-Jensen,^{3,4,5} G. R. Jansen,³ R. Machleidt,⁶ and T. Papenbrock^{2,1}

¹*Physics Division, Oak Ridge National Laboratory, Oak Ridge, TN 37831, USA*

²*Department of Physics and Astronomy, University of Tennessee, Knoxville, TN 37996, USA*

³*Department of Physics and Center of Mathematics for Applications, University of Oslo, N-0316 Oslo, Norway*

⁴*National Superconducting Cyclotron Laboratory, Michigan State University, East Lansing, MI 48824-1321, USA*

⁵*Department of Physics and Astronomy, Michigan State University, East Lansing, MI 48824, USA*

⁶*Department of Physics, University of Idaho, Moscow, ID 83844, USA*

We employ interactions from chiral effective field theory and compute binding energies, excited states, and radii for isotopes of oxygen with the coupled-cluster method. Our calculation includes the effects of three-nucleon forces and of the particle continuum, both of which are important for the description of neutron-rich isotopes in the vicinity of the nucleus ^{24}O . Our main results are the placement of the neutron drip-line at ^{24}O , the assignment of spins, parities and resonance widths for several low-lying states of the drip-line nucleus, and an efficient approximation that incorporates the effects of three-body interactions.

PACS numbers: 21.10.-k, 21.10.Dr, 21.10.Hw, 21.10.Tg, 21.30.-x, 21.60.De, 27.30.+t

Introduction. – Neutron-rich oxygen isotopes are particularly interesting nuclei. First, the nuclei ^{22}O and ^{24}O exhibit double magicity at the neutron numbers $N = 14$ and $N = 16$, respectively, see for example Refs. [1–3]. Second, oxygen is the heaviest element for which the neutron drip line is established experimentally. The recent experiments [4, 5] show clearly that the nuclei $^{25,26}\text{O}$ are unbound, thus making ^{24}O the most neutron-rich bound isotope of oxygen. The spectroscopy of the drip line nucleus ^{24}O was studied in a recent experiment [6]. One of the exciting results of this study is a state with an unknown spin and parity at about 7.5 MeV of excitation energy. Theoretical studies in this region of the nuclear chart are challenging [7–10]. Volya and Zelevinsky [7] employed an empirical two-body shell-model interaction (above the core of ^{16}O) and included the particle continuum in their calculation of neutron-rich oxygen isotopes. Otsuka *et al.* [9] included three-nucleon forces (3NFs) within the *sd*-shell model (keeping ^{16}O as a core with empirical single-particle energies) and found that three-body forces yield ^{24}O at the neutron drip line. The *ab initio* computations of neutron-rich oxygen isotopes by Hagen *et al.* [8] employed microscopic interactions from chiral effective field theory [11], had no core, but were limited to nucleon-nucleon (*NN*) interactions. Thus, we are still lacking a complete computation of neutron rich oxygens that properly accounts for (i) the effects of three-nucleon forces, (ii) the presence of open decay channels and particle continuum, and (iii) many-nucleon correlations. It is the purpose of this Letter to fill this gap. In particular we predict the spins and lifetimes of several resonances in ^{24}O at excitation energies around 7 MeV and thereby shed light on the recent experiment [6].

Effective field theory (EFT) is the framework that allows for a consistent formulation of low-energy nuclear Hamiltonians and currents [11–13]. Within chiral EFT, 3NFs are important contributions that enter at next-to-

next-to-leading order in the power counting. In light nuclei, our understanding of 3NFs has improved considerably over the past decade, and nuclear binding energies, spectra and decays cannot be understood without them [14–18]. The study of the role of 3NFs in medium-mass nuclei and exotic, neutron-rich nuclei is a frontier in contemporary nuclear structure theory. To date, the full inclusion of 3NFs is limited to *p*-shell nuclei. For heavier nuclei or nuclear matter, several approaches [9, 10, 19–21] employ a normal-ordered approximation [22], resulting in a medium-dependent two-body potential that includes effects of the 3NFs. Furthermore, the employed interactions are renormalization group transformations [23] of interactions from chiral EFT.

Hamiltonian and model space. – The intrinsic *A*-nucleon Hamiltonian used in this work reads

$$\hat{H} = \sum_{1 \leq i < j \leq A} \left(\frac{(\vec{p}_i - \vec{p}_j)^2}{2mA} + \hat{V}_{NN}^{(i,j)} + \hat{V}_{3\text{Neff}}^{(i,j)} \right). \quad (1)$$

Here, the intrinsic kinetic energy depends on the mass number *A*. The potential \hat{V}_{NN} is the chiral *NN* interaction developed by Entem and Machleidt [11] at next-to-next-to-next-to-leading order (*N³LO*) within chiral EFT. The potential $\hat{V}_{3\text{Neff}}$ is the in-medium *NN* interaction derived by Holt *et al.* [19] from the leading order chiral 3NF by integrating one nucleon over the Fermi sea (i.e. up to the Fermi momentum k_F) in symmetric nuclear matter. The leading chiral 3NF depends on five low-energy constants (LECs). The LECs $c_1 = -0.81 \text{ GeV}^{-1}$, $c_3 = -3.20 \text{ GeV}^{-1}$, and $c_4 = 5.40 \text{ GeV}^{-1}$ appear also in the two-pion exchange part of the chiral *NN* interaction and have the same values as in the *N³LO* *NN* potential we employ [11]. The remaining LECs of the 3NF are set at $c_D = -0.2$ and $c_E = 0.71$ together with $\Lambda_\chi = 0.7 \text{ GeV}$. For the oxygen isotopes considered in this work we apply the Fermi momentum $k_F = 1.05 \text{ fm}^{-1}$ in our potential $\hat{V}_{3\text{Neff}}$. Consistent with the *NN* force, the effective cutoff

for the 3NF is $\Lambda = 500$ MeV.

Let us comment on our phenomenological two-body potential $\hat{V}_{3\text{Neff}}$ that contains effects of 3NFs. The normal-ordered approximation of 3NFs [9, 21, 22] still requires one to compute an enormous number of three-body matrix elements. This poses a great challenge for the large model spaces we need to consider. The approach of this Letter is thus simpler: The summation over the third particle is performed in momentum space *before* the transformation to the oscillator basis takes place [39]. This procedure avoids the costly computation of three-body matrix elements in large oscillator spaces, but it introduces an uncontrolled approximation by replacing the mean-field of a finite nucleus by that of symmetric nuclear matter. To correct for this approximation, we adjusted the LEC c_E away from the optimal value established in light nuclei [25].

The coupled-cluster method is essentially a similarity transformation of the Hamiltonian with respect to a reference state. This method is accurate and efficient for nuclei with closed (sub-)shells [26–28]. We compute the ground states of $^{16,22,24,28}\text{O}$ within the singles and doubles approximation, while three-particle-three-hole ($3p\text{-}3h$) excitations are included in the $\Lambda\text{-CCSD(T)}$ approach of Ref. [30]. For excited states in these closed-shell isotopes we employ the equation-of-motion (EOM) coupled-cluster method with singles and doubles. The open-shell nuclei $^{15,17,21,23,25}\text{O}$ are computed within the particle attached/removed EOM formalism, and we employ the two-particle attached EOM formalism [31] for the nuclei $^{18,26}\text{O}$. For details about our implementation see Ref. [29]. These EOM methods work very well for states with dominant $1p\text{-}1h$, $1p$, $1h$, and $2p$ structure, respectively. We use a Hartree-Fock basis built in 17 major oscillator shells and varied the oscillator spacing $\hbar\omega$ between 24 MeV and 32 MeV. Well converged energy minima are found at $\hbar\omega \approx 28$ MeV for all oxygen isotopes. Open decay channels and the particle continuum near the dripline nucleus ^{24}O are included within the Gamow shell model [32, 33]. The single-particle bound and scattering states result from diagonalizing a spherical Woods-Saxon Hamiltonian in a discrete momentum basis in the complex plane [33, 34]. In the case of computing resonances in ^{24}O we used 35 mesh points for the $d_{3/2}$ partial wave on a rotated/translated contour in the complex momentum plane as described in Ref. [35]. The excited states we compute in $^{22,24}\text{O}$ are dominated by $1p\text{-}1h$ excitations and continuum mixing from other partial waves is small. They result as solutions of a complex-symmetric eigenvalue problem, and the imaginary part of the energy yields the width of the state. In computing radii we discretized the real momentum axis with 40 points for the neutron and proton partial waves closest to the threshold. This guarantees the correct exponential decay of matter and charge densities at large distances.

Results. – Figure 1 shows the ground-state energies

of the computed oxygen isotopes (red squares) compared with experimental data (black circles) and results limited to chiral NN interactions only (blue diamonds). For the isotopes around ^{16}O , NN interactions alone already describe separation energies rather well, and the inclusion of effects of 3NFs mainly changes underbinding into overbinding. For the more neutron-rich oxygen isotopes, the 3NFs significantly change the systematics of the binding energies, and energy differences are particularly well reproduced. The nuclei $^{25,26}\text{O}$ are unbound with respect to ^{24}O by about 0.4 MeV and about 0.1 MeV, respectively, in good agreement with experiments [4, 5]. We predict ^{28}O to be unbound with respect to ^{24}O by about 4 MeV and with a resonant width of about 1 MeV. The extremely short life time of ^{28}O poses a challenge for experimental observation. The energy difference between light and heavy oxygen isotopes is not correctly reproduced when compared to data. We believe that this is due to the fact that our interaction $\hat{V}_{3\text{Neff}}$ is based on symmetric nuclear matter. For smaller values of k_F , the ground-state energy of the lighter oxygen isotopes is increased (and can be brought to good agreement with data), while the heavier isotopes are significantly underbound. The value we chose for k_F is thus a compromise.

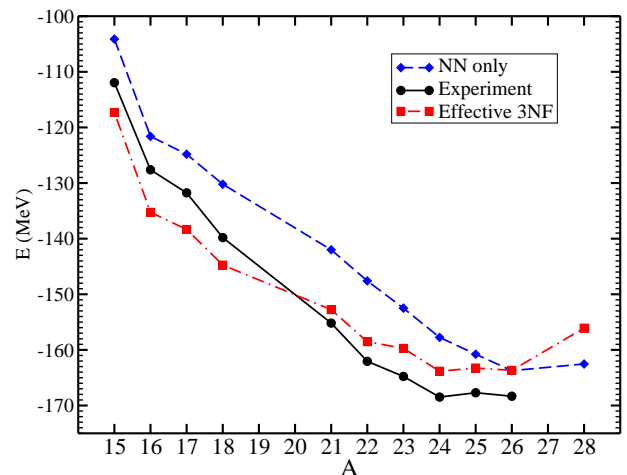


FIG. 1: (Color online) Ground-state energy of the oxygen isotope ^AO as a function of the mass number A . Black circles: experimental data; blue diamonds: results from nucleon-nucleon interactions; red squares: results including the effects of three-nucleon forces.

Let us comment on our computation of oxygen isotopes with open shells. First, we solve the CCSD equations for the Hamiltonian (1) of the closed-shell reference state, but employ the mass number $A \pm 1$ in the intrinsic kinetic energy. In a second step, we add (remove) a neutron within the particle attached (removed) EOM. This procedure ensures that the final result is obtained for the intrinsic (i.e., translationally invariant) Hamiltonian of $^{A\pm 1}\text{O}$. The $J^\pi = 1/2^+$ ground state energy

of ^{23}O , shown in Fig. 1, resulted from using particle-removal EOM from ^{24}O . For $^{18,26}\text{O}$, we performed a two-neutron attached EOM computation based on the reference states for $^{16,24}\text{O}$, the latter being computed with the mass number $A = 18, 26$ in the intrinsic kinetic energy. This approach is unproblematic for separation energies but it introduces an error in the computation of resonance widths. Our computation of ^{25}O within the neutron attached EOM employs a Gamow basis. Here the continuum threshold is incorrectly set by the closed-shell reference of ^{24}O , computed with the mass number $A = 25$ in the intrinsic kinetic energy. Clearly, this introduces a small error by shifting the scattering threshold, and thereby affects the widths of resonance states that are very close to the threshold. In Ref. [36] we showed that the coupled-cluster wave function factorizes into an intrinsic and a center-of-mass part. The center-of-mass wave function is to a very good approximation a Gaussian with a frequency $\hbar\omega \approx 14$ MeV for ^{24}O . Thus, we estimate the error introduced in the scattering threshold of ^{25}O to be $\frac{3}{4}\hbar\omega/A \approx 0.4$ MeV.

Figure 2 shows the excitation spectra of neutron-rich oxygen isotopes and compares the results limited to chiral NN interactions (blue lines) to the results obtained with our inclusion of 3NFs (red lines), and to experimental data (black lines) [40]. The particle continua above the scattering thresholds are shown as gray bands. Calculations limited to NN interactions yield the correct level ordering but very compressed spectra when compared to data, and all the computed excited states are well bound with respect to the neutron emission thresholds. However, the inclusion of 3NFs increases the level spacing and significantly improves the agreement with experiment. Several of the excited states are resonances in the continuum, and the proximity of the continuum is particularly relevant for the dripline nucleus ^{24}O . Here, the Gamow basis is essential for a proper description of the excited resonant states. In ^{24}O we find three resonant states near the unknown experimental state at about 7.5 MeV of excitation energy [6]. The excited $J^\pi = 3/2^+$ state in ^{23}O is computed as a neutron attached to ^{22}O , while the excited $J^\pi = 5/2^+$ state is computed by neutron removal from ^{24}O . Since we are interested in the excitation energy relative to the ground state we compute the $J^\pi = 1/2^+$ ground state either by adding or removing a particle, consistent with the particular excited state. For the lighter isotopes $^{15,16,17}\text{O}$, our inclusion of 3NFs yields only smaller changes to the spectra when compared with results from NN interactions only.

For the closed-shell nucleus ^{24}O we also computed resonance widths of excited states that are dominated by $1p-1h$ excitations from the $s_{1/2}, d_{5/2}$ hole to the $d_{3/2}$ particle orbitals. Table I shows that the first $J^\pi = 2^+$ and 1^+ excited states agree well with experimental data, both for the excitation energy and the resonance widths. The rather small widths and quasi-bound nature of these

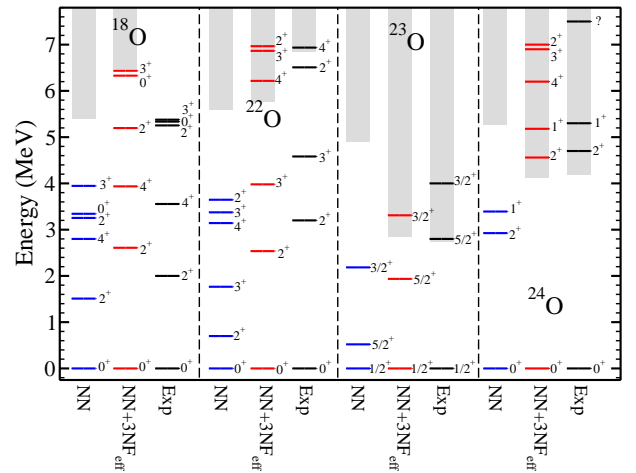


FIG. 2: (Color online) Excitation spectra of oxygen isotopes computed from chiral nucleon-nucleon interactions, with inclusion of the effects of three-nucleon forces, and compared to data.

J^π	2_1^+	1_1^+	4_1^+	3_1^+	2_2^+	1_2^+
E_{CC}	4.56	5.2	6.2	6.9	7.0	8.4
E_{Exp}	4.7(1)	5.33(10)				
Γ_{CC}	0.03	0.04	0.005	0.01	0.04	0.56
Γ_{Exp}	$0.05^{+0.21}_{-0.05}$	$0.03^{+0.12}_{-0.03}$				

TABLE I: Excited states in ^{24}O computed within EOM-CCSD compared to experimental data from Ref. [6]. Energies and widths are in MeV.

states can be attributed to the large angular momentum barrier of the $d_{3/2}$ orbital, together with neutron pairing effects. Above these 2_1^+ and 1_1^+ resonances we find several states with spin and parity $J^\pi = 1^+$ to 4^+ and excitation energies ranging from 6.2 MeV to 8.4 MeV. The small ratio $E_{4_1^+}/E_{2_1^+} \approx 1.36$ and the relatively high energy $E_{2_1^+}$ lend theoretical support to the doubly magic nature of ^{24}O [3]. The low experimental resolution of the resonance at 7.5 MeV let Hoffman *et al.* [6] to speculate that this resonance could be a superposition of narrow resonances with spins and parity $J^\pi = 1^+$ to 4^+ . Our calculation clearly supports this suggestion, except for the 1_2^+ state which we find at 8.4 MeV of excitation energy and with a width of 0.56 MeV.

Figure 3 shows the computed point matter and point charge radii for the neutron-rich isotopes $^{21-24}\text{O}$ with a comparison to the experimental data (Ref. [37] for ^{21}O and Ref. [38] for $^{22,24}\text{O}$). This computation employs the intrinsic density with respect to the center of mass. Our computed radii agree very well with experiment for the odd isotopes $^{21,23}\text{O}$, while for ^{22}O we underestimate the radii compared to experiment. We also computed the point matter radii from NN interactions only (blue di-

amonds). In this case the radii overestimate the data for $^{21,23}\text{O}$, while $^{22,24}\text{O}$ they are closer to the results with effects of 3NF's included. The computed charge radii clearly exhibit an odd-even staggering consistent with the shell closures at neutron numbers $N = 14, 16$. For ^{16}O , the computed point matter and charge radii are 2.23 fm and 2.24 fm, respectively. This is about 0.3 fm smaller than experiment and consistent with the computed overbinding and the increased neutron and proton separation energies.

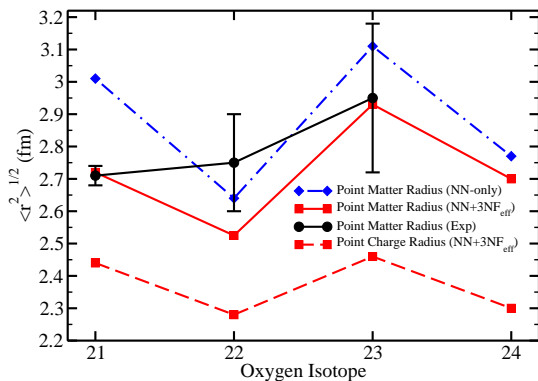


FIG. 3: (Color online) Point matter and point charge radii of neutron rich oxygen isotopes computed from chiral nucleon-nucleon interactions, with inclusion of the effects of three-nucleon forces, and compared to data.

Summary. – We employed interactions from chiral effective field theory, performed coupled-cluster computations of oxygen isotopes, and included effects of the particle continuum and of three-nucleon forces. Three-nucleon forces were approximated as in-medium nucleon-nucleon forces. This approach is computationally feasible and in keeping with the spirit of effective field theory. Compared to computations based on nucleon-nucleon interactions alone, the included 3NFs yield a significant improvement in binding energies and spectra. Our results confirm that chiral interactions yield the neutron drip line at ^{24}O , and we are able to compute spin, parities and resonance widths for several excited states close to the dripline. In particular, we compute several long-lived resonances at about 7 MeV of excitation energy in ^{24}O .

This work was supported by the Office of Nuclear Physics, U.S. Department of Energy (Oak Ridge National Laboratory), and through the Grants Nos. DE-FG02-03ER41270 (University of Idaho), DE-FG02-96ER40963 (University of Tennessee), and DE-FC02-07ER41457 (UNEDF SciDAC). This research used computational resources of the National Center for Computational Sciences, the National Institute for Computational Sciences, and the Notur project in Norway.

- [1] P. Thirolf *et al.*, Phys. Lett. B **485**, 16 (2000).
- [2] C. R. Hoffman *et al.*, Phys. Lett. B **672**, 17 (2009).
- [3] R. Kanungo *et al.*, Phys. Rev. Lett. **102**, 152501 (2009).
- [4] C. R. Hoffman *et al.*, Phys. Rev. Lett. **100**, 152502 (2008).
- [5] E. Lunderberg *et al.*, Phys. Rev. Lett. **108**, 142503 (2012).
- [6] C. R. Hoffman *et al.*, Phys. Rev. C **83**, 031303(R) (2011).
- [7] A. Volya and V. Zelevinsky, Phys. Rev. Lett. **94**, 052501 (2005).
- [8] G. Hagen *et al.*, Phys. Rev. C **80**, 021306 (2009).
- [9] T. Otsuka *et al.*, Phys. Rev. Lett. **105**, 032501 (2010).
- [10] J. D. Holt and A. Schwenk, arxiv:1108:2680.
- [11] D. R. Entem and R. Machleidt, Phys. Rev. C **68**, 041001(R) (2003).
- [12] E. Epelbaum, H. W. Hammer, and Ulf-G. Meissner, Rev. Mod. Phys. **81**, 1773 (2009).
- [13] R. Machleidt and D. R. Entem, Phys. Rep. **503**, 1 (2011).
- [14] R. B. Wiringa and S. C. Pieper, Phys. Rev. Lett. **89**, 182501 (2002).
- [15] P. Navrátil and W. E. Ormand, Phys. Rev. Lett. **88**, 152502 (2002).
- [16] P. Navrátil *et al.*, J. Phys. G **36**, 083101 (2009).
- [17] E. Epelbaum *et al.*, Phys. Rev. Lett. **106**, 192501 (2011).
- [18] P. Maris *et al.*, Phys. Rev. Lett. **106**, 202502 (2011).
- [19] J. W. Holt, N. Kaiser, and W. Weise, Phys. Rev. C **79**, 054331 (2009); *ibid.* Phys. Rev. C **81**, 024002 (2010).
- [20] K. Hebeler and A. Schwenk, Phys. Rev. C **82**, 014314 (2010); K. Hebeler *et al.*, Phys. Rev. C **83**, 031301 (2011).
- [21] R. Roth *et al.*, Phys. Rev. Lett. **107**, 072501 (2011).
- [22] G. Hagen *et al.*, Phys. Rev. C **76**, 034302 (2007).
- [23] S. K. Bogner, T. T. S. Kuo, and A. Schwenk, Phys. Rep. **386**, 1 (2003); S. K. Bogner, R. J. Furnstahl and R. J. Perry, Phys. Rev. C **75**, 061001 (2007).
- [24] J. Menéndez, D. Gazit, and A. Schwenk, Phys. Rev. Lett. **107**, 062501 (2011).
- [25] D. Gazit, S. Quaglioni, and P. Navrátil, Phys. Rev. Lett. **103**, 102502 (2009).
- [26] F. Coester, Nucl. Phys. **7**, 421 (1958); F. Coester and H. Kümmel, Nucl. Phys. **17**, 477 (1960); J. Čížek, J. Chem. Phys. **45**, 4256 (1966); J. Čížek, Adv. Chem. Phys. **14**, 35 (1969); H. Kümmel, K.H. Lührmann, and J.G. Zabolitzky, Phys. Rep. **36**, 1 (1978).
- [27] D. J. Dean and M. Hjorth-Jensen, Phys. Rev. C **69**, 054320 (2004).
- [28] R. J. Bartlett and M. Musiał, Rev. Mod. Phys. **79**, 291 (2007).
- [29] G. Hagen *et al.*, Phys. Rev. C **82**, 034330 (2010).
- [30] A. D. Taube and R. J. Bartlett, J. Chem. Phys. **128**, 044110 (2008); *ibid.* **128**, 044111 (2008).
- [31] G. R. Jansen *et al.*, Phys. Rev. C **83**, 054306 (2011).
- [32] R. Id Betan *et al.*, Phys. Rev. Lett. **89**, 042501 (2002).
- [33] N. Michel *et al.*, Phys. Rev. Lett. **89**, 042502 (2002); N. Michel *et al.*, J. Phys. G **36**, 013101 (2009).
- [34] Ø. Jensen *et al.*, Phys. Rev. Lett. **107**, 032501 (2011).
- [35] G. Hagen *et al.*, Phys. Lett. B **656**, 169 (2007).
- [36] G. Hagen, T. Papenbrock, D. J. Dean, Phys. Rev. Lett. **103**, 062503 (2009).
- [37] A. Ozawa *et al.*, Nucl. Phys. A **691**, 599 (2001).
- [38] R. Kanungo *et al.*, Phys. Rev. C **84**, 061304 (2011).
- [39] For the approximation of two-body currents as medium-dependent one-body currents, this approach has been

used in Ref. [24].
 [40] The displayed experimental levels are dominated by

$1p(h)$, $2p$ or $1p-1h$ excitations.

Evolution of shell structure in neutron-rich calcium isotopes

G. Hagen,^{1,2} M. Hjorth-Jensen,^{3,4} G. R. Jansen,³ R. Machleidt,⁵ and T. Papenbrock^{2,1}

¹*Physics Division, Oak Ridge National Laboratory, Oak Ridge, TN 37831, USA*

²*Department of Physics and Astronomy, University of Tennessee, Knoxville, TN 37996, USA*

³*Department of Physics and Center of Mathematics for Applications, University of Oslo, N-0316 Oslo, Norway*

⁴*National Superconducting Cyclotron Laboratory and Department of Physics and Astronomy,
Michigan State University, East Lansing, MI 48824, USA*

⁵*Department of Physics, University of Idaho, Moscow, ID 83844, USA*

We employ interactions from chiral effective field theory and compute the binding energies and low-lying excitations of calcium isotopes with the coupled-cluster method. Effects of three-nucleon forces are included phenomenologically as in-medium two-nucleon interactions, and the coupling to the particle continuum is taken into account using a Berggren basis. The computed ground-state energies and the low-lying $J^\pi = 2^+$ states for the isotopes ^{42,48,50,52}Ca are in good agreement with data, and we predict the excitation energy of the first $J^\pi = 2^+$ state in ⁵⁴Ca to be similar to the one in ⁵²Ca. In the odd-mass nuclei ^{53,55,61}Ca we find that the positive parity states deviate strongly from the naive shell model.

PACS numbers: 21.10.Dr, 21.30.-x, 21.60.De, 27.40.+z, 27.50.+e

Introduction. – The shell model is the paradigm for our understanding of atomic nuclei. Doubly magic nuclei (i.e., nuclei that exhibit an enhanced stability) are its cornerstones, and they determine the properties of nuclei in entire regions of the nuclear chart. The magic numbers – established *ad hoc* via a mean field plus a strong spin-orbit interaction more than 60 years ago by Mayer and Jensen for beta-stable nuclei [1] – are modified in neutron-rich nuclei, see for example Ref. [2] for a recent review. The magic nature of nuclei is reflected experimentally in enhanced neutron separation energies and a reduced quadrupole collectivity (i.e., a relatively high-lying first excited $J^\pi = 2^+$ state and relatively small electromagnetic transition probabilities from this state to the $J^\pi = 0^+$ ground state). In doubly magic nuclei such as ⁴⁰Ca and ⁴⁸Ca, the $J^\pi = 2^+$ state appears at an excitation energy close to 4 MeV, while in open-shell calcium isotopes like ^{42,44,46,50}Ca, this excitation energy is closer to 1 MeV. How these quantities evolve as we move towards the driplines is an open issue in ongoing nuclear structure research and is intimately related to our fundamental understanding of shell evolution in nuclei.

For the theoretical understanding of shell evolution, phenomenological terms such as the tensor interaction [3] have been proposed. In a modern picture, three-nucleon forces (3NFs) play a pivotal role in shell evolution [4]. In the oxygen isotopes, for instance, 3NFs make ²⁴O doubly magic and a dripline nucleus [5–7]. Similarly, Holt *et al.* [8] showed that 3NFs are greatly responsible for the magic neutron number $N = 28$. On the other hand, experiment and theory show that the next possible magic number, $N = 32$, exhibits a smaller value for the 2^+ excitation (but more than twice as large as seen in open-shell calcium isotopes) than observed in ⁴⁸Ca. This is often referred to as a sub-shell closure. The $N = 32$ sub-shell closure is well established from experiments in

calcium [9, 10], titanium [11], and chromium [12]. However, the situation is more complicated for neutron-rich calcium isotopes. For the neutron number $N = 34$, no sub-shell closure is seen experimentally in chromium [13] or titanium [14, 15], and there are some doubts regarding a sub-shell closure in calcium [16]. Different theoretical predictions have been made around $N = 34$. Within the *fp* shell-model space, the empirical interaction GXPF1 [17] predicts a strong shell gap in ⁵⁴Ca, while the monopole-corrected KB3 interaction [18] yields no shell gap. A low-momentum shell-model interaction with empirical single-particle energies and a ⁴⁸Ca core yields no shell gap in ⁵⁴Ca [19]. Shell-model calculations that include 3NFs predict a shell closure in ⁵⁴Ca in the *fp* model space, and this shell closure is reduced to a sub-shell closure (similar in strength to the $N = 32$ sub-shell closure in ⁵²Ca) in an enlarged model space that also includes the $g_{9/2}$ orbital [8]. Thus, the picture regarding the shell gap in ⁵⁴Ca is not settled yet. The theoretical prediction of the shell evolution in calcium isotopes is a challenging task that requires a very good understanding of the nuclear interaction, accurate treatment of many-body correlations and coupling to the scattering continuum [20]. To study the shell evolution, we will focus on neutron separation energies, the energies of the first excited $J^\pi = 2^+$ states, and spectra in the nuclei ^{53,55,61}Ca, which differ by one neutron from nuclei that exhibit a closed subshell in the naive shell model.

In this Letter, we present a state-of-the-art prediction for the shell evolution of neutron-rich calcium isotopes. To this purpose, we employ nucleon-nucleon (*NN*) interactions from chiral effective field theory (EFT) together with a schematic approximation of 3NFs guided by chiral EFT, and utilize the coupled-cluster method to solve the quantum many-body problem. Chiral EFT is a systematic and model-independent approach to nuclear interac-

tions. We employ the NN interactions at next-to-next-to leading order by Entem and Machleidt [21, 22], and an approximation for the chiral 3NFs that was previously adopted in neutron-rich oxygen isotopes [7]. The coupled-cluster method [23, 24] is a very efficient tool for the computation of nuclei with a closed (sub-)shell structure and their neighbors, and thus ideally suited for the task at hand.

Hamiltonian, model space, and method. – We employ the intrinsic Hamiltonian

$$\hat{H} = \sum_{1 \leq i < j \leq A} \left(\frac{(\vec{p}_i - \vec{p}_j)^2}{2mA} + \hat{V}_{NN}^{(i,j)} + \hat{V}_{3\text{Neff}}^{(i,j)} \right). \quad (1)$$

Here, the intrinsic kinetic energy depends on the mass number A . The potential \hat{V}_{NN} denotes the chiral NN interaction at next-to-next-to-next-to leading order [21, 22], while $\hat{V}_{3\text{Neff}}$ is a schematic potential based on the in-medium chiral NN interaction by Holt *et al.* [25] (see also Ref. [26]). The potential $\hat{V}_{3\text{Neff}}$ results from integrating one nucleon in the leading-order chiral 3NF over the Fermi sphere with Fermi momentum k_F in symmetric nuclear matter and is thus reminiscent of the normal-ordered approximation [27]. It depends formally on the Fermi momentum k_F , the low-energy constants c_D and c_E of the short-ranged contributions to the leading-order chiral 3NF, and the chiral cutoff. The latter is equal to the value employed in the chiral NN interaction [21]. In the computation of neutron-rich oxygen isotopes [7], the parameters $k_F = 1.0 \text{ fm}^{-1}$ and $c_E = 0.7$ resulted from adjusting the binding energies of $^{16,22}\text{O}$, while $c_D = -0.2$ was kept at its value determined in light nuclei [28]. In this work, we use $c_E = 0.68$ from adjusting the binding energy of ^{48}Ca . This small change in c_E reduces the binding energies of ^{48}Ca by about 6 MeV. It is very satisfying that the parameterization of $\hat{V}_{3\text{Neff}}$ changes only little as one goes from neutron-rich isotopes of oxygen to the significantly heavier calcium isotopes.

The coupled-cluster method generates a similarity-transformed Hamiltonian $\bar{H} = e^{-T} \hat{H} e^T$ by the action of the cluster operator T that creates up to n -particle- n -hole (np - nh) excitations with respect to a reference state. Details of our implementation are presented in Refs. [29, 30]. We compute the ground states of the closed-(sub)shell nuclei $^{40,48,52,54,60,62}\text{Ca}$ in the singles doubles (CCSD) approximation and include $n = 3$ triples perturbatively within the Λ -CCSD(T) approach of Ref. [31]. Our model space consists of up to $N_{\text{max}} = 19$ major spherical oscillator shells (i.e., the maximal single-particle excitation energy is 18 units of $\hbar\omega$ above the oscillator ground state), and the reference state results from a Hartree-Fock calculation. Our basis employs oscillator spacings between $24 \text{ MeV} \leq \hbar\omega \leq 32 \text{ MeV}$, and in the largest model spaces the results we present are practically independent of $\hbar\omega$. For excited states above threshold which are dominated by low- j orbitals, we use

Gamow-Hartree-Fock basis [7, 32]. Excited states of closed-shell nuclei are computed within the equation-of-motion (EOM) method with singles and doubles. The open-shell nuclei $^{39,41,47,49,51,53,55,59,61}\text{Ca}$ are computed with the particle attached/removed EOM methods, and we use the two-particle attached EOM method [33] for the nuclei $^{42,50,56}\text{Ca}$. Note that the employed EOM methods are expected to reliably compute the separation energies and low-lying excited states as long as they are dominated by $1p$, $1h$, $1p$ - $1h$ or $2p$ excitations.

Results. – Figure 1 shows the computed ground-state energies of the calcium isotopes and compares the results obtained with the Hamiltonian of Eq. (1) to available data and to the results based on chiral NN interactions alone. The inclusion of chiral 3NFs via the in-medium effective potential $\hat{V}_{3\text{Neff}}$ clearly yields a good agreement with data. The light isotopes $^{39,40,41}\text{Ca}$ are slightly overbound. The comparison with chiral NN forces shows that the in-medium effective potential $\hat{V}_{3\text{Neff}}$ is repulsive [39]. For the heavier isotopes of calcium, the in-medium effective potential $\hat{V}_{3\text{Neff}}$ becomes increasingly repulsive, and a saturation of the total binding energy sets in around ^{60}Ca . It is interesting that essentially the same interaction yields attraction in neutron-rich oxygen isotopes [7]. Note that the results for the isotopes $^{52-60}\text{Ca}$ are based on an exponential extrapolation of our results for $N_{\text{max}} = 14, 16, 18$ oscillator shells at the oscillator frequency $\hbar\omega = 26 \text{ MeV}$. This extrapolation adds 0.6 MeV of binding energy in ^{52}Ca and 1.3 MeV in ^{60}Ca . For the other nuclei our results are practically converged with 19 shells. As a check, we also employed a Gamow Hartree-Fock basis for the s - p - d neutron partial waves and computed the ground states for the isotopes $^{54,60}\text{Ca}$. The differences are small (up to about 0.3 MeV) and barely noticeable on the scale of Fig. 1.

Figure 2 shows the energies of the $J^\pi = 2^+$ states in the isotopes $^{42,48,50,52,54,56}\text{Ca}$, computed in a model space with $N_{\text{max}} = 18$ and $\hbar\omega = 26 \text{ MeV}$ for $^{48,52,54}\text{Ca}$ and $N_{\text{max}} = 16$ and $\hbar\omega = 28 \text{ MeV}$ for $^{42,50,56}\text{Ca}$. Where data is available, we obtain a good agreement between theory and experiment. The 3NFs generate the shell closure in ^{48}Ca and make $N = 28$ a magic number. We also computed the $J^\pi = 2^+$ excited state in ^{48}Ca using chiral NN forces alone, and we obtained $E_{2^+} = 2.07 \text{ MeV}$; this shows that the magicity of ^{48}Ca is due to the effects of 3NFs in our approach. Our results predict that ^{54}Ca exhibits a sub-shell closure that is similar in strength to the sub-shell closure in ^{52}Ca , and this is one of the main results of this Letter.

To further demonstrate this point, we also computed the energies of the first excited $J^\pi = 4^+$ states, and neutron separation energies S_n . The results in Table I show that theory and experiment agree well for the available data. The theoretical results for ^{54}Ca suggest strongly that this nucleus will only exhibit a sub-shell closure but not a shell closure. The neutron separation energy in

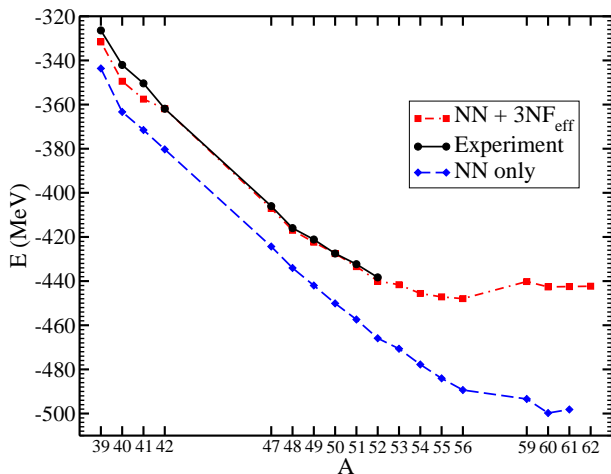


FIG. 1: (Color online) Ground-state energy of the calcium isotopes as a function of the mass number A . Black circles: experimental data; red squares: theoretical results including the effects of three-nucleon forces; blue diamonds: predictions from chiral NN forces alone. The experimental results for $^{51,52}\text{Ca}$ are from Ref. [34].

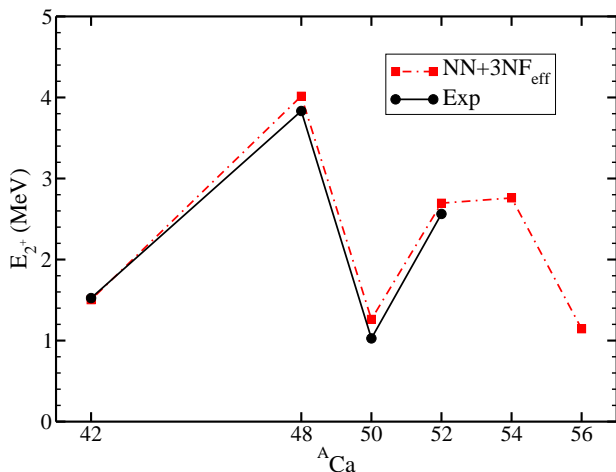


FIG. 2: (Color online) Excitation energies of $J^\pi = 2^+$ states in the isotopes $^{42,48,50,52,54,56}\text{Ca}$ (experiment: black, theory: red).

^{52}Ca is a noteworthy example. The atomic mass table evaluation [35] gives the value $S_n = 4.7$ MeV (estimated from systematics) for this nucleus. The very recent measurement [34], however, yields $S_n \approx 6$ MeV, in much better agreement with our prediction of $S_n = 6.65$ MeV.

To further study the evolution of shell structure we focus on spectra. Figure 3 shows the computed spectra for $^{52-56}\text{Ca}$, and compares them to available data. In $^{52,53}\text{Ca}$, our calculations suggest spin assignments for measured levels, while we give predictions for several levels in $^{53,54,55,56}\text{Ca}$. The scattering continuum is shown as a gray band. Note that we computed the

$J^\pi = 2^+, 4^+$ excited states of ^{54}Ca as $1p-1h$ excitations of the ^{54}Ca ground state and as $2p$ excitations of the ^{52}Ca ground state. In 17 major oscillator shells we obtain $E_{2^+,4^+} = 2.70, 5.83$ MeV and $E_{2^+,4^+} = 2.72, 5.88$ MeV, respectively. The two methods are in excellent agreement with each other, and this shows the quality of the employed methods.

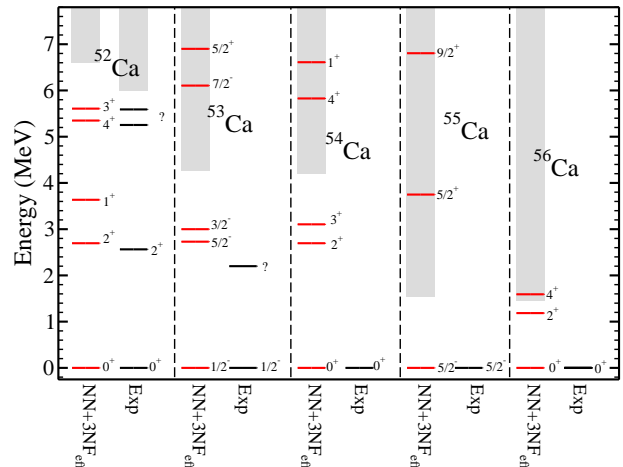


FIG. 3: (Color online) Theoretical excitation spectra of $^{52-56}\text{Ca}$ compared to available data. The continuum is indicated as a gray area.

In the naive shell-model picture, the order of single-particle orbitals above the Fermi surface of ^{60}Ca is $g_{9/2}$, $d_{5/2}$ and $s_{1/2}$. Mean-field calculations predict that the corresponding canonical orbitals are close in energy [36], yielding deformation in the isotopes $^{60-70}\text{Ca}$ [37]. The isotope ^{58}Ca is the heaviest isotope of calcium that has been produced [38], and ^{52}Ca is the most neutron-rich isotope whose mass is known [34]. Nuclear energy functionals and mass models [36, 37] predict the neutron drip line to be around ^{70}Ca . Figure 3 shows that the

	^{48}Ca	^{52}Ca	^{54}Ca
$E_{2^+}(\text{CC})$	4.02	2.70	2.76
$E_{2^+}(\text{Exp})$	3.83	2.56	n.a.
$E_{4^+}/E_{2^+}(\text{CC})$	1.13	1.92	2.16
$E_{4^+}/E_{2^+}(\text{Exp})$	1.17	n.a.	n.a.
$S_n(\text{CC})$	9.90	6.65	4.20
$S_n(\text{Exp})$	9.95	6.0*	4.0†

TABLE I: Excitation energies E_{2^+} (in MeV) of the lowest-lying $J^\pi = 2^+$ states, neutron-separation energies S_n (in MeV), and ratio of energies E_{4^+}/E_{2^+} from coupled-cluster theory (CC) compared to available data (Exp) [n.a. = not available; * = from Ref. [34]; † = from atomic mass table evaluation [35]]. The theoretical results point to a sub-shell closure in ^{54}Ca .

$J^\pi = 5/2^+$ resonant excited states in $^{53,55}\text{Ca}$ are lower in energy than the $J^\pi = 9/2^+$ states, and this is a deviation from the naive shell-model picture. There is no $J^\pi = 1/2^+$ resonance in the continuum due to absence of a centrifugal barrier. Due to the large $l = 4$ centrifugal barrier the $J^\pi = 9/2^+$ resonances can be considered as quasi-bound states, while the $J^\pi = 5/2^+$ has a significantly larger width, see Table II for details. Our results shown in Fig. 1 yield ^{60}Ca unbound with respect to ^{56}Ca . However, we cannot rule out the existence of ^{60}Ca since correlations beyond triples in the coupled-cluster expansion may play a larger role for ^{60}Ca than for the neighbors of ^{54}Ca . Our computations (including the scattering continuum) suggest that ^{61}Ca is a very interesting nucleus. We find resonant states $J^\pi = 5/2^+$ and $J^\pi = 9/2^+$ at excitation energies of 1.5 MeV and 2.7 MeV above threshold, respectively, and a virtual $J^\pi = 1/2^+$ state practically at threshold. This ordering of the resonances is consistent with the results for $^{53,55}\text{Ca}$. Table II summarizes our results for the $J^\pi = 5/2^+$ and $J^\pi = 9/2^+$ resonances in $^{53,55,61}\text{Ca}$. We also find the ^{62}Ca ground state to be very close to threshold, unbound by about 0.3 MeV with respect to ^{60}Ca and entirely dominated by $(s_{1/2})^2$ configurations. In our calculations, the correct treatment of the continuum is essential: (i) in ^{55}Ca the scattering continuum lowers the energy of the excited $J^\pi = 5/2^+$ by about 2 MeV when compared to a harmonic oscillator basis, (ii) in ^{61}Ca , the oscillator basis yields the level ordering of the naive shell model.

	^{53}Ca		^{55}Ca		^{61}Ca	
J^π	Re[E]	Γ	Re[E]	Γ	Re[E]	Γ
$5/2^+$	2.64	2.31	2.20	1.55	1.52	0.71
$9/2^+$	5.63	0.33	5.26	0.28	2.74	0.03

TABLE II: Energies of the $5/2^+$ and $9/2^+$ resonances in $^{53,55,61}\text{Ca}$. Re[E] is the energy relative to the one-neutron emission threshold, and the width is $\Gamma = 2\text{Im}[E]$ (in MeV).

As a check, we also computed the lowest excited states with spin and parity $J^\pi = 2^+, 4^+, 6^+$ in $^{50,54,56}\text{Ti}$. These states result from attaching two protons to the closed-core reference nuclei $^{48,52,54}\text{Ca}$, respectively, and we employ $2p-0h$ and $3p-1h$ excitations in the computation. Figure 4 shows a reasonably good agreement with the data, with a maximal deviation of about 0.6 MeV for the 2_1^+ state in ^{56}Ti . Let us compare the titanium isotopes to the isotopes $^{50,54,56}\text{Ca}$ which might also be computed by attaching two neutrons to $^{48,52,54}\text{Ca}$, respectively. The analysis of the cluster amplitudes shows that the $2p-0h$ cluster amplitudes account for about 65% of the total amplitude for the isotopes of titanium, while this number is about 72% for the calcium isotopes (with the remaining weight carried by $3p-1h$ amplitudes). Thus, the isotopes of titanium are more correlated due to proton-neutron interactions than the corresponding calcium isotopes. Most

likely, one needs $4p-2h$ amplitudes for a more accurate description.

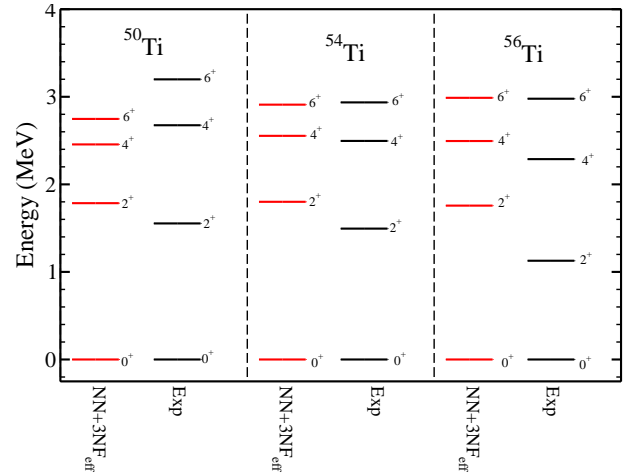


FIG. 4: (Color online) Theoretical excitation spectra of $^{50,54,56}\text{Ti}$ compared to data.

Summary. – We employed interactions from chiral effective field theory and performed coupled-cluster computations of neutron-rich calcium isotopes. The evolution of shell structure is understood by our computations of neutron-separation energies, low-lying $J^\pi = 2^+, 4^+$ states, and excitations in the odd-mass nuclei $^{53,55,61}\text{Ca}$. Our results confirm that the shell closure in ^{48}Ca is due to the effects of three-nucleon forces, and that ^{52}Ca and ^{54}Ca exhibit a sub-shell closure. We make several predictions for spin and parity assignments in the spectra of very neutron-rich isotopes of calcium and predict a level ordering in $^{53,55,61}\text{Ca}$ that is at variance with the naive shell model. Overall, we find that effects of three-nucleon forces and the scattering continuum are essential in understanding the evolution of shell structure towards the dripline.

We acknowledge valuable discussions with S. K. Bogner, R. J. Furnstahl, K. Hebeler, J. D. Holt, W. Nazarewicz, and A. Schwenk. This work was supported by the Office of Nuclear Physics, U.S. Department of Energy (Oak Ridge National Laboratory). This work was supported in part by the U.S. Department of Energy under Grant Nos. DE-FG02-03ER41270 (University of Idaho), DE-FG02-96ER40963 (University of Tennessee), and DE-FC02-07ER41457 (UNEDF SciDAC). This research used computational resources of the National Center for Computational Sciences, the National Institute for Computational Sciences, and the Notur project in Norway.

-
- [1] M. Mayer and J. H. D. Jensen, *Elementary Theory of Nuclear Shell Structure*, Wiley, New York (1955).
- [2] O. Sorlin and M.-G. Porquet, *Prog. Part. Nucl. Phys.* **61**, 602 (2008).
- [3] T. Otsuka *et al.*, *Phys. Rev. Lett.* **95**, 232502 (2005).
- [4] A. P. Zuker, *Phys. Rev. Lett.* **90**, 042502 (2003).
- [5] T. Otsuka *et al.*, *Phys. Rev. Lett.* **105**, 032501 (2010).
- [6] J. D. Holt and A. Schwenk, *arXiv:1108.2680* (2011).
- [7] G. Hagen *et al.*, *Phys. Rev. Lett.* **108**, in press (2012) and *arXiv:1202.2839* (2012).
- [8] J. D. Holt *et al.*, *arXiv:1009.5984v2* (2011).
- [9] A. Huck *et al.*, *Phys. Rev. C* **31**, 2226 (1985).
- [10] A. Gade *et al.*, *Phys. Rev. C* **74**, 021302 (2006).
- [11] R. V. F. Janssens *et al.*, *Phys. Lett. B* **546**, 55 (2002).
- [12] J. I. Prisciandaro *et al.*, *Phys. Lett. B* **510**, 17 (2001).
- [13] N. Marginean *et al.*, *Phys. Lett. B* **633**, 696 (2006).
- [14] S. N. Liddick *et al.*, *Phys. Rev. Lett.* **92**, 072502 (2004).
- [15] D.-C. Dinca *et al.*, *Phys. Rev. C* **71**, 041302 (2005).
- [16] M. Rejmund *et al.*, *Phys. Rev. C* **76**, 021304 (2007).
- [17] M. Honma *et al.*, *Phys. Rev. C* **65**, 061301 (2002).
- [18] E. Caurier *et al.*, *Rev. Mod. Phys.* **77**, 427 (2005).
- [19] L. Coraggio *et al.*, *Phys. Rev. C* **80**, 044311 (2009).
- [20] J. Dobaczewski *et al.*, *Prog. Part. Nucl. Phys.* **59**, 432 (2007).
- [21] D. R. Entem and R. Machleidt, *Phys. Rev. C* **68**, 041001(R) (2003).
- [22] R. Machleidt and D. R. Entem, *Phys. Rep.* **503**, 1 (2011).
- [23] F. Coester, *Nucl. Phys.* **7**, 421 (1958); F. Coester and H. Kümmel, *Nucl. Phys.* **17**, 477 (1960); J. Čížek, *J. Chem. Phys.* **45**, 4256 (1966); J. Čížek, *Adv. Chem. Phys.* **14**, 35 (1969); H. Kümmel, K.H. Lührmann, and J.G. Zabolitzky, *Phys. Rep.* **36**, 1 (1978).
- [24] R. J. Bartlett and M. Musiał, *Rev. Mod. Phys.* **79**, 291 (2007).
- [25] J. W. Holt, N. Kaiser, and W. Weise, *Phys. Rev. C* **79**, 054331 (2009); *ibid.* *Phys. Rev. C* **81**, 024002 (2010).
- [26] K. Hebeler and A. Schwenk, *Phys. Rev. C* **82**, 014314 (2010); K. Hebeler *et al.*, *Phys. Rev. C* **83**, 031301 (2011).
- [27] G. Hagen *et al.*, *Phys. Rev. C* **76**, 034302 (2007).
- [28] D. Gazit, S. Quaglioni, and P. Navrátil, *Phys. Rev. Lett.* **103**, 102502 (2009).
- [29] G. Hagen *et al.*, *Phys. Rev. Lett.* **101**, 092502 (2008).
- [30] G. Hagen *et al.*, *Phys. Rev. C* **82**, 034330 (2010).
- [31] A. D. Taube and R. J. Bartlett, *J. Chem. Phys.* **128**, 044110 (2008); *ibid.* **128**, 044111 (2008).
- [32] N. Michel *et al.*, *J. Phys. G* **36**, 013101 (2009).
- [33] G. R. Jansen *et al.*, *Phys. Rev. C* **83**, 054306 (2011).
- [34] A. Lapierre *et al.*, *Phys. Rev. C* **85**, 024317 (2012); A. T. Gallant *et al.*, *arXiv:1204.1987* (2012).
- [35] G. Audi, A. H. Wapstra, and C. Thibault, *Nucl. Phys. A* **729**, 337 (2003).
- [36] J. Meng *et al.*, *Phys. Rev. C* **65**, 041302 (2002); S. A. Fayans, S. V. Tolokonnikov, and D. Zawischa, *Phys. Lett. B* **491**, 245 (2000).
- [37] W. Nazarewicz *et al.*, *Phys. Rev. C* **53**, 740 (1996); J. Erler *et al.*, to be published (2012).
- [38] O. B. Tarasov *et al.*, *Phys. Rev. Lett.* **102**, 142501 (2009).
- [39] The binding energy of $^{40,48}\text{Ca}$ resulting from chiral NN interactions alone is larger than previously reported in Refs. [29, 30]. In the present work we use a higher cutoff ($J_{\text{max}} = 10$) in the relative angular momentum when transforming the NN interaction from the center-of-mass frame to the laboratory frame.